Progress in Materials Science 130 (2022) 100976

Contents lists available at ScienceDirect

Progress in Materials Science

journal homepage: www.elsevier.com/locate/pmatsci

Two-dimensional antibacterial materials

Bo Li [a], Yue Luo [a], Yufeng Zheng [b], Xiangmei Liu [a,c,*], Lei Tan [a], Shuilin Wu [b,*]

[a] Biomedical Materials Engineering Research Center, Collaborative Innovation Center for Advanced Organic Chemical Materials Co-constructed by the Province and Ministry, Hubei Key Laboratory of Polymer Materials, Ministry-of-Education Key Laboratory for the Green Preparation and Application of Functional Materials, School of Materials Science and Engineering, Hubei University, Wuhan 430062, China
[b] School of Materials Science & Engineering, Peking University, Beijing 100871, China
[c] School of Health Science & Biomedical Engineering, Hebei University of Technology, Xiping Avenue 5340#, Tianjin, 300401, China

ARTICLE INFO

Keywords:
Two-dimensional materials
Endogenous and exogenous response
Photocatalytic
Photothermal
Antibacterial
Therapy

ABSTRACT

Diseases caused by pathogens continue to threaten the health of people around the world, especially with the emergence of drug resistance. Therefore, there is an urgent need to develop new strategies that can replace antibiotic therapy. Novel nanomaterials represented by two-dimensional nanomaterials (2DNMs) have great application prospects in the field of antibacterial due to their tunable band gaps, special crystal structures, and limitations on carrier migration and thermal diffusion. In this review, several representative 2DNMs such as graphene, graphitized carbonitride and transition-metal dichalcogenides are reviewed and summarized including their research basis, progress, and prospects in the field of antibacterial. It starts with the introduction of the material, focusing on summarizing its inherent antibacterial properties and light-induced antibacterial properties. Specific strategies to optimize the antibacterial properties of 2DNMs are discussed. Finally, the challenges facing current antimicrobial 2DNMs are discussed and future prospects for the field are proposed based on the combination of photocatalysis and other germicidal technologies.

1. Introduction

Bacterial infection in humans has long been a concern. Although it was hoped that Fleming's discovery of antibiotics in 1928 would overcome bacterial-related diseases [1], in recent decades, the misuse of antibiotics has weakened the susceptibility of bacteria to antibiotics, resulting in the reduction or elimination of drug potency [2]. Hence, the treatment of bacterial infections has become increasingly difficult [3,4]. The development of drug systems that have excellent antibacterial properties and the prevention of drug resistance are important topics in scientific research. Since the discovery of graphene in 2004 [5], two-dimensional materials (2DNM) have drawn the attention of researchers. 2DNMs are materials in which electrons can move freely in only two dimensions (planar motion) at the nanoscale (1–100 nm) [6]. Typical 2DNMs discovered so far include carbon-based materials, such as the following: graphene, graphene oxide (GO) [7]; reduced graphene oxide (rGO) and its derivatives [8]; transition metal dichalcogenides (TMD) and their derivatives [9]; graphitic carbon nitride (g-C_3N_4) [10]; titanium carbide (MXenes) [11]; black phosphorus (BP) [12]; and boron

* Corresponding authors at: Biomedical Materials Engineering Research Center, Collaborative Innovation Center for Advanced Organic Chemical Materials Co-constructed by the Province and Ministry, Hubei Key Laboratory of Polymer Materials, Ministry-of-Education Key Laboratory for the Green Preparation and Application of Functional Materials, School of Materials Science and Engineering, Hubei University, Wuhan 430062, China (Xiangmei Liu).

E-mail addresses: liuxiangmei1978@163.com (X. Liu), slwu@pku.edu.cn (S. Wu).

https://doi.org/10.1016/j.pmatsci.2022.100976
Received 31 March 2021; Received in revised form 15 May 2022; Accepted 6 June 2022
Available online 13 June 2022

Abbreviation

2DNMs	Two-dimensional nanomaterials
3D	Three-dimensional
Ag	Silver
Cu	Copper
Zn	Zinc
Pd	Palladium
AuNPs	Gold nanoparticles
S. aureus	*Staphylococcus aureus*
E. coli	*Escherichia coli*
P. aeruginosa	*Pseudomonas aeruginosa*
B. subtilis	*Bacillus subtilis*
PTT	Photothermal therapy
PTAs	Photothermal agents
PDT	Photodynamic therapy
SDT	Sonodynamic therapy
MW	Microwave
ROS	Oxygen species
•OH	Hydroxyl radicals
$\bullet O_2^-$	Superoxide anion
$^1O_2$	Singlet oxygen
CB	Conduction band
VB	Valence band
SPR	Surface plasmon resonances
LSPR	Localized surface plasmon resonances
GO	Graphene oxide
rGO	Reduced graphene oxide
TMDs	Transition metal dihalides
g-C_3N_4	Graphitic carbon nitride
MXenes	Titanium carbide
BP	Black phosphorus
MoS_2	Molybdenum disulfide
WS_2	Tungsten disulfide
WO_3	Tungsten trioxide
BN	Boron nitride
CVD	Chemical vapor deposition
NIR	Near-infrared
RP	Red phosphorus
Bi_2WO_6	Bismuth tungstate
CQDs	Carbon quantum dots
N	Nitrogen
O	Oxygen
S	Sulphur
PA	Polyamide
PDINH	Perylene-3,4,9,10-tetracarboxylic diimide
PEI	Polyethyleneimine
PEG	Polyethylene glycol
CS	Chitosan
VOPc	Vanadyl-phthalocyanine
AQS	Sodium anthraquinone-2-sulfonate
QAS	Quaternary ammonium salt
AA	Ascorbic acid
HA	Hyaluronic acid
Hap	Hydroxyapatite
PVP	Polyvinylpyrrolidone
BNN6	N,N'-di-*sec*-butyl-N,N'-dinitroso-1,4-phenylenediamine
NHx	A types of N vacancies
N_2C	A types of N vacancies
PAO	Polyamidoxime

GSH	Glutathione
GSSG	Oxidized glutathione
ATP	Adenosine Triphosphate
EPS	Extracellular polymers

nitride (BN) [13]. As novel materials with unique properties, 2DNMs may provide new solutions to the growing problem of microbial infection.

Antibacterial strategies are either endogenous or exogenous. Among the antibacterial materials that have been developed, 2DNMs exhibit unique advantages for both exogenous and endogenous strategies because of their specific 2D structures, tunable size, and energy bands [14]. First, all 2DNMs have large specific surface areas, so they can be used as carriers of antibacterial drugs [15–16]. In addition, compared with traditional endogenous antibacterial systems, such as various metal ions (silver (Ag) [17], copper (Cu) [18], and zinc (Zn) [19]), organic materials (antimicrobial peptides [20], quaternary ammonium salts [21], and other systems [22]), 2DNMs have distinctive antibacterial mechanisms. Traditional endogenous antibacterial systems take advantage of their interactions with bacterial cell membranes [23–24] or their oxidative properties [25–26] to achieve bacteriostatic and bactericidal effects. However, 2DNMs use their 2D structures to achieve the effect of physical puncture and produce an oxidative stress response through physical and chemical interactions with microorganisms [27], thereby eliminating microorganisms. Meanwhile, traditional materials have limitations. For example, the release of ions is uncontrollable. When the upper tolerance limit of the human body is reached, toxicity occurs [28]. Organic antibacterial agents have poor heat resistance, and they are easily hydrolyzed, resulting in a short period of validity [29]. In addition, the toxicity of their decomposition products cannot be determined [30], which seriously hinders future research on the applications of this traditional antibacterial agent. In contrast, because 2DNMs have the advantages of simple preparation, low cost and high stability to induce drug resistance, they are novel antibacterial candidates [31].

Finally, in 2DNMs, because an exogenous antibacterial effect can be generated by exogenous stimuli, they are versatile and suitable for the elimination of microorganisms without causing drug resistance. Moreover, they are highly stable and have low toxicity in tissue cells [32,33]. Unlike the endogenous antibacterial strategy, which requires that the material contacts bacteria, the exogenous antibacterial strategy requires external stimuli, such as light, ultrasound, and microwaves, to stimulate the material, thus affecting the local environment and indirectly acting on bacteria, which are then inhibited or inactivated [34–36]. The photoinduced antibacterial method includes photothermal therapy (PTT) and photodynamic therapy (PDT), both of which can induce bacterial inactivation [37]. Reactive oxygen species (ROS) generated by PDT and local high temperatures generated by PTT disrupt bacterial cell membranes and inactivate bacterial deoxyribonucleic acid (DNA) and proteins, which are the main bactericidal mechanisms [38]. This antibacterial mode has a controllable effect on local infection and minimizes side effects in normal tissues. However, because of the poor penetration of light, the therapeutic effect on deep bacterial lesions is greatly reduced, which limits its applicability. Sonodynamic therapy (SDT) is a particularly novel technology [39]; it relies on the interaction of ultrasound and sonosensitizers to generate ROS under low-frequency ultrasound, destroying almost all bacteria. Because of the deep tissue penetration of ultrasound, this technology is suitable for treating deep infections. Another exogenous stimulus strategy, microwave irradiation, excites responsive materials to produce a microwave thermal effect that can inhibit bacterial growth [40].

Despite significant achievements in the development of 2D antibacterial materials, only a few reviews of the relevant literature have been conducted. Furthermore, these previous reviews focused on a certain types of 2D materials with antibacterial properties [41,42]. Therefore, from the perspective of materials science, an in-depth and systematic review of the latest research in the literature is warranted. The present literature review summarizes new frontiers in recent research on 2D antibacterial materials, including the inherent antibacterial properties of 2DNMs, as well as their light-responsive photothermal and photodynamic antibacterial properties and mechanisms. In addition, methods for improving the performance of 2DNMs are reviewed in terms of surface modification, defects, heterojunctions, and so on. [43]. Finally, the antibacterial potential of 2DNMs under ultrasonic and microwave irradiation is also discussed. The literature review discusses and analyzes the development of 2DNMs and suggests future research directions for overcoming challenges in their practical application.

2. Typical 2D antibacterial nanomaterials

After Geim's team at the University of Manchester successfully separated the single atomic layer of graphene, the 2DNM concept was proposed to describe a 2D atomic crystal material [5]. Thereafter, other 2DNMs were discovered, such as graphitic carbon nitride (g-C_3N_4) [44], molybdenum disulfide (MoS_2) [45], tungsten disulfide (WS_2) [46], MXene [47], bismuth (Bi)-based materials [48], and BN [49]. Because of their unique structures and photoelectrical properties, these 2DNMs exhibit immense potential for biological applications. Fig. 1 provides a schematic summary of these 2DNMs and their biomedical applications.

2.1. Graphene-based 2DNMs

Graphene is a 2DNM composed of carbon atoms, and structured in a hexagonal honeycomb lattice due to the sp^2 hybrid orbital of the atoms [50]. In this particular structure, the *p-s* orbital of each carbon atom in graphene is perpendicular to the direction of the layer, which forms a large polyatomic π bond throughout the entire layer, resulting in tunable electrical, thermal, optical, mechanical properties and a large specific surface area [51]. Graphene is prepared through chemical vapor deposition and thermal stripping. Graphite oxide is fabricated by oxidation using the Hummers method [52]. Reduced graphene oxide flakes were obtained by a

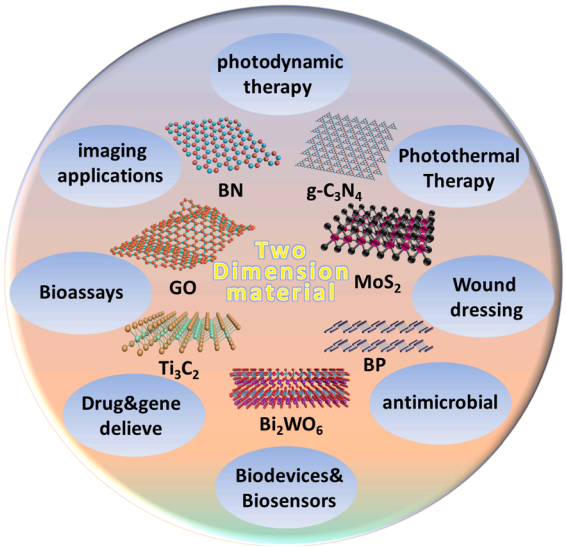

Fig. 1. Common 2DNM and its application in biology.

reduction method. Because graphene is a zero-band gap material (i.e., its band gap is zero) and is easily oxidized, it is often compounded with other semiconductors and metal nanostructures to improve its performance, thereby forming composite materials suitable for various applications [53,54]. For example, in the field of photocatalysis, graphene has been applied because of its high electrical conductivity (10^6 S m^{-1}), and in nanocomposites, it plays a positive role in accepting or transferring electrons, which helps to improve photocatalytic performance [55]. At present, the main methods used to enhance the antibacterial properties of graphene-based materials are as follows: adjusting the size and number of layers, surface functionalization, building a heterojunction structure, and building a composite system [56–59].

2.2. Graphitic carbon nitride

Similar to graphene, graphitic carbon nitride (g-C_3N_4) has a planar 2D sheet structure [44]. It has two basic units: a triazine ring and a 3-s triazine ring. The layers are assembled by van der Waals forces to form a 2D nanosheet [60]. Because of its convenient synthesis and functionalization, stable electronic field emission, and controllable forbidden band, g-C_3N_4 has received much attention in the photocatalysis literature. Moreover, g-C_3N_4 has perfect thermal and chemical stability. It maintains the stability of the structure and its performance under high temperatures as well as in acid and alkali conditions. In addition, the material is environmentally friendly and does not cause secondary pollution. The general preparation route of g-C_3N_4 uses a variety of nitrogen (N)-rich precursors (e.g., dicyandiamide, urea, melamine, and thiourea) in various methods, such as the solid-phase reaction method, solvothermal method, electrochemical deposition, and thermal polymerization [61]. As a result, g-C_3N_4 has received extensive attention in various research fields. However, it is worth noting that because of its poor water solubility, large particle size, low conductivity, wide band gap (i.e., light absorption wavelengths of less than 460 nm), and other shortcomings, its practical application remains limited. Therefore, several recent studies have shown that its photocatalytic performance could be improved by surface modification, doping, defect formation, and composite structure [62–65].

2.3. MXene

MXene is a 2D, layered transition metal carbide or nitride etched to obtain a layered structure [47]. It is composed of three main elements: transition metals (e.g., Ti, V, Cr, and Nb), IIIA, or IVA elements (e.g., Al, Si, and St), and carbon or nitrogen. Its chemical formula is $M_{n+1}AX_n$ (n = 1, 2, or 3). MXenes have not only the characteristics of a large specific surface area and high conductivity (9.88×10^5 S m^{-1}), similar to graphene, but also the advantages of the flexible adjustment of components and controllable minimum nanolayer thickness [66]. Because they are prepared by etching, the obtained MXenes consist of a single layer or only a few layers, and their thickness is usually less than 1 nm. Their lateral size ranges from nanometers to micrometers. Modified by functional groups, such as hydroxyl, oxygen, or fluorine, the surfaces of MXenes are hydrophilic, and they have broad application potential in the field of biomedicine [67]. Moreover, because they have good biocompatibility, nontoxicity, and degradability, they are eliminated by the human body. In addition, MXenes have a strong light response to near-infrared (NIR) light. Therefore, in antibacterial applications, they are flexibly functionalized through different surface modifications to improve their photocatalytic antibacterial performance [68].

2.4. Black phosphorus

In recent years, phosphorus has received much attention because of its widespread distribution and its environmentally friendly characteristics [24]. So far, various phosphorus allotropes have been found, including BP, amorphous red phosphorus (RP) [33], Hittorf's RP, and fibrillar RP [69,70]. Among these, BP differs from other allotropes because it has a 2D structure, which has attracted much attention in the relevant literature. The most mature methods used to prepare BP include mechanical extraction, liquid extraction, and *in situ* chemical vapor deposition (CVD). Phosphorus is sensitive to air because its valence electrons and configuration result in a pair of unshared electrons in each phosphorus atom [71]. Therefore, it has potential as a photocatalytic antibacterial [72]. In addition, the antibacterial strategy of physical puncture is also an advantage of BP [73].

2.5. Transition metal dichalcogenides

TMDs are a new type of 2DNM [22]. Their chemical formula is expressed as MX_2, which contains three atomic layers. Three chalcogenide (S, Se, and Te) atomic layers are connected by a transition metal atomic layer. In TMDs, two adjacent chalcogenide layers are combined by van der Waals forces, which allow for maintaining a 2D structure. Their ultrathin atomic single- or multilayer structure results in semiconductivity and semimetallic magnetism. TMDs have been shown to have unique optical, mechanical, and electronic properties, and they are widely used in optoelectronics, catalysts, biomedical engineering, and solar energy batteries [74,75]. The edge of MoS_2 has high catalytic activity, which, unlike the base surface of TMDs, tends to function as the catalytic center. However, its thermodynamic reactions tend to occur on the substrate surface, which limits the activation of active surface sites [76]. Therefore, improving the photocatalytic antibacterial efficiency of TMDs depends on controlling the surface structure on an atomic scale, including increasing the defective content and the specific surface area to expose more edge sites [77].

2.6. Bismuth-based materials

Bismuth (Bi)-based materials have been extensively researched because of their high stability, nontoxicity, wide energy band structure, and excellent photodegradation performance in pollutants. At present, bismuth-based photocatalysts that have been studied include bismuth oxide, bismuth halide oxide, bismuth tungstate (Bi_2WO_6), and bismuth molybdate [78]. Bismuth and oxygen can be combined through the hybridization of Bi(*6 s*) orbital and O(*2p*) orbital. Their unique atomic layer structure facilitates electronic conduction, and their tunable physical and electronic properties enable Bi-based materials to maximize their photocatalytic activity in a wide range [79]. Therefore, the current research directions for improving the photocatalytic antibacterial properties of Bi-based materials are as follows: changing the size, doping, or introducing defects, metal deposition, semiconductor bonding, and conjugated structural surface modification [80–82].

2.7. Boron nitride

BN is a 2D crystal composed of N atoms and boron atoms. Hexagonal BN has perfect high-temperature stability, high strength, high thermal conductivity (22 W $m^{-1}K^{-1}$), a low expansion coefficient (8.1×10^{-6} K^{-1}), large resistivity (14.4 Ω cm), and corrosion resistance [49]. They are prepared by chemical gas phase synthesis, hydrothermal synthesis, benzene thermal synthesis, self-propagating technology, and carbothermal synthesis technology [83]. The properties and applications of BN nanosheets are complementary to graphene, and they have advantages for chemical and thermal stability. The biocompatibility of BN depends on its size, shape, structure, and surface groups. Unsaturated boron atoms located at the edge or surface of nanosheets cause bacterial death [84]. In the field of photocatalytic antibacterials, the high thermal conductivity and high specific surface area of BN are often used to form heterojunctions with metals, metal oxides, and semiconductors to improve their antibacterial activity [85].

3. Antibacterial mode and related mechanisms

The antibacterial mode comprises both endogenous and exogenous antibacterial strategies. 2DNMs have unique 2D structures and abundant surface groups. In addition, their properties include tunable thickness and band gaps. 2DNMs not only inhibit bacterial activity through their inherent antibacterial activity but also indirectly act on bacteria through their response under specific conditions. The former is the endogenous mode, while the latter is the exogenous mode. These modes will be discussed in detail in the following sections.

3.1. Inherent antibacterial properties of 2DNMs

3.1.1. Physical prick

The bacterial cell wall is located in the outermost layer, which is wrapped around the cell membrane [86]. The surface compositions of the bacterial membrane of gram-positive bacteria and the cell walls of gram-negative bacteria are different, but they have in common the functional substance of peptidoglycan [87]. The main functions of the bacterial membrane are as follows: 1) maintains the shape of the cell and improves mechanical strength; 2) inhibits mechanical and osmotic damage; 3) assists in cell movement and growth; and 4) confers specific antigenicity on antibiotics and bacteriophages [88].

Previous studies confirmed that when nanosheets come into physical contact with bacteria, their sharp edges are beneficial for

destroying bacterial membranes [89]. The destruction of the bacterial membrane leads to the leakage of DNA, phospholipids, and proteins in the cell. Through physical action, antibacterial agents have the following advantages: 1) they have a universal eliminating effect on a variety of bacteria; 2) their high stability prevents bacterial growth for a long time; and 3) they do not cause secondary pollution. In recent years, an increasing number of 2DNMs, such as MoS_2, WS_2, GO, and BP, have been proven to have physical puncture properties, and they have been used in effective physical contact sterilization [90].

The physical puncture hypothesis first needs to be determined. Lu et al. studied the interactions between different orientations of GO toward bacteria [91]. Three different orientations of GO nanosheets (i.e., random, vertical, and planar) were prepared via the action of a magnetic field. The morphology of bacteria on random GO and planar GO remained intact, whereas the bacteria on vertical GO presented severe shrinkage, indicating a loss of viability and cell membrane damage [92]. This mechanism suggested that the sharp edges of graphene nanosheets had the characteristic of destroying the bacterial membrane. The detection of dye fluorescence further confirmed that the breakage of the membrane in the GO/lipid vesicle system was caused by the physical disruption of the bilayer structure of the GO nanosheets, rather than by ROS oxidation.

Specific 2DNMs have been shown to have physical piercing antibacterial properties, but the specific mechanism of action still needs to be determined. There are three modes of insertion: First, under the action of bacteria's gravity, contact between bacteria and the edge of the nanosheet is established. For example, Wei et al. designed and investigated the antibacterial properties of vertically and horizontally aligned graphene on semiconductor silicon (Si) and insulator silicon dioxide substrates against different types of bacteria [93]. According to the experimental results, the specific antibacterial mechanisms of different types of bacteria were different (Fig. 2**a**). The mechanism of gram-positive bacteria was physical puncture. By their own gravity, the bacteria were easily punctured by the vertically arranged graphene film, thus destroying the bacterial membrane and inactivating bacteria. In gram-negative bacteria, the antibacterial mechanism was shown to be electron transfer. Because negative electricity came from the respiratory proteins in the microbial membrane, the bacteria membrane surface had more negative charges. In addition, graphene has excellent conductivity and can be used as an electron acceptor, electrons were easily captured from the microbial film, which was then transferred to the

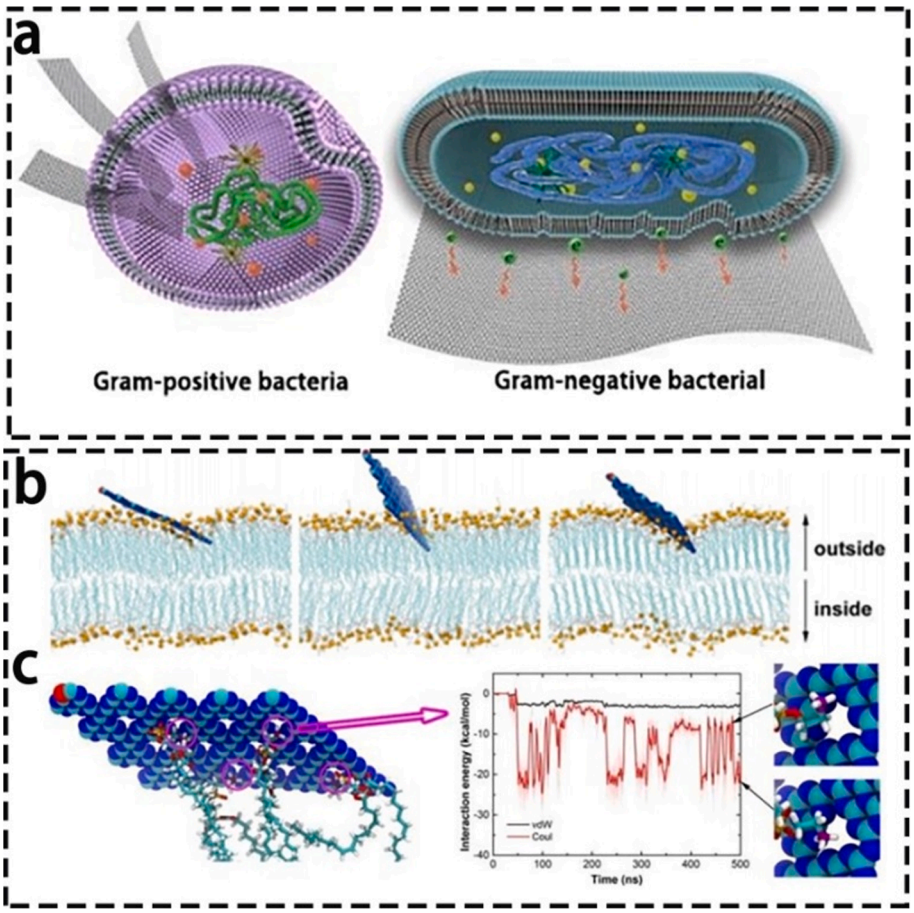

Fig. 2. (a) Diagram showing the different antibacterial mechanisms of graphene coated materials [93]. Adapted with permission. Copyright 2021, Royal Society of Chemistry. (b) Final snapshots of g-C_3N_4 nanosheet interacting with the lipids of bacterial membrane in three independent trajectories. (c) Snapshot of g-C_3N_4 capturing lipids' heads at it pore sites. And the interaction energies between one typical lipid and g-C_3N_4 [94]. Adapted with permission. Copyright 2019, Royal Society of Chemistry.

underlying substrate. Compared with the insulating silica substrate, the antibacterial performance of the silicon substrate system was better. It could be more clearly shown that graphene caused a continuous loss of electrons from the gram-negative bacterial biofilm, thereby making it inactive. Second, nanosheets can adsorb to the bacterial membrane and destroy its structure through van der Waals forces and hydrophobic interactions. For example, Cui et al. examined the sterilization properties of g-C_3N_4 treated with N plasma (N-g-C_3N_4) [94]. After 8 h of incubation in a dark environment, the bactericidal rate of N-g-C_3N_4 against eight kinds of foodborne pathogens was over 99%, which was over 10 times more efficient than that of untreated g-C_3N_4. The main reason for this result was that direct physical contact between the g-C_3N_4 nanosheets and the cell membrane led to cell rupture. To further characterize its performance by simulating molecular dynamics, it was found that the process of N-g-C_3N_4 nanosheets approaching the cell membrane was mainly driven by the Coulomb force (Fig. 2**b, c**). When the nanosheets were close to the phospholipid molecules on the cell membrane, the Coulomb force between the phospholipids carrying positively charged amino groups and negatively charged N-g-C_3N_4 nanosheets drove the nanosheets into the phospholipid bilayer. The nanosheets were then easily inserted into the phospholipid bilayer, resulting in the high physical antibacterial properties of N-g-C_3N_4. Finally, destructive extraction has been shown to cause membrane deformation and loss of integrity. For example, Tu et al. studied the molecular mechanism of graphene-induced *E. coli* cell membrane degradation and found that, in addition to severe insertion and cleavage, the destructive extraction of lipid molecules was also an important factor [95]. The phenomenon of the direct extraction of phospholipids from lipid membranes was verified by computer simulations and TEM images. This phenomenon was mainly due to the unique 2D structure of graphene, which had sp^2 carbon atoms that contributed to the generation of an exceptionally strong dispersion interaction between the graphene and lipid molecules, resulting in a powerful attraction. Because of the redistribution of hydrophobic tails, in order to maximize the hydrophobic interaction with the graphene surface, the extracted lipid molecules also performed synergistic movements on the graphene 2D surface.

3.1.2. Antibacterial oxidative stress

The term oxidative stress refers to an imbalance in the oxidative and antioxidative effects on bacteria under external stimuli. The generation of oxidative stress oxidizes and destroys the substances on the surface of the membrane, disrupts the basic functions of cells, hinders the metabolism of bacteria, and eventually leads to bacterial inactivation [96]. Therefore, oxidative stress is a widely accepted antibacterial method. As shown in Fig. 3, two types of oxidative stress are mediated by 2DNMs. The first is ROS-dependent oxidative stress. When bacteria are activated by outside stimuli, the intracellular redox reaction is unbalanced, resulting in the excessive accumulation of active substances, such as hydrogen peroxide (H_2O_2), hydroxyl radical (•OH), superoxide anion ($\bullet O_2^-$), and singlet molecular oxygen ($^1O_2$), which ultimately affects bacterial activity [97,98]. The second type is ROS-independent oxidative stress, which refers to the direct contact of nanomaterials with bacterial membranes through electron transfer or redox reactions, directly destroying or oxidizing the structure of the membrane and its surface components, rather than generating ROS [99,100].

To verify the mechanism of ROS-dependent oxidative stress, as shown in Fig. 4**a-c**, Karunakaran et al. used different surfactant molecules with thiol functions to exfoliate and modify 2H-MoS_2 nanosheets to enhance antibacterial effects [98]. In the main mechanism, positively charged and functionalized 2H-MoS_2 interacted with the bacterial surface to generate ROS. The conduction band (CB) of 2H-MoS_2 was lower than the redox potential of ROS generation, which contributed to the generation of ROS. A glutathione (GSH) depletion experiment further verified the production of ROS in the cells. Gurunathan et al. reported the antibacterial mechanism of GO and rGO against *Pseudomonas aeruginosa* [101]. Both GO and rGO accelerated oxidative stress in cells by disrupting the balance between oxidant and antioxidant processes. The generated ROS accumulated and destroyed cellular components, including DNA and proteins. Another 2D nanomaterial, BP, can also be used to eliminate bacteria by promoting the production of oxidative stress. The antibacterial behavior of BP nanosheets after exfoliation was examined by Xiong et al [102]. They detected intracellular ROS levels by testing the fluorescence intensity, confirming that the main bactericidal mechanism of BP was to induce

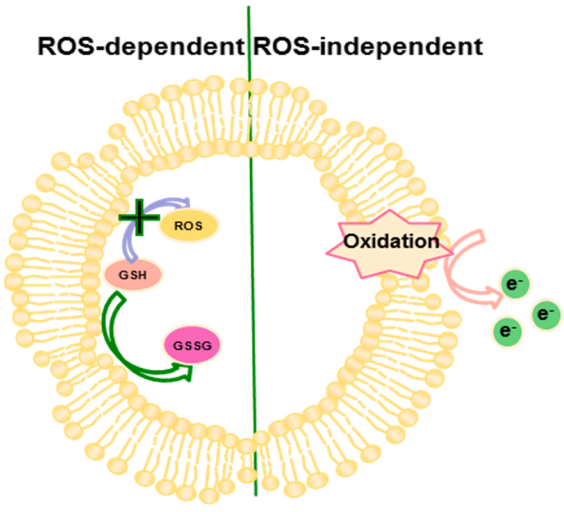

Fig. 3. Schematic diagram of oxidative stress of 2DM.

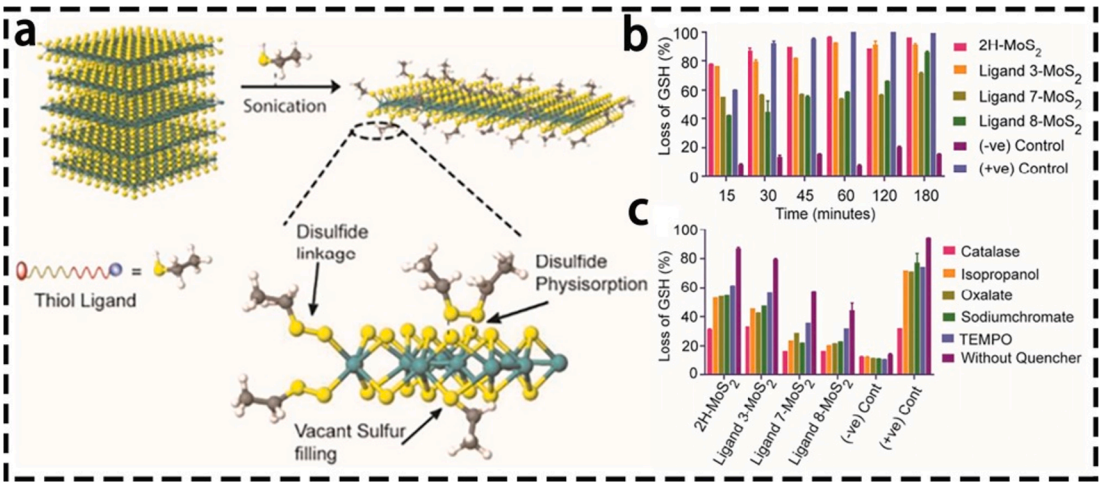

Fig. 4. (a) Schematic representation of the ligand induced exfoliation and possible modes of MoS_2 surface functionalization. (b) Abiotic oxidative stress estimation by Ellman's assay. (c) Estimation of the type of ROS species by Ellman's assay in the presence of different ROS scavengers. [98]. Adapted with permission. Copyright 2018, American Chemical Society.

ROS-dependent oxidative stress. Specifically, the BP nanosheet group showed more obvious green fluorescence compared with the control group, indicating that BP enhanced the production of ROS in bacteria, consequently leading to bacterial death. Furthermore, because of differences in membrane structure and function, the BP nanosheets against two bacterial strains, gram-negative *Escherichia coli* (*E. coli*) and gram-positive *Bacillus subtilis* (*B. subtilis*), showed time- and concentration-dependent bactericidal activities. The thinner cell wall of *E. coli* made it more sensitive to the treatment of BP nanosheets in an early stage (6 h), so the growth inhibition and bactericidal effects on *E. coli* were more pronounced than those of *B. subtilis*. Considering the self-healing ability of the outer membrane of *E. coli*, the antibacterial properties of BP against it were partially reversible, and the effect weakened after 12 h.

Unlike ROS-dependent mechanisms, ROS-independent mechanisms are direct oxidation reactions. As shown in Fig. 5**a**, Pandit et al. used different thiol ligands to chemically exfoliate and modify MoS_2 to obtain ce-MoS_2. The surface of the material then had different charges and hydrophobicities, thus achieving highly efficient antibacterial efficacy against pathogens and their biofilms [103]. Their results demonstrated that because of the positive charge, the bacterial surface was effectively bound to MoS_2 nanosheets, thereby amplifying the effects of oxidative stress on the bacteria (Fig. 5**b-c**). Long-chain alkanes have hydrophobic interactions with bacterial cell membranes, which could depolarize bacterial membranes to varying degrees, change the surface potential of the membranes, inhibit bacterial metabolic activities, and lead to bacterial death. In addition, they could inhibit the formation of bacterial biofilms while maintaining inhibitory activity on the already formed biofilm [104]. Kim et al. investigated GO and MoS_2 composite systems that had enhanced antibacterial activity [105], mainly because of their increased oxidation ability and improved electrical conductivity (Fig. 5**d**). The GO-MoS_2 nanocomposite exhibited a higher ROS-independent oxidation ability (Fig. 5**e-f**). That is, it oxidized the bacterial cell structure directly, destroying the bacterial membrane and inducing leakage of intracellular components, thus eliminating

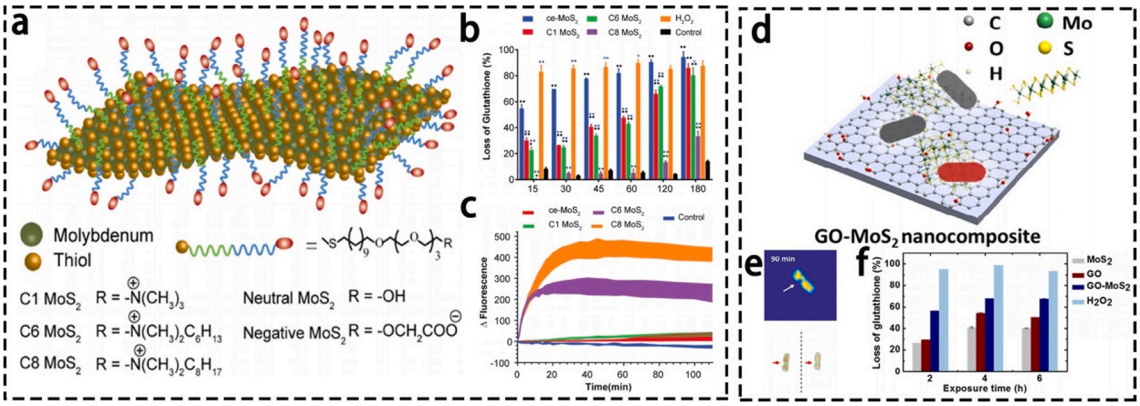

Fig. 5. (a) Schematic representation of functionalized ce-MoS_2 with thiol ligands. (b) Abiotic glutathione oxidation assay for quantification of oxidative stress generated. (c) Quantification of membrane depolarization of *MRSA* using DISC3(5) fluoresecent probe [103]. Adapted with permission. Copyright 2016, American Chemical Society. (d) Schematic of GO-MoS_2 nanocomposite film. (e) Representative cross-sectional images of 3D RI tomograms of a bacterial cell came in contact with 2D nanocomposite surface for 90 min on the focal plane. (f) *In vitro* glutathione oxidation using Ellman's assay [105]. Adapted with permission. Copyright 2017, American Chemical Society.

the bacteria. In addition to direct contact with bacteria, 2DNMs can also wrap bacteria, which leads to their inactivation. Rasool et al. reported the antibacterial behavior of $Ti_3C_2T_x$ in a colloidal suspension [106]. Their results showed that $Ti_3C_2T_x$ exhibited strong antibacterial properties because of its high hydrophilicity, which enhanced contact with bacteria. As the $Ti_3C_2T_x$ concentration increased, the bacteria were encapsulated by nanoscale $Ti_3C_2T_x$ flakes to form aggregates. The strong reducing activity of $Ti_3C_2T_x$ and its active surface could be used to directly inactivate attached microorganisms. Finally, hydrogen bonds between the oxygen-containing groups of $Ti_3C_2T_x$ and lipopolysaccharide chains on the cell membrane inhibited bacterial growth by preventing the uptake of nutrients.

3.2. Photodynamic antibacterial activity of 2DNMs

Photodynamic therapy is a new technology developed to treat bacterial diseases based on the photocatalytic properties of photosensitive materials [107,108]. As shown in Fig. 6, when light irradiation excites the photosensitive material, electrons gain energy and transfer from the ground state to the excited state. The excited electrons react with water or oxygen to generate highly reactive $^1O_2$ and •OH, which directly oxidates bacteria, resulting in cell damage and even death [109,110]. This strategy has been extensively studied, and the application of 2DNMs has been expanded in the antibacterial field [111,112].

Chong et al. confirmed the antibacterial property of GO under simulated sunlight and revealed its underlying mechanism [113]. Measurements of ROS showed that GO produced only a few $^1O_2$ under dark conditions, and its oxidative activity was low (Fig. 7**a-e**). However, under light irradiation, photoinduced electron-hole pairs were generated on the active sites on the surface of GO. These photoinduced electrons promoted the reduction of GO which then introduced carbon-centered radicals, thus accelerating damage to the bacterial antioxidant system and effectively eliminating bacteria [114]. Huang et al. found that graphitic carbon nitride polymer was an effective and recyclable catalyst that induced electrons and holes to react with the bacterial membrane and caused bacterial inactivation under visible light irradiation [115].

3.3. Strategies for enhancing photocatalytic activity

Despite the advantages described above, most 2DNMs exhibit poor innate photocatalytic performance due to poor photoelectric conversion efficiency or rapid coupling of light-generated electrons and holes, which results in poor antibacterial efficiency under light irradiation. Various strategies have been developed to improve the photocatalytic antibacterial effects. Recent studies in the relevant literature have found methods that can be used to improve the photocatalytic performance of 2DNMs, thereby improving their antibacterial effects [116].

3.3.1. Changing the size or thickness of nanometer sheets

The size and thickness of 2DNMs have been shown to be closely related to their performance [117]. For example, the bandgap of the conventional multilayer bulk nanocrystalline Bi_2WO_6 is 2.9 eV. When Bi_2WO_6 was prepared as a monolayer using cetyltrimethylammonium bromide, the band gap was reduced to 2.7 eV. In this case, the prepared monolayer of Aurivillius oxide, Bi_2WO_6, had a unique sandwich structure $[BiO]^+$-$[WO_4]^{2-}$-$[BiO]^+$, which mimicked a traditional heterojunction structure (Fig. 8**a**) [118]. Because it was a single-atom-layer nanosheet, many unsaturated bismuth atoms on its surface were used as active sites. Therefore, under irradiation, the active sites directly generated holes, and the interlayer generated electrons, which enabled ultrafast charge separation. Hence, the brominated surface modification reduced the material's bandgap by 0.2 eV and increased the material's light absorption intensity. In addition, the unique atomic arrangement mimicked the heterojunction, which facilitated the separation of photogenerated carriers, thus effectively improving photocatalytic performance. In addition to simulating the heterostructure interface in a specific monolayer 2DNM by changing the number of layers, the structure could also be changed to obtain a porous structured 2DNM with an increased surface area, thereby lowering its band gap and enhancing its light absorption. For example, the photocatalytic performance of bulk g-C_3N_4 is not ideal because of its wide band gap (2.7 eV), high exciton dissociation energy, and limited electron mobility. The first issue to be solved was a peeling and layering treatment, which would be highly significant for improving overall activity. Kang et al. developed a simple bacterial etching method by exfoliation at room temperature to prepare high-quality g-C_3N_4 nanosheets (Fig. 8**b**) [119]. The g-C_3N_4 treated with bacteria had not only a 2D structure (BT-CN-2D) but also a porous structure

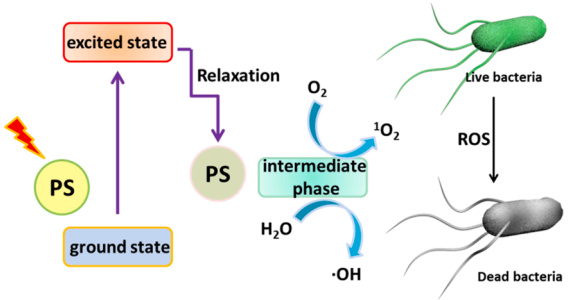

Fig. 6. Antibacterial diagram of photocatalyst.

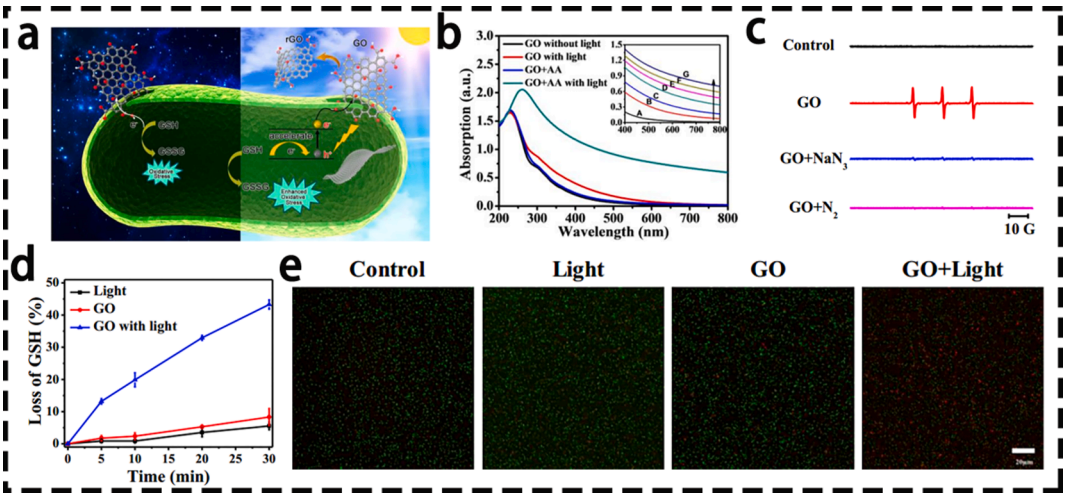

Fig. 7. (a) Antibacterial diagram of GO in dark and visible light (b) UV–vis spectra of GO dispersions under different conditions as above. (c) ESR spectra of GO alone, addition of NaN_3, and anaerobic conditions. (d) *In vitro* GSH oxidation. (e) Representative fluorescence images of cells after different treatments. Scale bars = 20 μm [113]. Adapted with permission. Copyright 2017, American Chemical Society.

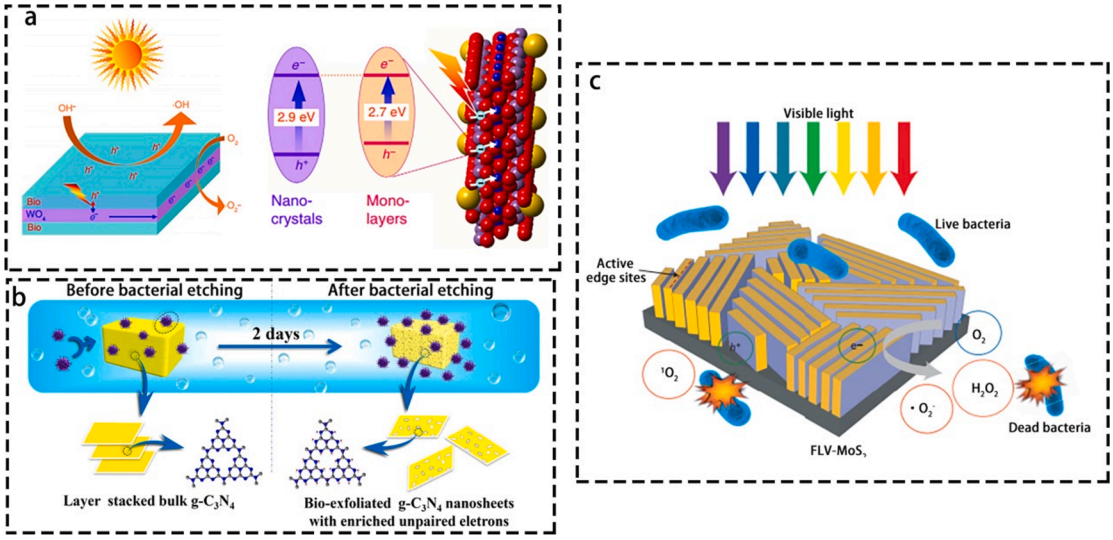

Fig. 8. (a) Schematic illustration of photocatalytic mechanism over the monolayer Bi_2WO_6. And the band energy diagrams of Bi_2WO_6 nanocrystals and monolayers [118]. Adapted with permission. Copyright 2015, Springer Nature. (b) The proposed bacterial-inspired synthesis process and mechanism of bacteria treated g-C_3N_4 samples [119]. Adapted with permission. Copyright 2018, American Chemical Society. (c) Schematic that shows the FLV-MoS_2 inactivating bacteria in water through visible-light photocatalytic ROS generation [123]. Adapted with permission. Copyright 2016, Springer Nature.

on the surface. Therefore, its specific surface area was significantly increased, and the band gap was significantly reduced to 2.11 eV. Many unpaired electrons were enriched in BT-CN-2D, and the electrons were rapidly transmitted. Therefore, the photocatalytic performance of BT-CN-2D was four times higher than that of bulk g-C_3N_4, and antibacterial stability was superior. In addition to structure, changing the thickness of 2DNMs also can greatly improve performance [120]. For example, a single layer of g-C_3N_4 prepared by thermal etching and ultrasonic stripping had a thickness of 0.5 nm and exhibited excellent photocatalytic performance [121]. Therefore, the 2D conduction path was shortened, which reduced the resistance to charge transfer. Combined the short transfer distance and low charge transfer resistance promoted the effective separation of photogenerated charges and improved photocatalytic efficiency. Finally, photocatalytic activity is also affected by the number of layers of 2DNMs [122]. Liu et al. arranged a few layers of MoS_2 vertically to obtain FLV-MoS_2 film [123]. By reducing the thickness of MoS_2 to a few layers or one layer, its energy band gap was increased from 1.3 eV to 1.55 eV (Fig. 8**c**). The increase in the band gap effectively enhanced the absorption of visible light. In addition, compared with the performance of FLV-MoS_2 and horizontal MoS_2, the vertical configuration had a higher photocatalytic disinfection rate because the vertical thin layer structure shortened the electron transfer distance, increased the hole separation efficiency, had

higher in-plane conductivity, and exposed more active edge sites on the FLV-MoS_2 film.

3.3.2. Organic matter surface modification

The weak electrochemical activity and easy agglomeration of 2DNMs greatly impair their photocatalytic performance, thus limiting their photocatalytic antibacterial applications. The modification of organic compounds, regardless of whether they are small organic molecules, macromolecules, or antimicrobial peptides, imparts different properties to 2DNMs, which have a profound impact on expanding their application [124–125].

For example, in a recent study, the recrystallization of perylene-3,4,9,10-tetracarboxylic diimide (PDINH) was performed on the surface of g-C_3N_4 nanosheets (Fig. 9**a**) [126]. The recrystallization of PDINH further enhanced the crystal structure of g-C_3N_4. The lattice spacing was reduced to 0.475 nm, and there were strong intermolecular π-π interactions between the layers (Fig. 9**b-d**). The optical absorption spectrum of the system was extended from 450 nm to 750 nm, and the band gap decreased. Therefore, the separation efficiency of the photoinduced carriers in the system was greatly improved. The photocatalytic performance of the modified g-

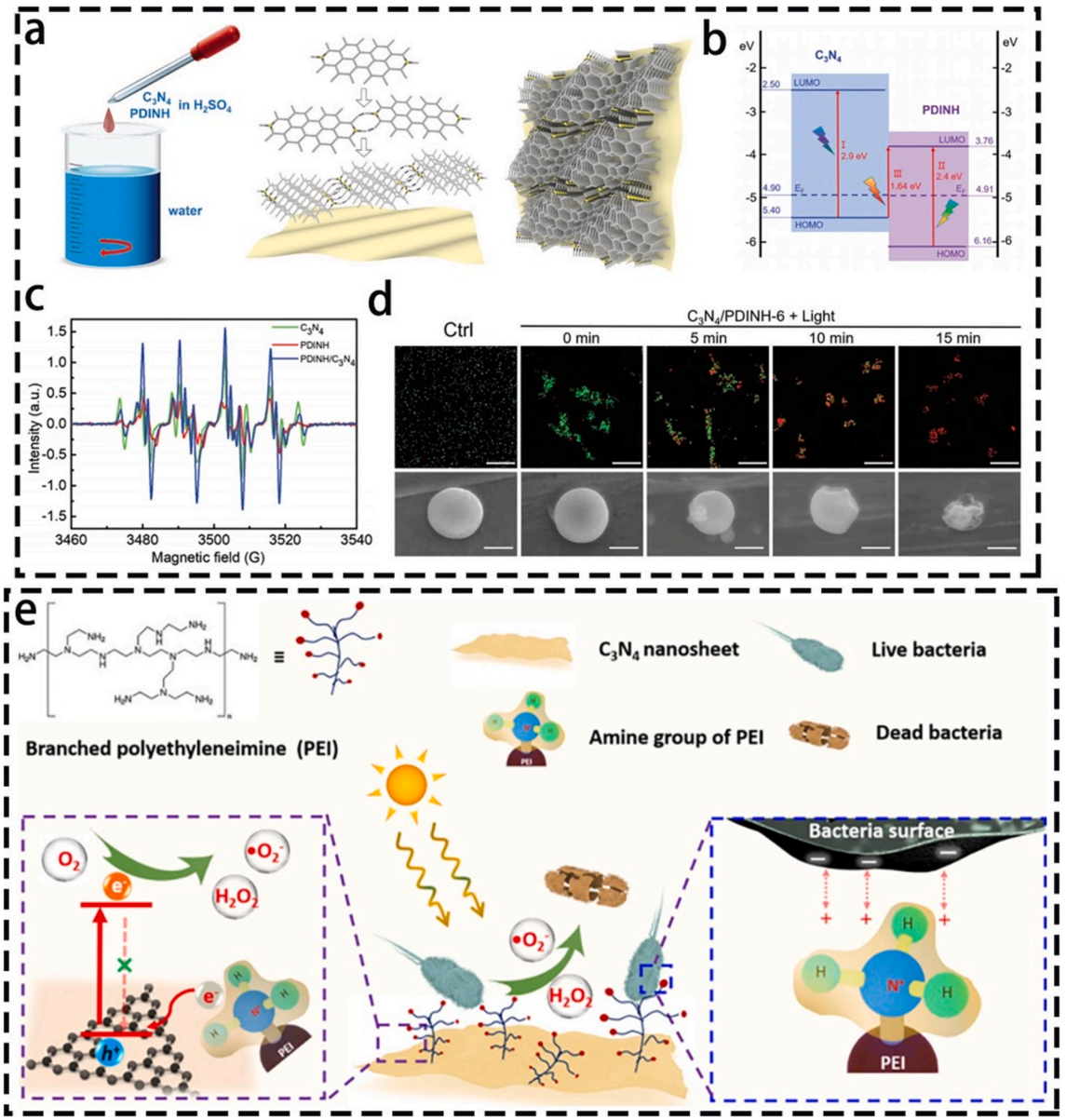

Fig. 9. (a) Schematic diagram of preparation method. (b) Band alignmnet of the C_3N_4/PDINH heterostructure. (c) ESR spectra upon irradiation of self-assembled PDINH, C_3N_4, PDINH/C_3N_4 heterostructure for detection of $\bullet O_2^-$ (d) Relative bacteria viabilities of *S. aureus* in different time intervals with C_3N_4/PDINH heterostructure and the corresponding SEM images [126]. Adapted with permission. Copyright 2019, Wiley-VCH. (e) Illustration of the roles of PEI on C_3N_4 for enhanced photocatalytic bactericidal activity [127]. Adapted with permission. Copyright 2020, Elsevier B.V.

C_3N_4 was also improved, which catalyzed water and O_2 to produce •OH, $•O_2^-$ and $^1O_2$, inducing serious damage to bacterial cells.

To solve the problem of incompatibility between materials and bacterial membrane potential, Zeng et al. modified 2D g-C_3N_4 using polyethyleneimine (PEI) through a simple immersion and electrostatic adsorption process [127]. As shown in Fig. 9**e**, PEI adjusted the electronic structure of g-C_3N_4 through molecular interactions, thereby promoting the separation of light-excited electrons and holes in g-C_3N_4, which led to the generation ROS ($•O_2^-$ and H_2O_2). The photocatalytic activity of the modified g-C_3N_4 was twice as high as that of the untreated group. In addition, the protonation of surface-grafted PEI in water induced a positive charge. Because of these properties, PEI interacted with the negatively charged membrane surface, which was beneficial for the adherence of bacteria to g-C_3N_4 and the improved inactivation of ROS. In addition, antimicrobial peptides were found to play an important role in changing the hydrophilic properties of materials. For example, Samak et al. prepared cyclic dodecapeptide (AMP) composed of various ratios of arginine (Arg) to tryptophan (Trp) [128], which was immobilized on a nanocomposite (RGO/β-MnO_2) hybridized by flaky reduced graphene oxide and β-phase manganese dioxide (β-MnO_2). The cationic nature of AMP facilitated electrostatic interactions with *Pseudomonas aeruginosa*-negative surfaces and improved binding to phospholipid membranes, resulting in an amphiphilic structure that facilitated adaptation between the membrane-water interfaces. Thus, the antibacterial properties of the system improved.

3.3.3. Organic photosensitizer modification

Organic photosensitizers absorb light radiation and excite the transition of electrons from the ground state to the short-lived singlet excited state, and then to the long-life triplet state. In the triplet state, electrons undergo direct reduction reactions with the substrate or electronic disintegration. When an organic photosensitizer is in contact with bacteria, the unsaturated phospholipids in the cell membrane are oxidized [129]. Organic photosensitizers also react with O_2 through energy transfer to produce $^1O_2$. The highly active $^1O_2$ rapidly reacts with biomolecules on the bacterial membranes, such as amino lipids, peptides, enzymes, and receptors, which induce damage [130].

Because of the abovementioned characteristics, some organic photosensitizers have been utilized to assist 2DNMs in achieving better photocatalytic antibacterial efficiency. Table 1 shows the combinations of some common organic photosensitizers and 2DNMs [131–145].

In 2DNMs, organic photosensitizers play a role in promoting absorption in the visible NIR region, which greatly enhances their light excitation ability. For instance, Shi et al. were the first to adopt the simple solution of a phase method to couple vanadyl-phthalocyanine (VOPc) and g-C_3N_4 (Fig. 10**a, b**) [138]. VOPc is a photosensitizer that broadens the absorption range of g-C_3N_4 from visible light to the NIR light region. Therefore, the optoelectronic activity and photocatalytic performance of g-C_3N_4 were significantly improved. Li et al. devised a composite system consisting of MoS_2, IR780, and arginine-glycine-aspartate-cysteine [144]. IR780 is a photosensitizer that adheres to the negatively charged MoS_2 layer through electrostatic bonding. Through atomic-level contact, it changed the electronic structure of the 2DNMs, which then affected the separation of electrons and holes generated by light. In addition, it produced $^1O_2$ under NIR light irradiation, which also played a positive role in antibacterials. Zhang et al. used sodium anthraquinone-2-sulfonate (AQS) to modify GO using a simple polymerization process (Fig. 10**c**) [145]. In composite materials, AQS showed a variety of biological activities as a photosensitizer, and GO provided a high surface area. Both were combined through π-π bond conjugation. Experimental results showed that AQS-GO had a more obvious photocurrent response, which indicated higher charge transfer efficiency and electron-hole pair separation efficiency. The electrons and holes generated on the CB and valence band (VB) of the AQS reacted with oxygen and H_2O to form $•O_2^-$ and •OH, respectively (Fig. 10**d**). In addition, the holes in the VB of GO

Table 1
The properties of organic photosensitizers compounded with 2DM.

Organic Photosensitizer	Two demension material	Irradiation wavelength	synthetic method	combination mode	Ref
TCPP	rGO, Bi_2WO_6	Visible light	hydrothermal, ultrasonic method	π-π stacking interactions	131
CuTCPP	g-C_3N_4	450–600 nm	Ultrasound, water bath	electrostatic, stacking interaction	132
*m*TCPP	g-C_3N_4	visible light	impregnation method	π-π stacking interactions	133
MTPPs	g-C_3N_4	visible light	hydrothermal method	π-π stacking interactions	134
ZnTcPc	g-C_3N_4	visible light	–	Coupling	135
DPyP	GO	White light	mix and stir	Electrostatic, coordination interaction	136
N-$CuMe_2Pc$	GO	visible light	ultrasonic assisted method	π-π stacking interactions	137
VOPc	g-C_3N_4	vis/ NIR	–	coupling	138
ZnTNPc	g-C_3N_4	visible light	impregnation method	coupling	139
Zn-*tri*-PcNc	g-C_3N_4	NIR	impregnation method	–	140
MPc	g-C_3N_4	UV–vis light	surface hydroxylinduced assembly process	coupling	141
ICG	MoS_2	808 nm	one-step hydrothermal method	covalently grafting, loading	142
ICG-CPPDN	rGO	NIR	mixture stirred	electrostatic interaction	143
IR780-PDA-RGDC	MoS_2	NIR	–	electrostatic binding forces	144
AQS	GO	visible light	ultrasonic treatment	π-π stacking interactions	145

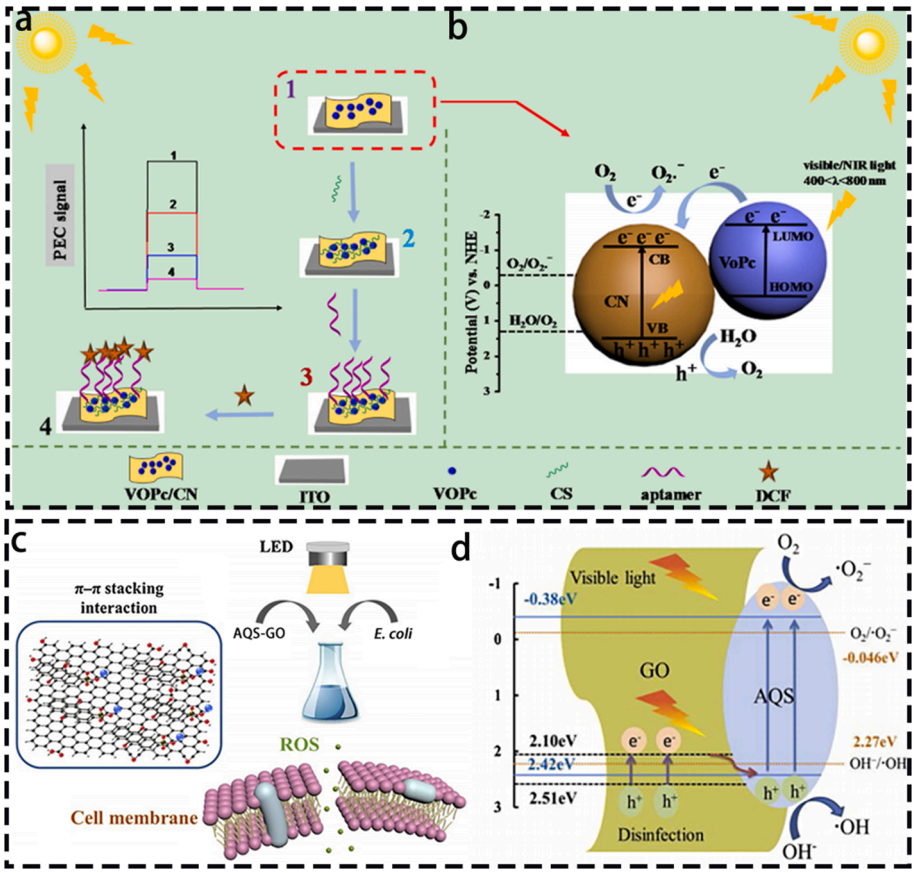

Fig. 10. (a) Fabrication process of PEC sensor for DCF detection under light irradiation of λ < 400 nm and (b) The electron-transfer process of VOPc/CN nanocomposites [138]. Adapted with permission. Copyright 2019, Elsevier B.V. (c) Schematic illustrating the plausible mechanism of antimicrobial activity of AQS-GO under visible light illumination. (d) Schematic mechanism of AQSGO for photo-generated ROS under visible light [145]. Adapted with permission. Copyright 2020, Elsevier B.V.

Table 2
The common defects in 2DMs.

2DNM	composite	Irradiation wavelength	synthetic method	defect type	Ref
GO	–	UV–visible	CVD	C-defects	147
Bi_2WO_6	–	solar light	solvothermal method	Bi-O dimer Vacancy pairs	148
Bi_2WO_6	Bi quantum dots	visible light	hydrothermal	O-Vacancy	149
Bi_2WO_6	–	visible light	ion exchange process	Bi-vacancy	150
BiOCl	–	380 nm	cracking the crystal	Pits defects	151
Bi_2MoO_6	Ce	visible light	hydrothermal	Crystal Defects	152
Bi_3O_4Br	–	Solar light	self-assembly strategy	Bismuth, O-Vacancy	153
BiOBr		visible light	hydrothermal	O-Vacancy	154
BiOBr	–	visible-light	solvothermal method	Bi-vacancy, Bi-O double, Bi-O-Bi triple atoms defect cluster	155
g-C_3N_4	3-AT prepolymers	420 nm	thermal polymerization	N-defects	156
g-C_3N_4	–	visible light	acid etching effect	N-defects	157
PCN	Cu	visible light	in-situ vapor diffusion	N-defects	158
g-C_3N_4	–	visible light	twice thermal treatment	surface C-defects	159
g-C_3N_4		visible light	thermal polymerization	structural defects	160
g-C_3N_4		solar light	one-pot KOH-assisted calcination	NH_x and N_{2C} Vacancy	161
g-C_3N_4	–	visible light	pyrolysis	edge site defects	162
MoS_2	–	–	electron irradiation	line defects	163
MoS_2	C, CdS	visible light	hydrothermal	S-Vacancies	164
MoS_2	Ru	visible light	hydrothermal	S-Vacancies	165
MoS_2	Ag_2S	visible light	Electrospray-deposited	Mo-rich edges defect	166

directly reacted with *E. coli*. Therefore, the composite system had stronger light-induced antibacterial properties compared with single components.

3.3.4. Surface defects

During the preparation and storage of 2DNMs, defective structures may occur [146]. Table 2 shows common types of defects in 2DNMs that enhance photocatalytic performance [147–166]. There are four types of defects in 2DNMs (Fig. 11). The first category is the vacancy of nonmetallic elements. The defect elements are mainly carbon (C), nitrogen (N), oxygen (O), and sulfur (S). For example, Guirguis et al. used electron cyclotron resonance microwave plasma CVD to grow vertically aligned graphene nanosheets on carbon fibers to produce graphene with carbon edge defects (Fig. 12**a**) [147]. The second type consists of cation vacancies, such as metal cation holes. Using the solvothermal method, Zhang et al. prepared Bi_2WO_6 nanosheets with a large proportion of crystal faces, and "Bi-O" dimer vacancy pairs were formed on the (1 0 0) high-energy plane (Fig. 12**b**) [148]. The third type consists of cavities or even pits. In ultrathin 2DNMs, atoms on adjacent surfaces escape from lattice points because of their low atomic escape energy. Guan et al. obtained ultrathin nanosheets with high solar photocatalytic activity by preparing BiOCl nanosheets with fully exposed (0 0 1) facets, which were more active (Fig. 12**c**) [151]. In addition, when the thickness of the nanosheet was reduced to the atomic level, more atoms escaped, causing the defects to change from the isolated single-atom defect "V_{Bi}" to the three-vacancy polyatomic defect "$V_{Bi}V_OV_{Bi}$." The fourth type comprises lattice defects, such as lattice dislocation, distortion, and disorder. During the preparation of Bi_2MoO_6, Dai et al. added metal cerium (Ce) to cause ion substitution and a charge compensation reaction process to generate O vacancies, thus distorting the crystal structure (Fig. 12**d**) [152]. These defects changed the local electronic structure of 2DNMs to a certain extent, thereby adjusting their physical and chemical properties and ultimately improving their photocatalytic performance.

Defects can increase the number of unsaturated active sites. During heterogeneous catalysis, a catalytic reaction preferentially occurs on coordinated unsaturated active sites, such as steps, edges, and protrusions on the surface of the material. [167]. First, unsaturated active sites greatly affect the electrochemical structure of a material. Di et al. successfully prepared Bi_3O_4Br nanosheets with single-cell thickness and bismuth defects using a self-assembly strategy with the surfactant polyvinylpyrrolidone (PVP) (Fig. 13**a**) [153]. The existence of Bi vacancies greatly reduced the formation energy of O vacancies, so as to achieve the purpose of regulating the generation of O vacancies (Fig. 13**b-d**). Because of its unique ultrathin atomic structure, surface defects were easily produced which changed the local atomic arrangement and affected its electronic structure. The combination of O vacancies and Bi vacancies led to the appearance of defective energy levels. A higher defect density led to the formation of defect levels near the energy band, thereby indirectly reducing the band gap. Therefore, under light irradiation, electrons were easily excited and transferred to CB. In addition, the more that defect states appeared in the band gap, the more likely was the surface separation center of carriers. This facilitated enhancing the electron trapping speed, thus promoting charge separation and prolonging the lifetime of the carriers. Hence, in this study, the photocatalytic efficiency was increased by 4.9 times compared with that in bulk Bi_3O_4Br.

Second, these active sites have been shown to contribute to the adsorption and desorption of reactants. Defective unsaturated coordination can provide many dangling bonds that preferentially adsorb reactants [168]. The adsorption of reactants is an important prerequisite for catalytic reactions that facilitate the transfer of interfacial charges. Local electrons at defect sites have the potential to feed electrons back to the adsorbed molecule, which activates some inert chemical bonds in the adsorbed molecule [154]. Qi et al. reported a double-defect strategy used to expand charge dynamics. The *in situ* vapor-phase diffusion method simultaneously generated N defects in polymer carbon nitride (PCN) and formed atomically dispersed single-point copper (Cu) at the DPCN-Cu's interface [158].

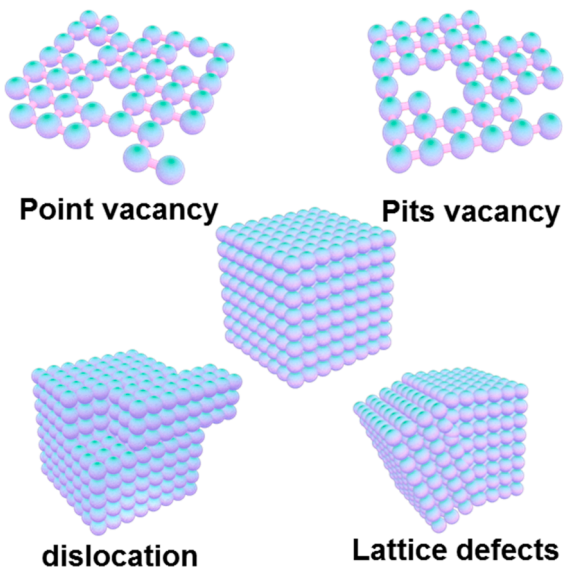

Fig. 11. The four kinds of defects in 2DNM.

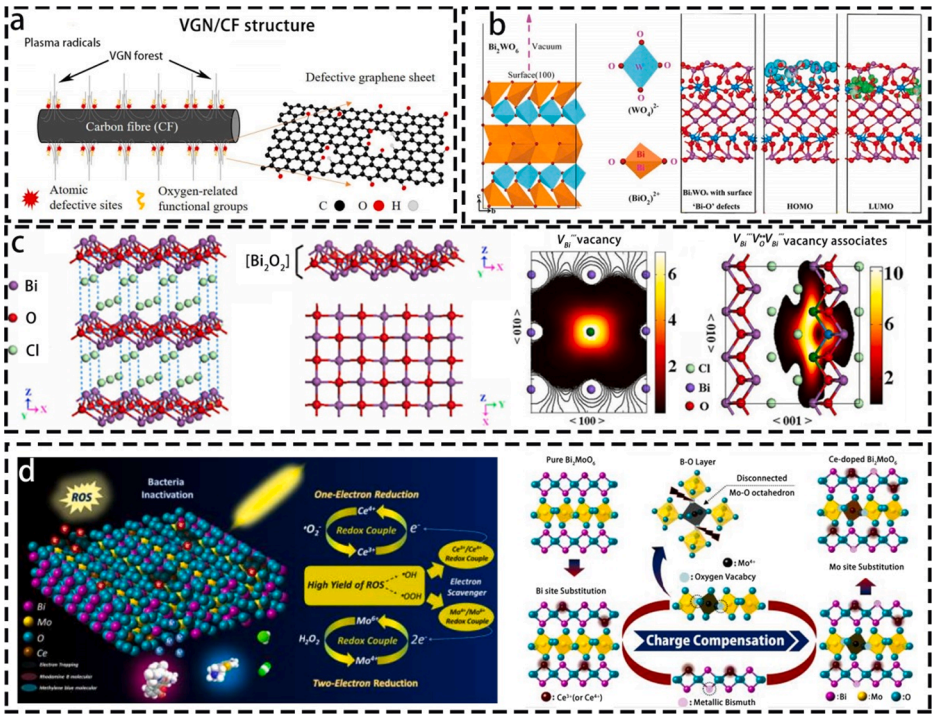

Fig. 12. (a) Schematic representation of the VGN/CF structure [147]. Adapted with permission. Copyright 2020, Elsevier B.V. (b) Schematic representation of the crystal structure of Bi_2WO_6. And the optimized model of Bi_2WO_6 with surface defects (left) [148]. Adapted with permission. Copyright 2015, Wiley-VCH. (c) Schematic representation of the crystal structure of BiOCl, Three-dimensional projection and $[Bi_2O_2]^{2+}$ layers along with the [0 1 0] and [0 0 1] direction, respectively. And the schematic representations of trapped positrons of $V_{Bi}^{'''}$ defect and $V_{Bi}^{'''}V_O^{\bullet\bullet}V_{Bi}^{'''}$ vacancy associates, respectively [151]. Adapted with permission. Copyright 2013, American Chemical Society. (d) Schematic representation of the photocatalytic degradation of dyes and photoinactivation of bacterium by Ce-doped Bi_2MoO_6 photocatalyst. And illustration of the possible formation process of crystal defects in Ce-doped Aurivillius Bi_2MoO_6 structure [152]. Adapted with permission. Copyright 2016, American Chemical Society.

Surface N defects extended light absorption to long wavelengths through sub band absorption. The Cu-N bond formed by the interaction between N and single-point Cu facilitated the transfer of photoelectrons. Therefore, highly dispersed active sites effectively captured electrons, and were used for the adsorption and activation of reactant molecules, which improved surface reaction efficiency and further improved photocatalytic activity. Therefore, DPCN-Cu photocatalytic efficiency was about 4.5 times higher than that of PCN, regardless of whether it was in the visible light range or the full light range.

Finally, the introduction of defects has been found to adjust the band gap of the semiconductor, expand the light absorption range, regulate the generation of photoexcitons, affect the separation and transmission of electrons and holes, and promote the process of gas adsorption and activation, thus promoting the catalytic reaction and improving catalytic efficiency [169]. For example, Xie et al. used a one-pot calcination method to prepare polymer carbon nitride with two NH_x and N_{2C} vacancies (Fig. 14**a, b**) [161]. NH_x and N_{2C} holes on the two electron paths accelerated the separation of the photoexcited charges. The former led to the accumulation of surface carriers for the subsequent reduction reaction with O_2, while the latter was mainly used to activate O_2. In addition, the local deep energy level generated by the N_{2C} vacancy broadened the absorption range to the visible light region. The local shallow energy level generated by the NH_x vacancy was slightly higher than the maximum value of VB, which increased the mobility of the carriers and extended the free path of carrier diffusion. Therefore, NH_x vacancies promoted the separation of photogenerated carriers, resulting in higher electron density. The synergy between the two defects improved the photocatalytic performance of the system. The optimized sample showed a 15-fold increase in catalytic performance under solar irradiation.

3.3.5. Heteroatom doping

Heteroatom doping is a valid method for tuning the physical and chemical performance of 2DNMs [170]. Regardless of whether it replaces atoms in the unit cell or enters the crystal lattice through heteroatom doping, changes in the properties of 2D materials are induced. The method of doping atoms can effectively tune the band gap width and electronic structure of the material, thereby affecting photocatalytic performance [171]. As shown in Table 3, the carbon (C), nitrogen (N), oxygen (O), and sulfur (S) atoms are common heteroatom elements used for doping in the 2DNMs [172–185].

Xiong et al. used glucose as a carbon source to fabricate C-doped $(BiO)_2CO_3$ (CBCO) nanosheets and self-assembled microspheres using a simple hydrothermal method (Fig. 15**a**) [172]. When the amount of doped carbon element increased in the crystal structure of BCO, a localized state on the edge of the VB appeared, and both the potential of CB and the band gap of CBOC decreased, resulting in enhanced visible light absorption (Fig. 15**b-d**). In addition, carbon doping tended to form more defect sites in the crystal lattice, which

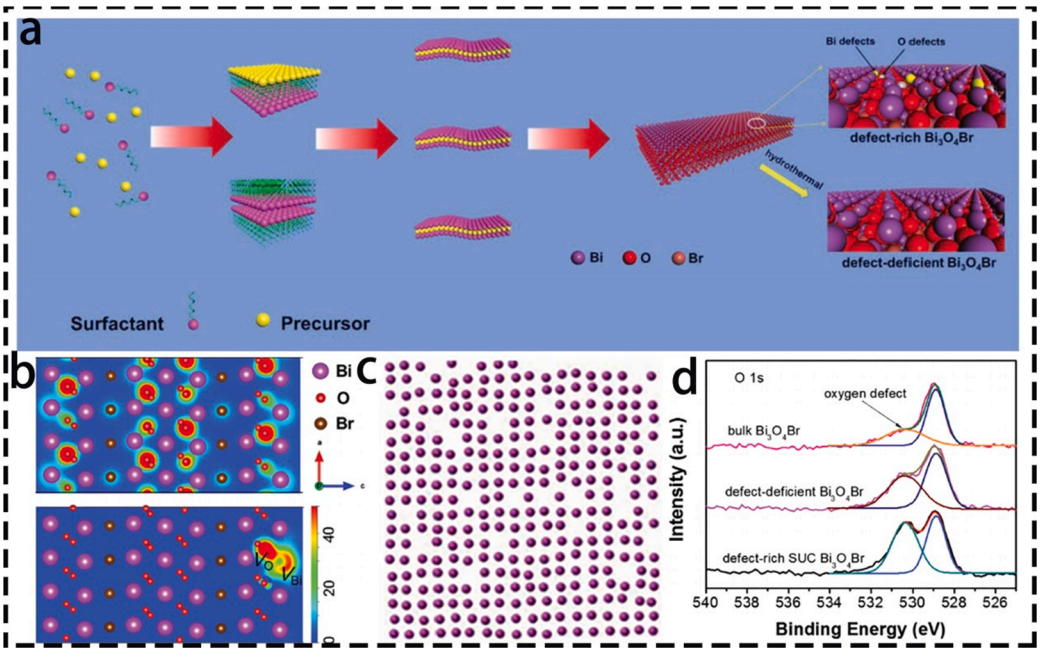

Fig. 13. (a) Illustration of molecular assembly for the formation of single-unit-cell Bi_3O_4Br nanosheets with or without defects. (b) Schematic representations of trapped positrons of defect-deficient Bi_3O_4Br and defect-rich SUC Bi_3O_4Br, respectively. (c) Structural model to show surface Bi defects. (d) The O 1 s XPS spectra [153]. Adapted with permission. Copyright 2019, Wiley-VCH.

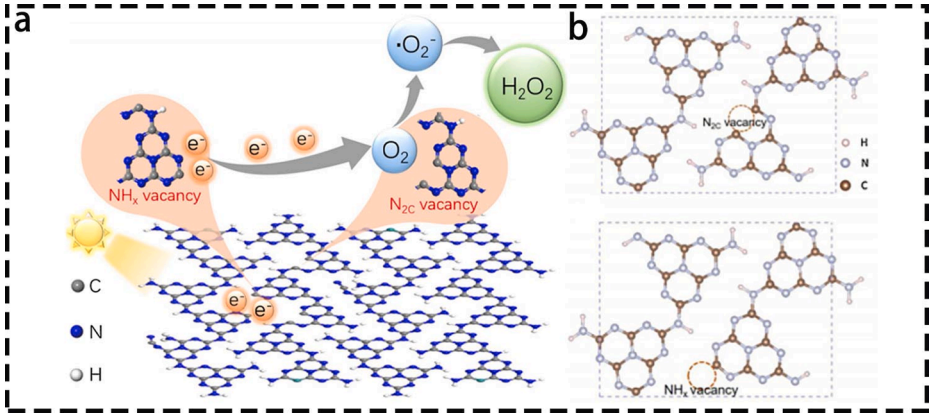

Fig. 14. (a) Schematic diagram of efficient solar-to-H_2O_2 conversion by polymeric carbon nitride with two types of cooperative nitrogen vacancies (NH_x vacancy and N_{2C} vacancy). (b) Density-functional theory calculations. Structure models of polymeric carbon nitride with N_{2C} vacancy and with NH_x vacancy [161]. Adapted with permission. Copyright 2019, Elsevier B.V.

could be employed as active site centers to promote the separation of electrons and holes. In addition, the layered structure on the surface of the nanomicrospheres allowed for the multiple scattering and reflection of incident light, thus increasing the light absorption efficiency. Moreover, this structure facilitated the diffusion of reaction intermediates and products to accelerate the reaction rate. The photocatalytic activity of CBCO was effectively enhanced and steadily improved, far exceeding that of undoped BCO. Zhang et al. fabricated a highly efficient porous O-doped g-C_3N_4 photocatalytic catalyst [177]. The catalyst ensured the complete binding of melamine to its hydrolysate by forming uniform supramolecular assemblies during the hydrothermal process. On a g-C_3N_4 network, nanopores and oxygen (O) doping were uniformly distributed on the surface. The porous structure and the introduction of heteroatoms (O) increased the number of active sites and tuned the electronic structure, thereby narrowing the energy band and enhancing its light-harvesting ability. In another study, Feng et al. synthesized a simple heat-treatment strategy to prepare S-doped h-BN and tuned the band structure and interlayer distance through doping (Fig. 15**e, f**) [181]. Compared with the original h-BN, the performance of the optimized S-doped h-BN was greatly improved because of the doping of sulfur (S). The doping amount of S adjusted the band gap of the h-BN. The *p*-orbital and *d*-orbital of S participated in the hybridization so that new VB and CB edges formed in h-BN. As a result, the potential of CB decreased, the band gap shrunk, the absorption spectrum of h-BN red-shifted, and the light absorption performance

Table 3
The common heteroatom doping in 2DMs.

2DM	composite	Irradiation wavelength	synthetic method	Dopant atoms type	Ref
$(BiO)_2CO_3$	Cu	visible light	hydrothermal method	C-doped	172
Bi_2WO_6		visible light	hydrothermal	N-Doped	173
graphene	RhCrOx/STO:Al	visible light	hydrothermal	N-doped	174
Ti_3C_2	TiO_2	UV–visible	low temperature calcination	N-doped	175
MoS_2	Pt	UV–visible	one-step solvothermal	N-doped	176
g-C_3N_4	–	visible light	solvothermol route	O-doped	177
g-C_3N_4	–	visible light	hydrothermal	O-doped	178
g-C_3N_4	–	UV–visible	thermal condensation	P-doped	179
g-C_3N_4	CoS_2	visible light	hydrothermal and sulfidation processes	S-doped	180
h-BN	–	visible-light	heat treatment strategy	S-doped	181
rGO	ZnS	sunlight	hydrothermal	S-doped	182
Bi_2WO_6	Ce		one-step hydrothermal	F-doped	183
Bi_2MoO_6	–	visible light	one-pot solvothermal	F, Cl, Br, I-doped	184
g-C_3N_4	–	visible light	Heat treatment	P,S,O-doped	185

increased (Fig. 15**g**). Because many polar B-S bonds increased the interaction between layers, the interlayer distance of h-BN was compressed. Abundant S-doped sites and shortened layer stacking distance might be the main reasons for promoting charge mobility and surface reactivity, which ultimately led to improved photocatalytic activity.

3.3.6. Building heterojunctions

The construction of heterojunction structures can significantly improve the photocatalytic performance of materials. According to the classification of materials, heterojunction structures are categorized as metal/2DNMs or semiconductor/2DNMs [186,187].

3.3.6.1. Precious metal/2DNM heterojunction. The combination of precious metals (Au or Ag) with 2DNM significantly improves the photoreactivity of 2DNMs because of two main characteristics: the Schottky junction and localized surface plasmon resonances (LSPR) [188,189]. In the Schottky junction, precious metals capture light-emitting electrons from 2DNMs and then participate in the reduction reaction [190]. As shown in Fig. 16, a Schottky junction is formed when the 2DNM is in close contact with the metal, and their E_{Fermi} changes simultaneously, and then reaches equilibrium in a uniform constant value. As a result, the energy band of 2DNM is bent and deformed, and a potential energy difference appears. Captured by the metal, the electrons from the 2DNM cannot return because they are blocked by the Schottky barrier. Hence, the Schottky junction further accelerates the transfer of the photogenerated electrons to improve the efficiency of separation from holes, accelerate photogenerated carrier dynamics, and improve the photocatalytic performance of 2DNM [191].

Cai et al. prepared an Ag_3PO_4/Ti_3C_2 Schottky catalyst, and the synergy between the two components effectively improved performance (Fig. 17**a, b**) [190] for the following reasons: 1) the surface of Ti_3C_2 had a large number of hydrophilic functional groups, which had a strong interaction force with Ag_3PO_4, facilitating charge migration and separation; 2) highly active electrons accumulated on the surface of titanium (Ti) sites participated in the reduction reaction to generate •OH; 3) the difference in Fermi levels between Ti_3C_2 and Ag_3PO_4 induced electrons to flow from Ag_3PO_4 to Ti_3C_2 until a uniform Fermi level was formed, creating an embedded electric field that was beneficial to the effective transfer of electrons to the surface of Ti_3C_2. As a result, Ag_3PO_4/Ti_3C_2 showed better light absorption, higher photoelectric properties, and photocatalytic activity.

Schottky heterojunctions often occur in multiple heterojunctions. For example, Zhang et al. synthesized a 2D flat SnS_2/rGO/Ag nanocomposite with multiple junctions using a hydrothermal method and ultraviolet reduction [191]. Because the conjugated structure of rGO provided abundant delocalized electrons, the holes on the VBs of SnS_2 were rapidly transferred to the rGO surface under illumination, thereby facilitating the transport of charge carriers. The photoelectrons of SnS_2 were transferred to Ag clusters because of the formation of the Schottky junction. Photoinduced electrons on Ag captured H_2O and O_2 to produce ROS. The holes on the surface of rGO generated •OH radicals by reacting with H_2O. Based on the synergy between the ternary heterojunctions, rGO and Ag were vehicles of holes and electrons, which promoted their separation, extended the life of carriers, and improved the photocatalytic activity of the system. Han et al. prepared hydrophilic porous composite nanofiber membranes through electrospinning, followed by hydrolysis and thermal reduction treatments, in which polyamidoxime (PAO)-grafted rGO was used as an additive to adsorb heavy metals, and PVP was used as a pyrogen (Fig. 17**c, d**) [192]. Because some of the silver ions adsorbed by PAO were reduced to elemental silver, there were two Schottky junctions (rGO/Ag and Ag^+/Ag) in the PAN-based nanofiber membrane. The light absorption of the system was enhanced, and the photoelectrons were quickly transferred from Ag to rGO-g-PAO@Ag^+ to promote their separation and improve the photocatalytic sterilization effect (Fig. 17**e-h**).

It has been shown that the surface plasmon resonance (SPR) effect can strengthen the photocatalytic performance of 2DNMs (Fig. 18**a**). Surface plasmon photocatalytic material is a metal–semiconductor composite photocatalytic based on the SPR effect of precious metal nanoparticles (NPs) [193]. Of note is the special SPR effect of LSPR (Fig. 18**b**). The main determinant of its occurrence is the size of the metal nanostructure. Generally, the particle size must be smaller than the mean free path of electrons and the wavelength of incident light. The unique LSPR effect of precious metal NPs can greatly expand the absorption spectrum range, thereby obtaining more energy to excite electrons, promoting their separation from holes, and ultimately improving the solar energy

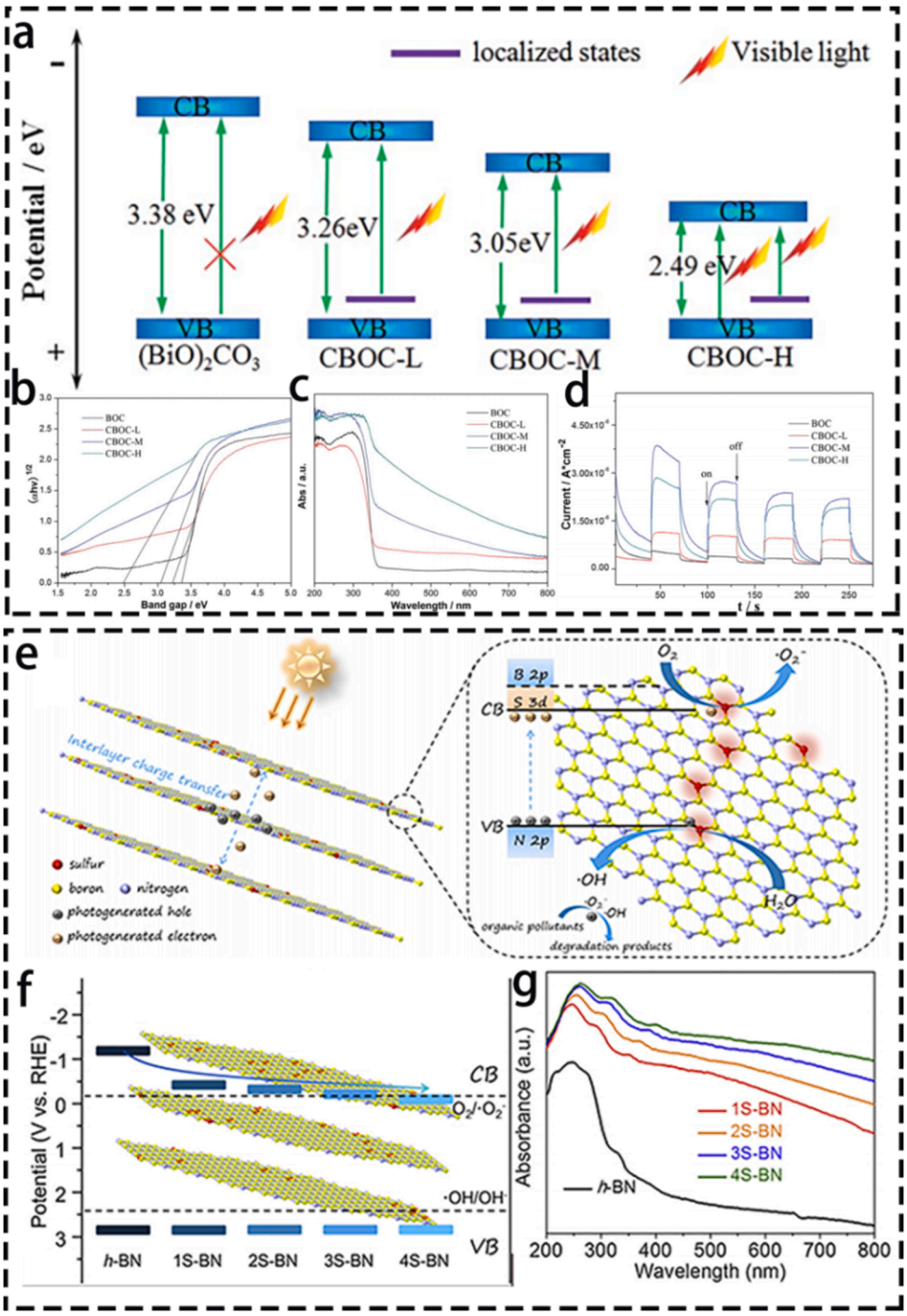

Fig. 15. (a) Proposed schematic energy band structure of the as-prepared samples. UV–vis DRS (b) and plots of $(ahv)^{1/2}$ vs. photon energy (c) of the four as-prepared samples. (d) Transient photocurrent density of the as-prepared samples [172]. Adapted with permission. Copyright 2015, Royal Society of Chemistry. (e) Schematic diagram for the interlayer charge transfer, band structure change and 2,4-DCP degradation process of S-BN photocatalysts. (f) The schematic diagram for the band variations of h-BN and xS-BN samples. (g) UV–vis DRS for h-BN and xS-BN samples [181]. Adapted with permission. Copyright 2019, Elsevier B.V.

conversion efficiency and the photocatalytic performance of the materials [194].

Studies had shown that Ag/AgO synthesized *in situ* enhanced the photocatalytic performance of g-C_3N_4 (Fig. 19**a**) [195]. Compared with g-C_3N_4, due to the SPR effect of nano-Ag and AgO, the composite exhibited a stronger visible light absorption intensity, and its band gap was also significantly reduced (Fig. 19**b, c**). In addition, the decreased charge transfer resistance of the composite material accelerated the charge transfer. Because the potential of g-C_3N_4 CB was higher than that of AgO, the excited electrons were first

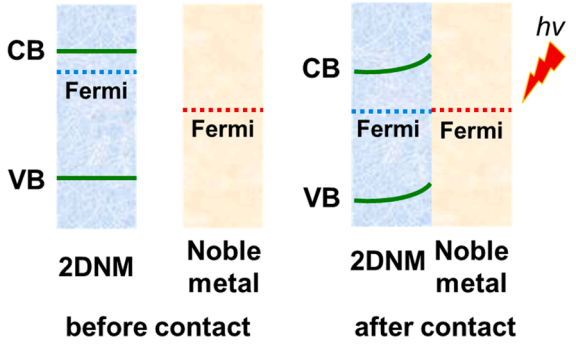

Fig. 16. Schottky Junction schematic.

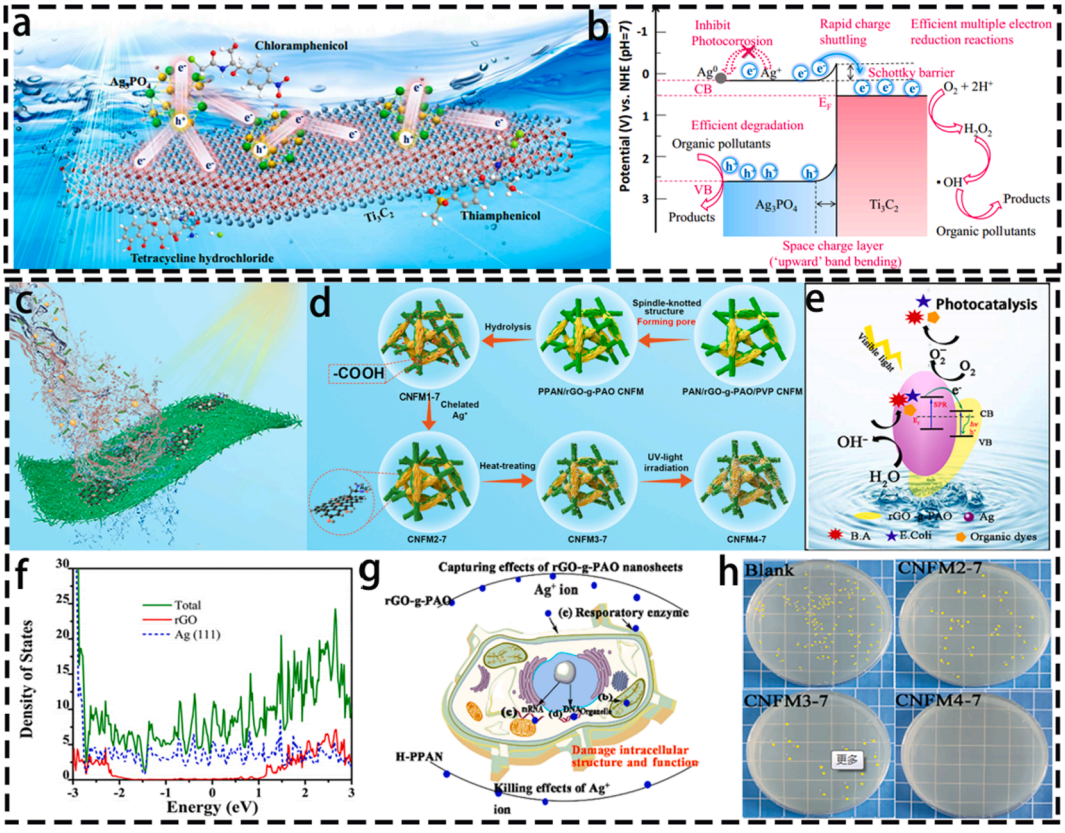

Fig. 17. (a) The photocatalysis schematic diagram of Ag_3PO_4/Ti_3C_2. (b) The mechanism of photodegradation and anti-photocorrosion of Ag_3PO_4/Ti_3C_2 Schottky catalyst [190]. Adapted with permission. Copyright 2018, Elsevier B.V. (c) The photocatalysis schematic diagram of rGO-g-PAO@Ag^+/Ag. (d) Scheme of the Fabrication Procedure of H-PPAN/rGO-g-PAO@Ag^+/Ag CNFM. (e) Hypothetical photocatalytic mechanism of CNFM4-7. (f) DOS for Ag and rGO Schottky junction. (g) Schematic of the hypothetical synergistic antibacterial mechanism of the rGO-g-PAO@Ag^+/Ag nanosystem. (h) The results of colony culture after 6 h of irradiation for the blank group and the detection system containing CNFM2-7, CNFM3-7 and CNFM4-7. [192]. Adapted with permission. Copyright 2019, American Chemical Society.

transferred to the CB of AgO and then to Ag. The VB potential of AgO was lower than that of g-C_3N_4, so the holes migrated smoothly to g-C_3N_4. Hence, the carriers were well separated in the composite system, which helped generate a large number of active substances with oxygen and H_2O, which greatly increased the photocatalytic bactericidal performance of g-C_3N_4. In another study, Xie et al. reduced Ag^+ *in situ* to obtain Ag/GO so that AgNPs were uniformly distributed on the nanosheets, and then type I collagen was deposited on the surface to improve its biocompatibility (Fig. 19**d**) [196]. The results showed that GO had a large specific surface area and many negatively charged functional groups, which was beneficial in uniformly dispersing AgNPs through electrostatic adsorption and avoiding agglomeration. Light irradiation induced the SPR effect of AgNPs to generate electrons. In addition, by taking advantage of the high conductivity of GO, these excited electrons were quickly transferred to the surface, avoiding interactions with holes.

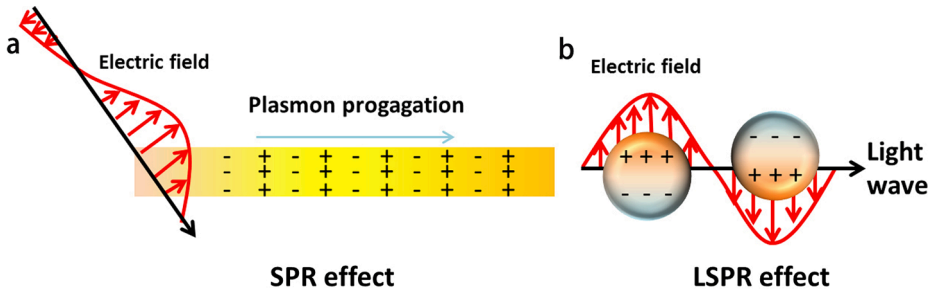

Fig. 18. (a) The schematic of SPR effect. (b) The schematic of LSPR effect.

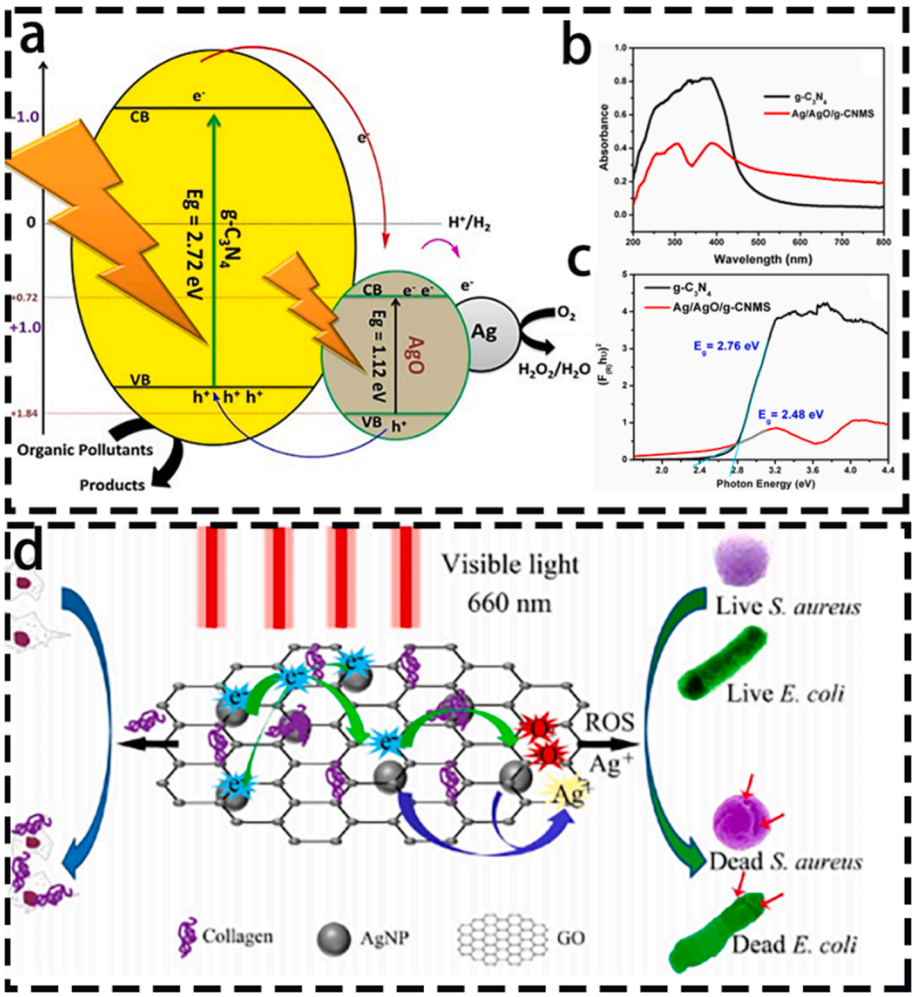

Fig. 19. (a) Schematic illustration of electron transfer in Ag/AgO/g-CNMS composite (b) UV–Vis absorption spectra and (c) Kubelka-Munk plots of g-C_3N_4 and Ag/AgO/g-CNMS [195]. Adapted with permission. Copyright 2017, Elsevier B.V. (d) Schematical Illustration of cytocompatibility and synergistic bacteria killing through the innate antimicrobial ability of Ag^+ and the photodynamic effects of AgNPs in GO/AgNPs/Collagen hybrid coating using 660 nm visible light [196]. Adapted with permission. Copyright 2017, American Chemical Society.

Finally, the electrons reacted with oxygen and H_2O to generate ROS to eliminate bacteria. The results showed that after 20 min of irradiation, the bactericidal effects on *E. coli* and *Staphylococcus aureus* (*S. aureus)* were 96.3% and 99.4%, respectively.

3.3.6.2. Semiconductor/2DNM heterojunction. In addition to the above strategies for enhancing photocatalytic antibacterial activity, a heterojunction composed of semiconductor photocatalysts and 2DNM was developed to obtain high antibacterial efficacy [197].

Heterojunctions that establish close contact between dissimilar semiconductors are a current topic because they accelerate electron transfer, thereby indirectly promoting the separation of electrons and holes [198]. Depending on different material types and band gaps, heterojunctions are categorized into four types: conventional, p-n, Z-scheme, and S-scheme heterojunctions. Each heterojunction has profound effects on its own charge transfer properties [199]. Table 4 shows typical semiconductor/2DNMs heterojunctions that enhance the photocatalytic performance of 2DNMs [200–217].

3.3.6.2.1. Conventional heterojunctions. There are three types of traditional heterojunctions: spanning gaps (type I), staggered gaps (type II), and broken gaps (type III) [201]. In the type I heterojunction photocatalyst (Fig. 20**a**), the CB and VB of semiconductor A are higher and lower than semiconductor B, respectively. According to this principle, electrons transfer from a low electric potential to a high electric potential, and holes transfer from a high electric potential to a low electric potential. Electrons and holes accumulate at the CB and VB of semiconductor B, respectively. The combination probability of the two is relatively high, so effective separation cannot be achieved. In addition, redox reactions occur in semiconductors with lower potentials, which reduce the redox capability of heterojunction photocatalysts. In the type II heterojunction photocatalyst, the CB and VB of semiconductor A are both higher than those in semiconductor B (Fig. 20**b**) [202]. Therefore, the photogenerated electrons are transferred to semiconductor B, and the photogenerated holes are transferred to semiconductor A. The electrons and holes accumulate in the two materials, and the probability of their combination is reduced, thereby enhancing the redox activity of the photocatalyst. In the type III heterojunction photocatalyst, the band gap distribution of the two is extreme. That is, the VB of semiconductor A is higher than the CB of the semiconductor, resulting in band gaps that cannot overlap (Fig. 20**c**). Therefore, there is no electron transfer between the two semiconductors, which is unsuitable for improving the performance of the photocatalyst. Therefore, among the three types of heterojunctions, the type II heterojunction photocatalyst improves the separation efficiency of electrons and holes, thus improving the performance of the photosensitizer [203].

Cai et al. used a one-pot synthesis strategy to load titanium dioxide (P25) and metal palladium (Pd) into g-C_3N_4 to form a type II heterostructure for photocatalysts (Fig. 21**a**) [200]. When the type II heterojunction was formed, the electrons generated by the light excitation of g-C_3N_4 were directionally transferred to the surface of P25 and then to Pd, while the holes were transferred to g-C_3N_4, thereby preventing recombination of the carriers (Fig. 21**b-c**). Therefore, the catalytic activity of the g-C_3N_4/P25(N)-Pd system was significantly enhanced. Under the illumination of visible light and full-wave light, catalytic performance was enhanced by 8.7 times and 24.5 times compared with pure g-C_3N_4, respectively. In another study, a microwave-assisted hydrothermal reaction was used to *in situ* synthesize zinc sulfide (ZnS) on the surface of g-C_3N_4 to form a type II heterojunction [202]. Excited by visible light, g-C_3N_4 generated excited electrons and holes. Because of the low CB potential energy of ZnS, the electrons on g-C_3N_4 CB were transferred easily to the CB of ZnS to achieve the separation of electrons and holes. Finally, the performance of the system was enhanced 4.5 times compared with pure g-C_3N_4. Type II heterojunctions can also be formed between 2DNMs. For example, Li et al. used an *in situ* solvothermal method to prepare the type II heterojunction Bi_2MoO_6/g-C_3N_4 [203]. The exfoliated nanosheet g-C_3N_4 had a large specific surface area and numerous active sites on the surface, which was beneficial for the close combination of g-C_3N_4 and Bi_2MoO_6, thereby

Table 4
The typical semiconductor/2DM heterojunctions.

2DM	composite	Irradiation wavelength	synthetic method	type	Improve photocatalytic performance	Ref
g-C_3N_4	P25	visible, full wave light	calcinated	Type-II	8.7 and 24.5 times	200
g-C_3N_4	AgX (X = Cl,Br)	visible light	sonication, deposition	Type-II	4.2 times	201
g-C_3N_4	ZnS	visible light	microwave hydrothermal	Type-II	4.5 times	202
g-C_3N_4 Bi_2MoO_6	–	visible light	*in situ* solvothermal	Type-II	4 times	203
Bi_2WO_6	Cu_2ZnSnS_4	visible light	secondary solvothermal	Type-II	3 times	204
BiOI, rGO	–	visible light	solvothermal reactions	p-n	2 times	205
g-C_3N_4	$CuBi_2O_4$	visible light	calcining method	p-n	4 times	206
Bi_2WO_6	$MoSe_2$	visible light	bath sonication method	p-n	6 times	207
$Bi_2O_2CO_3$/BiOCl	–	visible light	homogeneous precipitation	p-n	1 ~ 2 times	208
Bi_2MoO_6	$CuBi_2O_4$	visible light	solvothermal	p-n	3 ~ 6 times	209
Bi_2MoO_6	poly(benzothiadiazole)	visible light	*in situ* palladium-catalyzed cross-coupling	Z-scheme	3 ~ 4 times	210
g-C_3N_4	TiO_2	visible light	one-step hydrothermal	Z-scheme	4 times	211
rGO	TiO_2, WO_3	visible light	hydrolysis-hydrothermal	Z-scheme	2 times	212
MoS_2	WS_2, WO_{3-x}	visible -NIR light	hydrothermal, heat-treatment	Z-scheme	4 times	213
BP, Bi_2WO_6	–	visible light	exfoliated, hydrothermal	Z-scheme	9.15 times	214
Bi_2MoO_6	MO (M = Cu, $Co_{3/4}$, or Ni)	visible light	hydrothermal	Z-scheme	2 ~ 3 times	215
BiOBr/ $BiOAc_{1-x}Br_x$	–	visible light	co-precipitation	S-scheme	2 ~ 3 times	216
g-C_3N_4	$Cd_{0.5}Zn_{0.5}S$	visible light	annealing	S-scheme	9 times	217

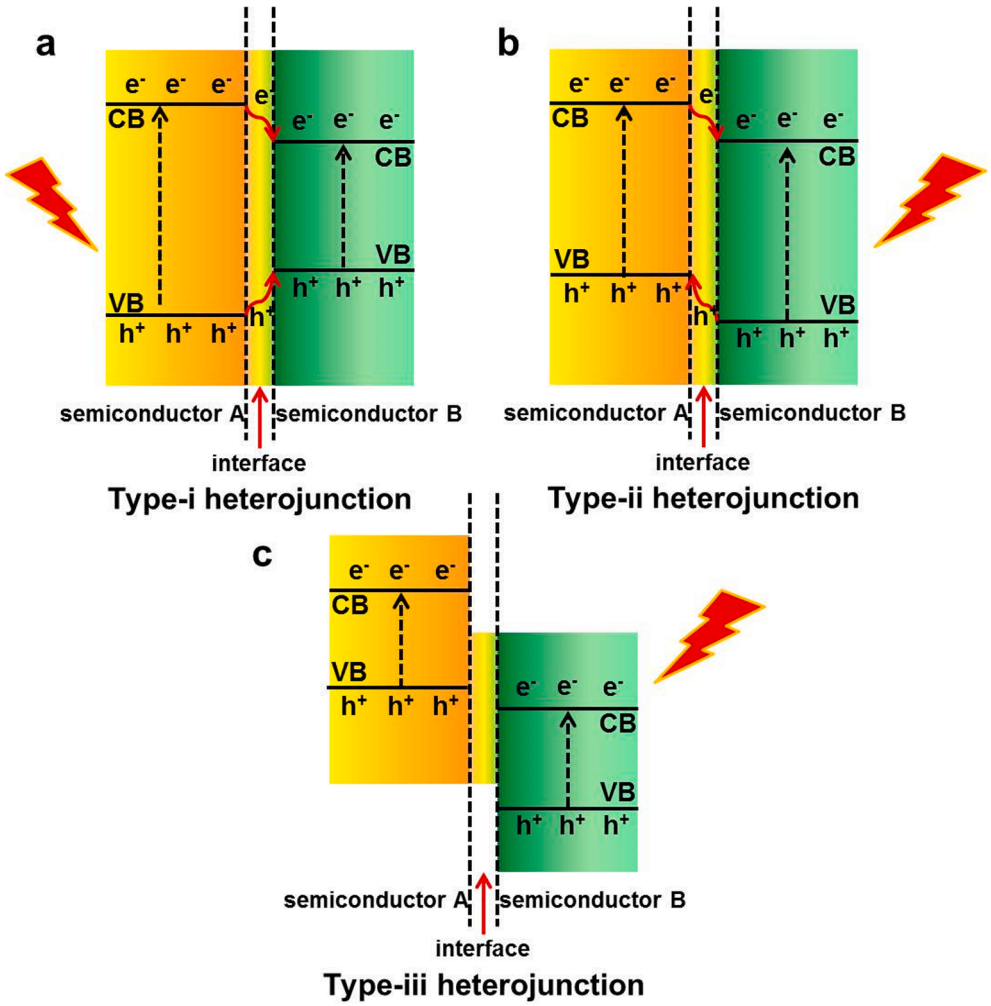

Fig. 20. The schematic diagram of conventional heterojunction: (a) type-I, (b) type-II, (c) type-III heterojunction.

shortening the diffusion distance of the photogenerated charges. The results showed that the electrons generated in the CB of g-C_3N_4 were transferred to Bi_2MoO_6 after excitation by light radiation. Moreover, the holes in the VB of Bi_2MoO_6 moved to g-C_3N_4, which promoted the separation of the photoelectrons and holes, involving them in the subsequent sterilization process. The experimental results showed that the 20%-Bi_2MoO_6/g-C_3N_4 heterojunction had the best photocatalytic disinfection effect on bacteria and that the holes were the dominant active substances in deactivating *E. coli*.

3.3.6.2.2. p-n heterojunction. Ideally, a type II heterojunction can separate light-excited electrons and holes to avoid recombination. However, in practical applications, the carrier separation speed caused by a type II heterojunction is not as high as its recombination speed [204]. Thus, a unique p-n heterojunction has been extensively studied [205]. In this type of heterojunction, a weak electric field is formed at the interface (Fig. 22). Under the influence of this field, the migration rate of electrons and holes to the heterojunction is accelerated, which is beneficial for catalytic applications. Specifically, because the Fermi levels of the p-type semiconductor and the n-type semiconductor are close to their corresponding VB and CB, respectively, when the two are in contact, the electrons near the n-type semiconductor interface and the holes on the p-type semiconductor interface spontaneously spread to the other side until the E_{Fermi} balance of the system is reached [207]. This also causes the VB and CB of the p-type and n-type semiconductors to bend and deform, eventually shifting to high- and low-level potentials, respectively. The spontaneous movement of interfacial electrons and holes eventually lead to the formation of an internal electric field. When irradiated, the p-type and n-type semiconductors are sufficiently excited to generate carriers. Influenced by the internal electric field, the excited electrons and holes migrate quickly to the CB of the n-type semiconductor and the VB of the p-type semiconductor, respectively, which resulted in a higher separation efficiency of carriers compared with the type II heterojunction [208].

Guo et al. synthesized Cu_2ZnSnS_4/Bi_2WO_6 (CZTS/BWO) p-n heterojunctions using a brief secondary solvothermal process (Fig. 23**a, b**) [204]. After the two were in contact, the imbalance of E_{Fermi} energy led to the migration of carriers until equilibrium was reached. Therefore, the interface between BWO and CZTS was positively and negatively charged, respectively, forming an intercalation electric field and bending the band edges of both. After excitation by light radiation, the electrons generated by CZTS were

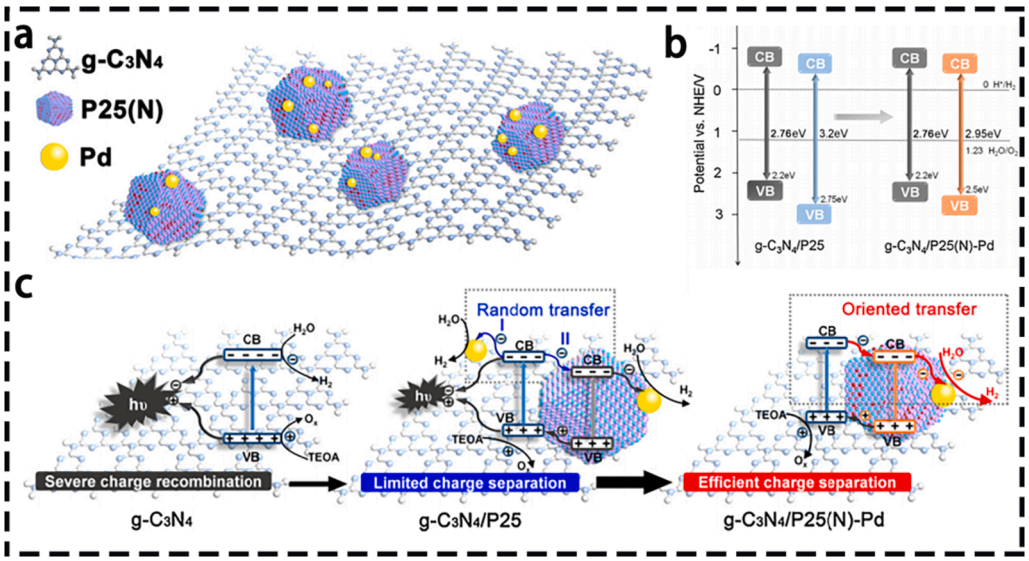

Fig. 21. (a) The diagram of type II heterostructured g-C_3N_4/P25(N)-Pd (For interpretation of the references to colour in this figure legend, the reader is referred to the web version of this article.). (b) The illustration of bandstructures for g-C_3N_4/P25 and g-C_3N_4/P25(N)-Pd, respectively. (c) Plausible mechanisms photocatalytic hydrogen evolution over g-C_3N_4, g-C_3N_4/P25, and g-C_3N_4/P25(N)-Pd, respectively [200]. Adapted with permission. Copyright 2019, Elsevier B.V.

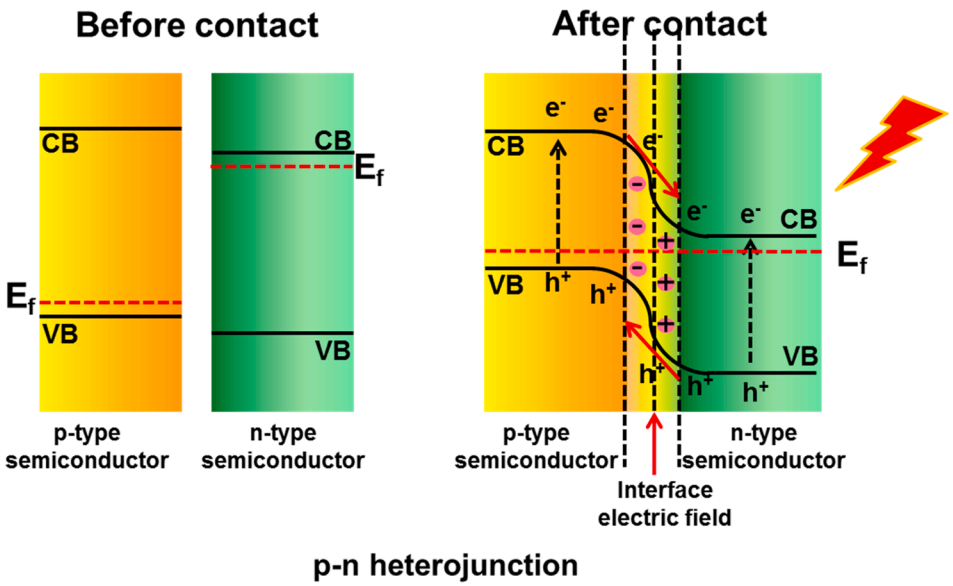

Fig. 22. The schematic diagram of p-n heterojunction before the contact and after contacr between p-type and n-type semiconductor.

transferred to BWO under the drive of electric field force, and the holes on BWO were transferred to CZTS. After the transfer, large numbers of accumulated electrons and holes had strong reducibility and oxidability, thereby participating in the redox reaction to reduce or oxidize O_2 and H_2O to $\bullet O_2^-$ and $\bullet OH$, respectively (Fig. 23**c, d**). Because of this synergy, the photocatalytic efficiency of the heterojunction was five and two times higher than that of the simple CZTS and BWO, respectively. The photocatalytic performance of 2D Bi_2WO_6 was enhanced by forming a p-n heterojunction with $MoSe_2$ using a simple ultrasonic method [207]. The results showed that the photocatalytic activity of the 1.5%-$MoSe_2$/Bi_2WO_6 catalyst was six times and seven times higher, respectively, than that of pure Bi_2WO_6 and pure $MoSe_2$. This result was due to the lower band gap in $MoSe_2$, and the composite material exhibited a significant red shift, which was beneficial for the catalytic performance of both materials. In addition, under the action of the internal electric field, the strong interlayer interaction of $MoSe_2$/Bi_2WO_6 promoted the separation of holes and electrons. That is, the holes moved to the $MoSe_2$ interface, and the electrons moved to Bi_2WO_6, effectively extending the lifetime of light-induced carriers. The results showed that as surface carriers accumulated, more ROS was generated, and the catalytic performance of the system was significantly improved.

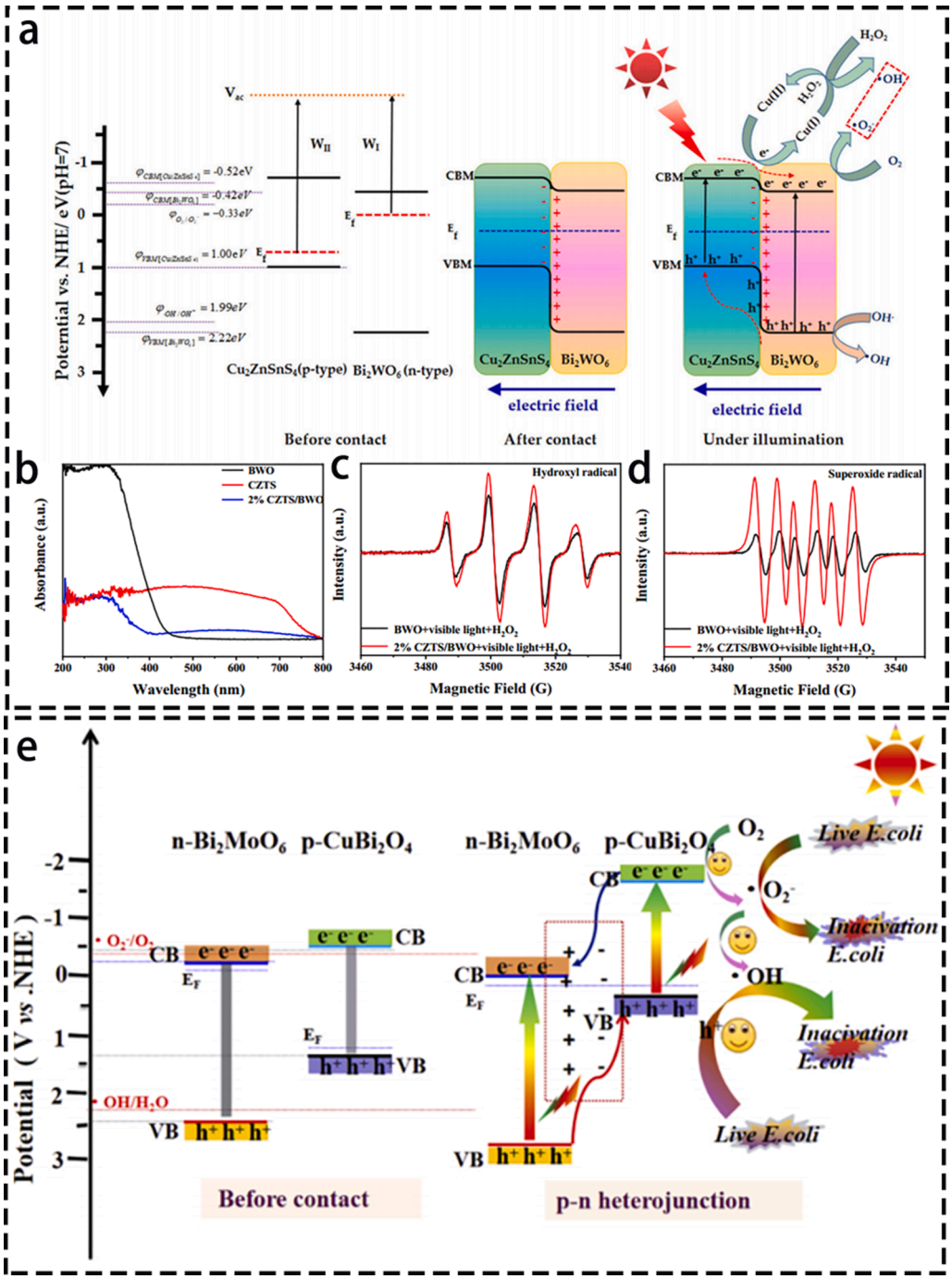

Fig. 23. (a) Proposed photocatalytic and photo-Fenton catalytic mechanisms by the 2D/2D CZTS/BWO type-II p-n heterojunction. (b) UV–Vis diffuse reflectance spectra of BWO, CZTS, and the 2% CZTS/BWO heterojunction.DMPO spin-trapping ESR spectra of the catalysts for (c) DMPO-·OH and (d) DMPO-·O_2^- [204]. Adapted with permission. Copyright 2020, Elsevier B.V. (e) Mechanism of photocacalytic disinfection towards *E. coli* of $CuBi_2O_4/Bi_2MoO_6$ p-n heterojunction [209]. Adapted with permission. Copyright 2019, Elsevier B.V.

Another $CuBi_2O_4/Bi_2MoO_6$ p-n heterojunction also confirmed improvement in the catalytic performance of the system, thus endowing 2DNMs with high photocatalytic bacteria-eliminating efficiency under visible light excitation (Fig. 23**e**) [209].

3.3.6.2.3. Z-scheme heterojunction. Both heterojunctions, type II and p-n, have obvious defects. Both electrons and holes are concentrated at the lower energy level of semiconductors, thus reducing the redox performance of the materials. As a result, a new type of heterojunction, the Z-type heterojunction, gradually developed. The Z-scheme was developed over three generations (Fig. 24) in 1979, 2006, and 2013, respectively: 1) a traditional Z-scheme with a space shuttle redox media; 2) an all-solid-state Z-scheme with

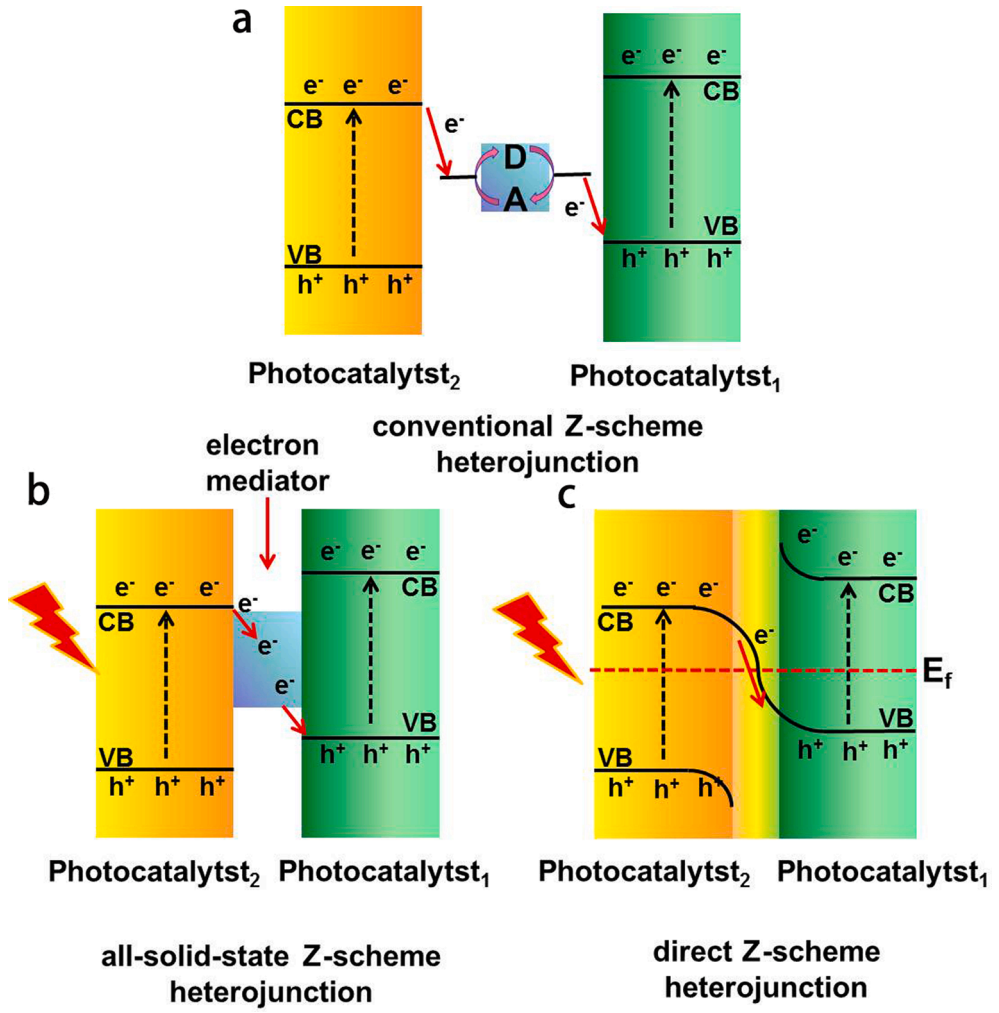

Fig. 24. The schematic diagram of three type Z-scheme heterojunction: (a) traditional Z-scheme (b) all-solid-state Z-scheme (c) direct Z-scheme.

electronic media; and 3) a direct Z-scheme [218–220].

Fig. 24**a** shows a traditional Z-scheme. The system consists of photocatalyst$_1$ and photocatalyst$_2$ (without physical contact) and a liquid-phase electron acceptor/donor (A/D) pair. When two kinds of semiconductors are exposed to light radiation, the excited electrons in the CB of the photocatalyst$_2$ reduce A to produce D, and the holes of the photocatalyst$_1$ oxidize D to produce A. Using the redox conversion of the A/D medium, the electrons in photocatalyst$_2$ and the holes in photocatalyst$_1$ are indirectly combined, and the holes and electrons in the two are retained, respectively, which indirectly realizes the separation of light-excited carriers. The retained electrons and holes are in higher potential CB and VB, which provides the system with a higher redox capacity, thereby greatly promoting photocatalytic reduction and oxidation reactions. However, redox media (A / D), such as IO^{3-}/I^{-}, Fe^{3+}/Fe^{2+} and I^{3-}/I^{-}, exist only in the liquid phase, which hinders their development in the gas–solid two-phase [221].

Fig. 24**b** shows an all-solid-state Z-scheme system, which is composed of two semiconductors (photocatalyst$_1$ and photocatalyst$_2$) and a solid electronic medium in close contact with the two semiconductors. Solid electronic media, such as precious metal NPs and carbon-based materials, are generally excellent conductors of electrons [222]. Similar to the traditional Z-scheme, after excitation by light irradiation, using an electronic medium with good electron transport properties, the electrons in the CB of the photocatalyst$_2$ are directly combined with the holes in the VB of photocatalyst$_1$. Finally, highly oxidative holes and strongly reductive electrons are left in photocatalyst$_2$ and photocatalyst$_1$, respectively.

For example, through a simple calcination strategy, Feng et al. used carbon quantum dots (CQD) as the electronic medium between CdS and g-C_3N_4 to synthesize a Z-scheme heterojunction with a visible NIR light response [223]. The CQDs showed excellent up-conversion performance, in which NIR light was converted to visible light and an NIR light response was realized. In addition, as an electronic medium, CB electrons in CdS quickly migrated to the CQDs and then interacted with the holes in g-C_3N_4, which led to the separation of carriers in the composite material. The remaining electrons in g-C_3N_4 CB reacted with O_2 to generate $\bullet O_2^-$ and combined with the holes accumulated in CdS to cause a redox reaction. In addition to CQDs, a recent study showed that rGO could also be used as

an electron transfer medium between two semiconductors: TiO_2 and WO_3. A simple hydrolysis-hydrothermal method was employed to prepare the Z-scheme heterojunction of TiO_2/rGO/WO_3, and rGO was used to combine the other two phases. (Fig. 25**a, b**) [212]. Compared with TiO_2/WO_3 nanocomposites, TiO_2/rGO/WO_3 had a Z-type heterojunction structure because rGO acted as an electron transport medium, which improved the optoelectronic properties and photocatalytic activity of the system, which then exhibited enhanced bacterial inactivation activity under simulated sunlight (Fig. 25**c**). In particular, the photoexcited electrons in the CB of WO_3 migrated to the VB of TiO_2, while the respective electrons and holes were stored and aggregated. Finally, the electrons on the CB of TiO_2 oxidized oxygen to produce $\bullet O_2^-$ and H_2O_2. The holes accumulated in WO_3 reduced H_2O to generate •OH. These active substances effectively inactivated *E. coli*, achieving a sterilization efficiency of 97.3% within 80 min under visible light irradiation.

The third type of direct Z-heterojunction is shown in Fig. 24**c**. Compared with photocatalyst$_2$, the CB and VB of photocatalyst$_1$ have higher potential energy with a smaller work function (i.e., a higher Fermi level). When the two are in contact, the free electrons on the CB of photocatalyst$_2$ are transferred to the VB of photocatalyst$_1$ until the Fermi level is balanced. Therefore, the light-excited electrons in photocatalyst$_1$ and the holes in photocatalyst$_2$ are preserved and separated, and their original strong redox ability is maintained, so they exhibit higher photocatalytic efficiency [224].

Wu et al. constructed a Z-scheme composed of two 2D materials, O-doped carbon oxynitride (OCN) and ultrathin coal double hydroxide (CoAl-LDH), which were tightly combined by hydrogen bonding [225]. After visible light irradiation, both OCN and CoAl-LDH generated charge carriers. At the heterojunction interface, the electrons of OCN and the holes of CoAl-LDH were rapidly combined, and the holes and electrons on each were retained separately to avoid recombination. The light-induced electrons accumulating in the CB of CoAl-LDH oxidized O_2 to form $\bullet O_2^-$. The VB of the OCN transferred more positively charged holes to reduce H_2O to generate •OH. Consequently, the hybrid exhibited enhanced photocatalytic performance compared with the single component. Hu et al. designed and synthesized a simple and effective 2D/2D BP/monolayer Bi_2WO_6 (MBWO) nanosheet Z-type heterojunction (Fig. 26**a**) [214]. The catalytic performance of the BP/MBWO heterojunction was greatly enhanced compared with that of each individual component (Fig. 26**b**), which was caused by the effective separation and transfer of carriers by the Z-scheme and the wide absorption spectrum (i.e., from ultraviolet to NIR) of BP. The electrons in the CB of MBWO combined with the holes on the BP, and the accumulated electrons on the VB of BP reduced O_2 to $\bullet O_2^-$, which enhanced the photocatalytic performance of the hybrid heterojunction. In another study, Wu et al. used MnO_2 and g-C_3N_4 to construct a direct Z-scheme on the surface of a Ti implant [226]. After excitation by visible light radiation, MnO_2 and g-C_3N_4 generated carriers. Because of the influence of the heterojunction interface, the excited electrons in MnO_2 were directly combined with the holes in g-C_3N_4, which indirectly avoided the recombination of the single component carrier. In the final performance, the light conversion efficiency of the system was 21.11% higher than that of pure g-C_3N_4. On the surface of the heterostructure, O_2 reacted with the photogenerated electrons of g-C_3N_4 to generate $\bullet O_2^-$ and $^1O_2$, and H_2O reacted with the holes of MnO_2 to generate •OH, which denatured the protein and DNA and effectively eliminated both *S. aureus* and *E. coli*.

3.3.6.2.4. S-scheme heterostructure. The S-type heterojunction is composed of two n-type semiconductors: an oxidation photocatalyst (OP) and a reduction photocatalyst (RP) (Fig. 27). Because the Fermi level of the former is lower than that of the latter, in the absence of radiation, electrons in the RP spontaneously flowed into the OP at the interface until the Fermi levels of the two reached equilibrium, thereby generating an internal electric field. When OP and RP are excited by light to generate a large number of carriers, the electrons in the CB of OP consume photogenerated holes in the VB of RP induced by the internal electric field. The reserved holes and electrons with strong redox ability accumulate in the two, playing an important role in subsequent catalytic applications.

Jia et al. fabricated an S-scheme composite BiOBr/$BiOAc_{1-x}Br_x$ using a simple co-precipitation method to prepare BiOBr and BiO$(CH_3COO)_{1-x}Br_x$ at room temperature [216]. In this S-scheme heterojunction, $BiOAc_{1-x}Br_x$ and BiOBr were used as RPs with a higher Fermi level and OPs with a lower Fermi level, respectively. When they were in close contact, the Fermi level tended to balance, causing

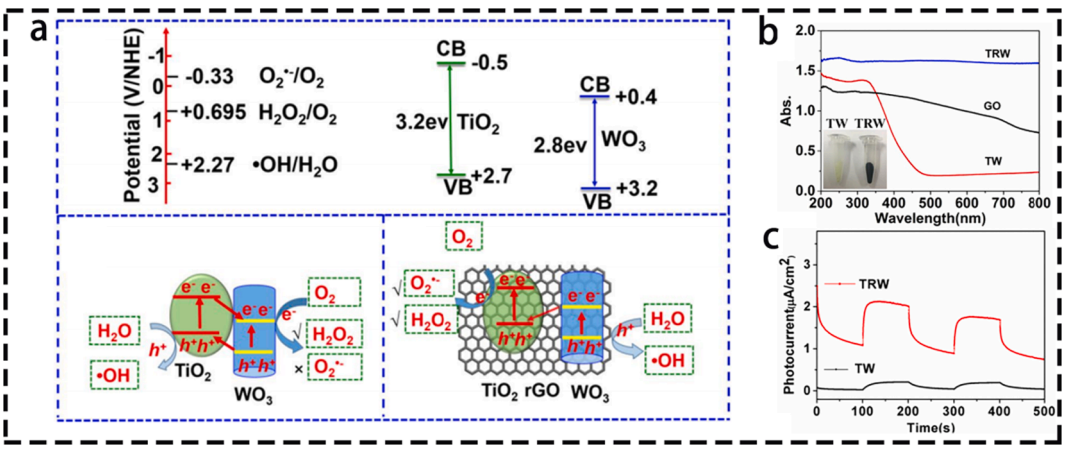

Fig. 25. (a) Schematic diagram for describing the conduction band and valence band of TiO_2 and WO_3; Heterojunction-type charge transfer and surface redox reactions for TiO_2/WO_3; Z-scheme charge transfer and surface redox reactions for TiO_2/rGO/WO_3. (b) UV–vis diffuse reflectance spectra of different samples. (c) Photocurrent response curve [212]. Adapted with permission. Copyright 2017, Elsevier B.V.

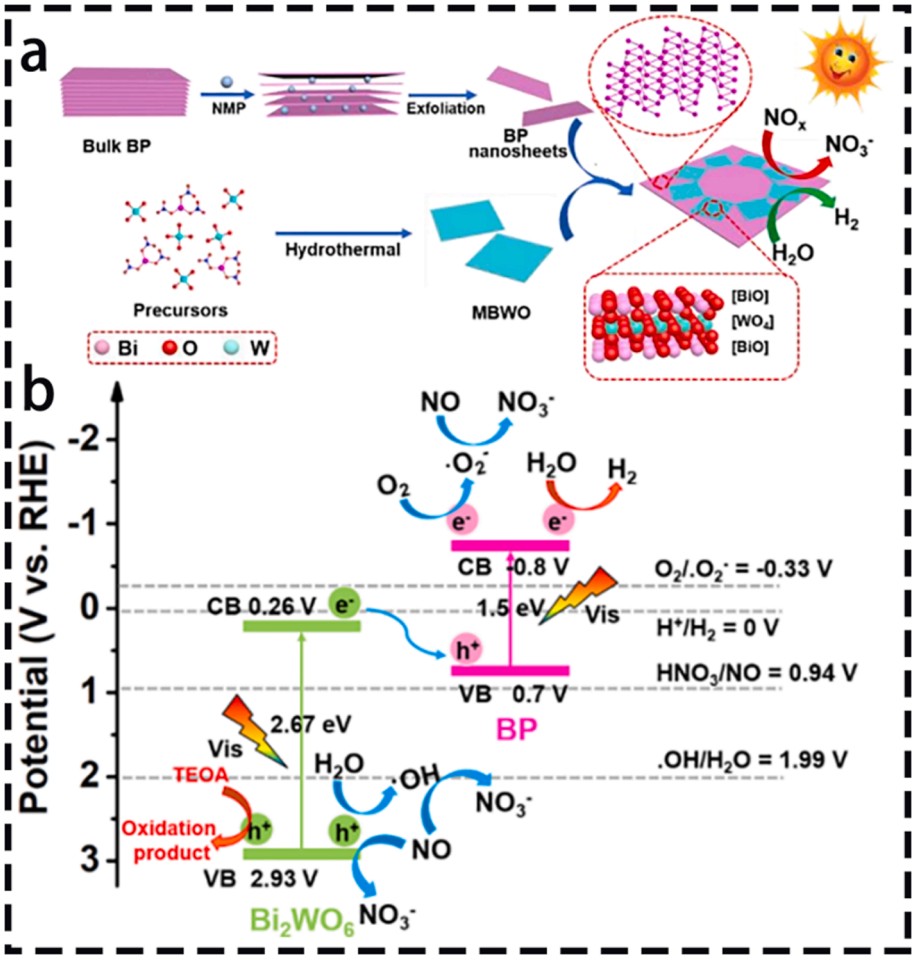

Fig. 26. (a) Schematic illustration of the fabrication of BP/MBWO heterojunction. (b) Photocatalytic mechanism of NO removal and water splitting by BP/MBWO heterojunction under visible-light irradiation (the various redox potentials versus RHE) [214]. Adapted with permission. Copyright 2018, Wiley-VCH.

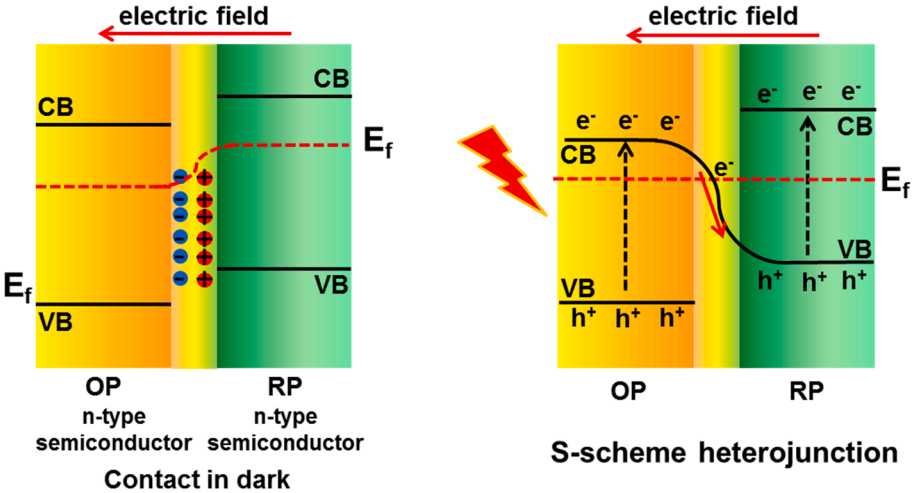

Fig. 27. The schematic diagram of S-scheme heterojunction before the contact and after contacr between two n-type semiconductors.

the charge in the interface of $BiOAc_{1-x}Br_x$ to spontaneously transfer to BiOBr, which also led to the formation of an internal electric field. In a subsequent excitation by light radiation, because of the electric field, the excited electrons in the CB of BiOBr were transferred to the VB of $BiOAc_{1-x}Br_x$ to combine with "useless" holes, and a large number of "useful" holes and electrons were accumulated and retained in BiOBr and $BiOAc_{1-x}Br_x$, respectively. The electrons and holes were combined with O_2 and H_2O to generate $\bullet O_2^-$ and •OH, respectively, thereby enhancing the photolysis performance of the hybrid product. In another study, Xia et al. used an *in situ* growth strategy to grow CeO_2 quantum dots on the surface of PCN nanosheets to obtain a new 0D/2D S-scheme heterojunction material (Fig. 28**a-c**) [227]. The Fermi level of PCN was higher than that of CeO_2. In this study, when the CeO_2 photocatalyst was in close contact with PCN, the Fermi energy level tended to reach the same level, and the electrons in PCN flowed to CeO_2 spontaneously. Then, under light irradiation, both PCN and CeO_2 generated excited carriers. Subsequently, driven by the internal electric field and the Coulomb interaction, electrons accumulated in the CB of CeO_2 tended to recombine with the holes in PCN VB, while the other excitonic holes and electrons accumulated in VB and CB, respectively, and interacted with the surrounding H_2O and O_2 molecules to produce •OH and $\bullet O_2^-$ (Fig. 28**d, e**). Finally, these active species effectively destroyed the cell walls of bacteria through advanced oxidation processes, inducing a highly effective antibacterial efficiency of 99.4% after 60 min of light irradiation.

3.4. Photothermal antibacterial of 2DNMs

High-temperature treatment is the most common method used to eliminate microorganisms. When the temperature exceeds 55 °C over a period of time, the physiological and biochemical reactions in non-heat-resistant bacteria are accelerated, and temperature-sensitive substances in the body, such as heat shock proteins, are irreversibly damaged as temperatures increase [228]. Photothermal therapy has been employed to treat cancer and bacterial diseases using the thermal effects of photothermal agents (PTA) under light irradiation [229]. As shown in Fig. 29, the main antibacterial mechanism of PTA is to increase the surrounding local temperature by converting light energy into thermal energy. High temperatures can denature bacterial proteins, alter gene expression, disrupt metabolism, and induce bacterial cell apoptosis. Based on the discovery of the photothermal properties of 2DNMs, many 2DNMs have been used as PTAs in antibacterial applications [230–232].

Many 2DNMs have photothermal conversion properties, such as MXene [233], GO [234], MoS_2 [235,236], and BP [237]. Chou et al. prepared MoS_2 using the chemical stripping method [235]. By measuring the photothermal curves of different concentrations of MoS_2, they determined that when a low concentration of MoS_2 was applied (38 ppm), the temperature quickly rose to above 40 °C after

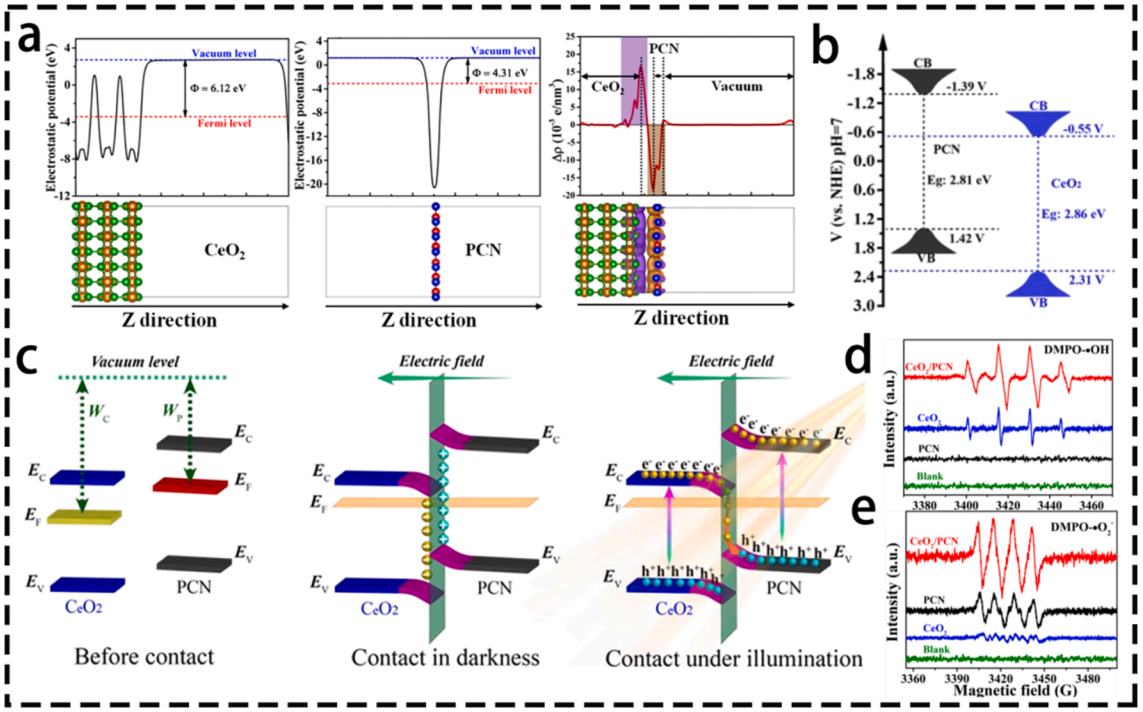

Fig. 28. (a) The calculated work function and corresponding structural model of (1 1 1) plane of CeO_2 and (0 0 1) plane of PCN. And the planar-averaged electron density difference Δρ and side view of the charge density difference over the CeO_2/PCN heterojunction. The orange and purple areas represent depletion and accumulation of electrons, respectively. (b) Band structure of pure CeO_2 and PCN. (c) The internal electric field with band edge bending near the interface of CeO_2/PCN. And the S-scheme transfer mechanism of photogenerated electrons under the illumination. EPR signals of (d) DMPO-•OH adducts in deionized water and (e) DMPO-$\bullet O_2^-$ adducts in methanol over various photocatalysts under illumination for 120 s [227]. Adapted with permission. Copyright 2019, Wiley-VCH. (For interpretation of the references to colour in this figure legend, the reader is referred to the web version of this article.)

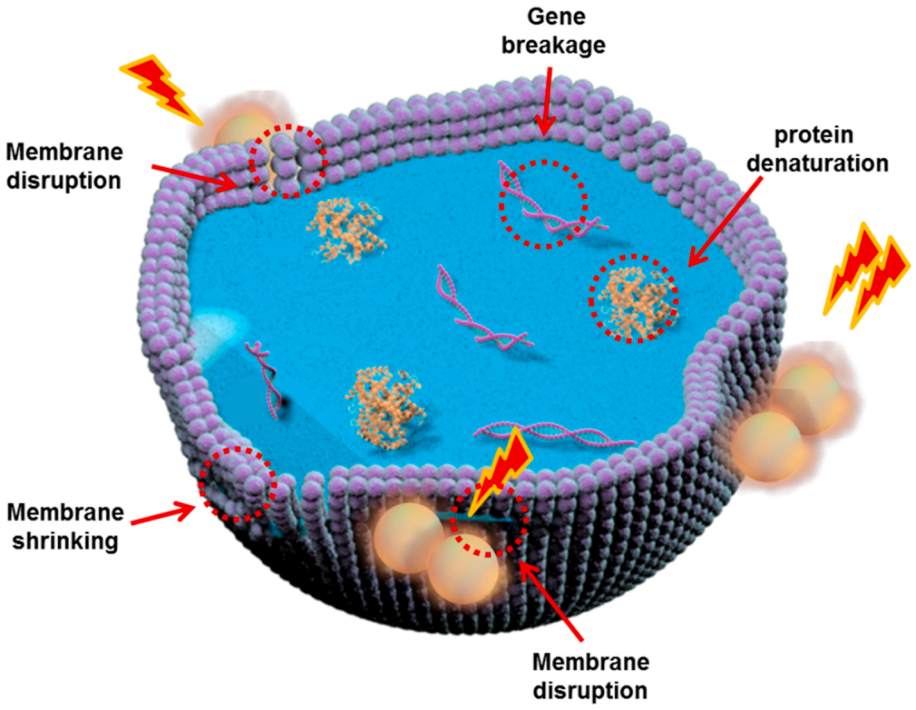

Fig. 29. The schematic diagram of photothermal of PTAs action on bacterial cell membrane.

light irradiation for 1 min (0.8 W cm^{-2}, 808 nm). Li et al. used chitosan hydrogels as carriers and BP nanosheets as PTAs to construct filtration membranes with sandwich structures [237]. Under irradiation of 808 nm light at a power density of 0.5 W cm^{-2}, the temperature of the film rose to 100 °C within 10 min.

To discuss the photothermal mechanism of 2DNMs, it is necessary to understand the principle of light absorption by materials. The unique feature of 2DNMs is their layered structure [238]. When 2D materials are irradiated by light, radiation waves are absorbed repeatedly between layers. The repeated refraction and absorption of light by the multilayer structure led to the obvious absorption of

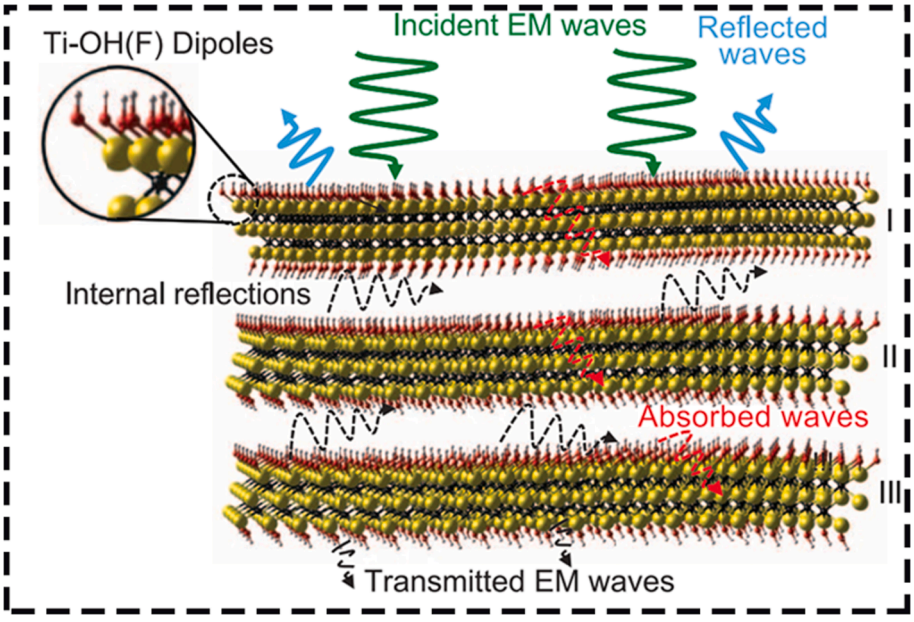

Fig. 30. Proposed electromagnetic waves shielding mechanism. Incoming electromagnetic waves (green arrows) strike the surface of an MXene flake [239]. Adapted with permission. Copyright 2020, American Association for the Advancement of Science. (For interpretation of the references to colour in this figure legend, the reader is referred to the web version of this article.)

light by 2DNMs, which is also the basis of its excellent photothermal performance. For example, a recent study showed that when electromagnetic waves hit the surface of 2D MXene nanosheets, some electromagnetic waves would be reflected [239]. The remaining electromagnetic waves passed through the MXene lattice structure and interacted with its high density of discrete electrons to generate an electrical current, resulting in ohmic losses and reduced electromagnetic wave energy (Fig. 30). The surviving electromagnetic waves encountered the next barrier layer after passing through the first layer, and the electromagnetic wave attenuation phenomenon was repeated. Moreover, layer II acted as a reflective surface, causing multiple internal reflections. Electromagnetic waves were reflected back and forth between layers until they were completely absorbed into the structure, which resulted in the phenomenon that the multilayer structure effectively absorbed electromagnetic waves.

The mechanism of the absorption spectrum of 2DNMs has understood, but the mechanism by which radiant light is consumed and converted into 2DNMs needs to be further explored. The common mechanisms of light conversion to thermal energy are shown in Fig. 31. 2DNMs generate hot electrons and holes upon light excitation, and the temperature of the initial carriers is higher than the lattice temperature [240]. The phonons are scattered by electrons and holes to achieve a thermal balance between the hot carriers and the crystal lattice. When excess heat energy is transferred to the phonons, it causes vibrations in the crystal lattice, which raises the local temperature. Defects of the surfaces of 2DNMs induce the formation of deep-level defects in the intermediate energy gap [241]. The photoexcited electrons recombine with the holes through the limited bridge deep-level defects to generate phonons. They then generate strong lattice vibrations that release heat to the surrounding medium. Zhang et al. developed a solar steam generator based on defect-rich graphene sheets [242]. Utilizing these abundant defects shortened the free path of long-wave phonons in graphene, thereby reducing overall thermal conductivity and presenting better optical and thermal performance. In another situation, in most photons, the energy emitted by the light source is higher than the excitation energy required for 2DNM. The excited carriers relax to the edge of the band gap, and the extra energy is converted into heat through the thermalization process [243]. When a 2DNM heterojunction is constructed, the band gap in each component changes, and more electron transfer paths are formed, which is beneficial for improving photothermal efficiency [244]. Some 2DNMs, such as the Bi-based materials, MoS_2 and MXene, have been shown to have unique LSPR effects. For example, Fan et al. found that MXenes and $Ti_3C_2T_x$ exhibited semimetallic properties with ultrahigh metal conductivity, which produced an LSPR effect similar to metal NPs [245], resulting in enhanced light absorption, rapid solar collection, and high heat conversion ability. Under visible light irradiation at a power density of 128.6 mW cm^{-2}, the temperature of PEG/$Ti_3C_2T_x$ composite increased sharply from 19 °C to > 55 °C.

3.5. Strategies for enhancing photothermal antibacterial therapy

Because of the larger bandgap width in 2DNMs, the light absorption range is narrow. As a result, photothermal conversion efficiency is limited, resulting in poor photothermal antibacterial performance. Therefore, it is necessary to improve the photothermal performance of 2DNMs by modification. Current modification methods include changing the size and thickness of 2DNMs and combining with other photothermal agents (PTAs).

3.5.1. Changing the structures

In addition to the previously described PDT, the PTT performance of 2DNMs varies according to changes in their structure [246–248]. 2DNMs have micron-scale and nanoscale structures. The micron-scale structure is modified by changing the morphology of

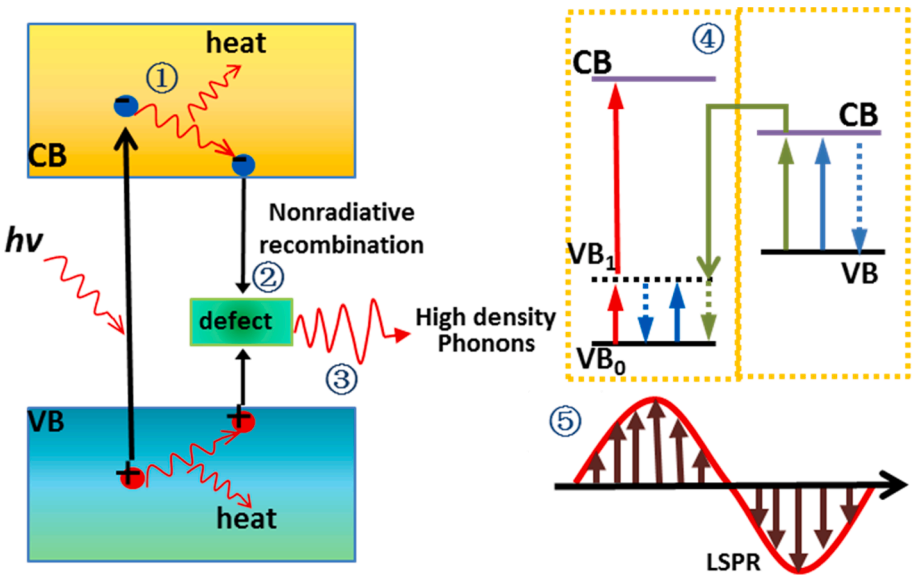

Fig. 31. The five photothermal production mechanism diagram of PTAs.

Table 5
Summary of the size-dependent PTT of 2DMs.

2DM	Irradiation wavelength	synthetic method	Size and thickness	Irradiation time	T (°C)	Antibacterial efficiency	Ref
NRGO	808 nm	Hummers method	thickness lower than 1 nm	10 min	60 °C	almost 100 % for *S. aureus*	249
titanium carbide	808 nm	intercalation, delamination	monolayer or bilayer	5 min	60 °C	–	250
MnB_2	808 nm	chemical etching	monolayer	5 min	60 °C	–	251
MoS_2	808 nm	*in situ* solvothermal	diameters of 25 nm	20 min	50 °C	97 % for Amp^r *E. coli* and 100 % for *B. Subtilis*	252
ce-MoS_2	Solar light	chemically exfoliated	monolayer	15 min	60 °C	–	253

the material, such as particle size tuning. The nanoscale structure is modified by doping or defect formation. Table 5 lists typical 2DNMs and their structure-dependent photothermal properties [249–253]. The micron-scale structure of 2DNMs is determined by the aspect ratio and the number and thickness of the nanosheets. In [249], a nanoscale rGO (NRGO) had a lateral size of less than 100 nm and a longitudinal thickness of less than 1 nm, which was used as an effective photothermal agent to eliminate pathogenic bacteria. In addition, NRGO was bound to the anti-*S. aureus* polyclonal antibody through its surface groups, so the composite could be used for specific recognition. Compared with large rGO, NRGO showed greater absorbance and better photothermal performance. When the system concentration was only 20 mg L^{-1}, the temperature reached 55 °C under 808 nm wavelength light (400 mW cm^{-2}) after irradiation for 10 min. Therefore, the antibody-NRGO complex selectively adsorbed and contacted S. *aureus* through antibodies, thus eliminating the bacteria through the photothermal effect.

In addition to the size of the nanosheets, the number of their layers was shown to affect photothermal performance. Xuan et al. reported a new method for preparing extremely thin delaminated titanium carbide (TC) sheets with strong NIR absorption (Fig. 32**a-c**)

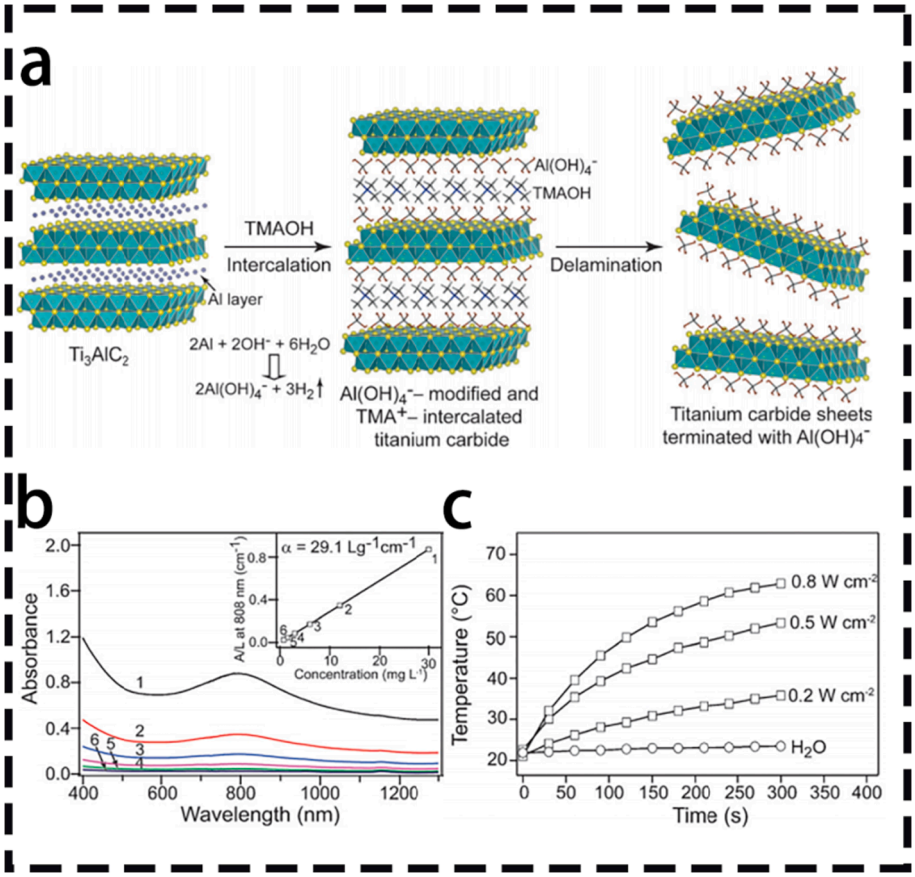

Fig. 32. (a) Schematic illustration showing the intercalation and delamination process. (b) NIR absorption spectra for the colloidal sheet suspensions. Inset: Beer law absorbance plot for absorption at 808 nm. (c) Photothermal heating curves of TC nanosheets at various power densities [250]. Adapted with permission. Copyright 2016, Wiley-VCH.

Table 6
Summary of the PTAs composite with 2DMs.

2DNM	PTAs	Irradiation wavelength	synthetic method	Irradiation time	photothermal conversion efficiency	PTT	Antibacterial efficiency	Ref
WS_2	carbon dots	1064 nm	hydrothermal	5 min	56.3 %	53 °C	–	259
MoS_2	carbon dots	808 nm	Hummers method	5 min	78.2 %	55 °C	–	260
BP	carbon dots	808 nm, 1064 nm	microwave, stirring	6 min	77.3%, 61.4%	55.5 °C, 53.7 °C	–	261
BP	Cu, RGD, PEG	808 nm	exfoliation conjugated	5 min	–	56 °C	–	262
g-C_3N_4	CuS PEG	808 nm	pyrolysis	20 min	59.64 %	46 °C	99% of both *S. aureus* and *E. coli*	263
MoS_2	CdS/ Au	660, 808 and 980 nm	chemical vapor deposition	–	–	–	–	264
rGO	CdSe/ZnS QDs	808 nm	Hummer, sedimented	5 min	–	67 °C	–	265
rGO	AuNS	808 nm	seed mediated growth	6 min	22.6 %	61 °C	97% for *S. aureus* and 98% for *E. coli*	266
GO	AuNP, QCMC	808 nm	Hummer method	2 min	–	88.2 °C	effective for *B. subtilis* and *E. coli*	267
BP	Au	808 nm	physical adsorption	20 min	36.1 %	50 °C	–	268
GO	Ag	808 nm	Hummer method	7 min	–	61.6 °C	95.6% and 95.9 %for MDR-1 and MDR-2 *E. coli*	269
BP	Ag	808 nm,	*in situ* growth strategy	5 min	–	55 °C	effective for MRSA	270
MnO_2	Ag, CS	808 nm	hydrothermal	20 min	30.79 %	55.4 °C	99 % and 99.25% for *S. aureus* and *E. coli*	271
BP, rGO	–	808 nm	sonication and annealing	5 min	57.79 %	51 °C	–	272

[250]. Compared with the traditional method, this method uses organic base tetramethylammonium hydroxide (TMAOH) as an etchant. It reacted with Al in TC and generated $Al(OH)_4^-$ as an interlayer to promote delamination. After irradiation by 808 nm light at a power density of 0.8 W cm^{-2} for 3 min, the temperature of the ultrathin monolayer TC at a concentration of 50 mg mL^{-1} was increased to 50 °C. TMD is also a commonly used 2D photothermal material. Because some 2DNMs are polycrystaline, the properties of the crystaline phases differ. Changing the thickness of the nanosheets also changes the crystal phase of the material and improves performance. For example, Ghim et al. focused on the different photothermal properties in the 1 T phase and 2H phase of MoS_2 [253]. By preparing chemically exfoliated MoS_2 (ce-MoS_2), its crystal phase was changed from the 2H phase (triangular prism coordination) to the 1 T phase (octahedral coordination). The results showed that compared with bulk MoS_2, ce-MoS_2 had a highly efficient photothermal effect, and its photothermal conversion efficiency was increased by about 19%.

In addition to changes in micron-scale structure, nanoscale structure changes also modify photothermal performance. This change is mainly achieved through doping and defect formation. Ito et al. developed a multifunctional nitrogen-doped porous graphene material [254]. Pore size and chemical doping determined the thermal conductivity of graphene samples to some extent. N-doping led to the formation of defects in the lattice structure of graphene, which then led to a decrease in the thermal conductivity and specific heat capacity of graphene.

3.5.2. *Combination with other photothermal materials*

In addition to changing the size, other PTAs have been utilized to strengthen the photothermal effects of 2DNMs by fabricating composites [255,256]. PTAs commonly used to enhance the photothermal performance of 2DNMs have good electrical conductivity or narrow band gaps. These PTAs conduct the electrons generated by 2DNM photoexcitation, which then disperse and generate more phonons. The phonons then transfer energy to the lattice and generate heat through lattice vibrations [257]. The incorporation of PTA also leads to a red shift in the absorption spectrum of the material, increasing the light absorption intensity and photothermal conversion efficiency. In addition, the LSPR effect of PTA is beneficial for improving photothermal performance [258]. Table 6 [259–272] summarizes recent advances in this field.

For example, carbon dots (CD) are PTA. The positively charged N-doped CDs synthesized by the microwave-assisted hydrothermal method have been shown to have an absorption spectrum ranging into the NIR-II region. Geng et al. assembled CDs on the surface of

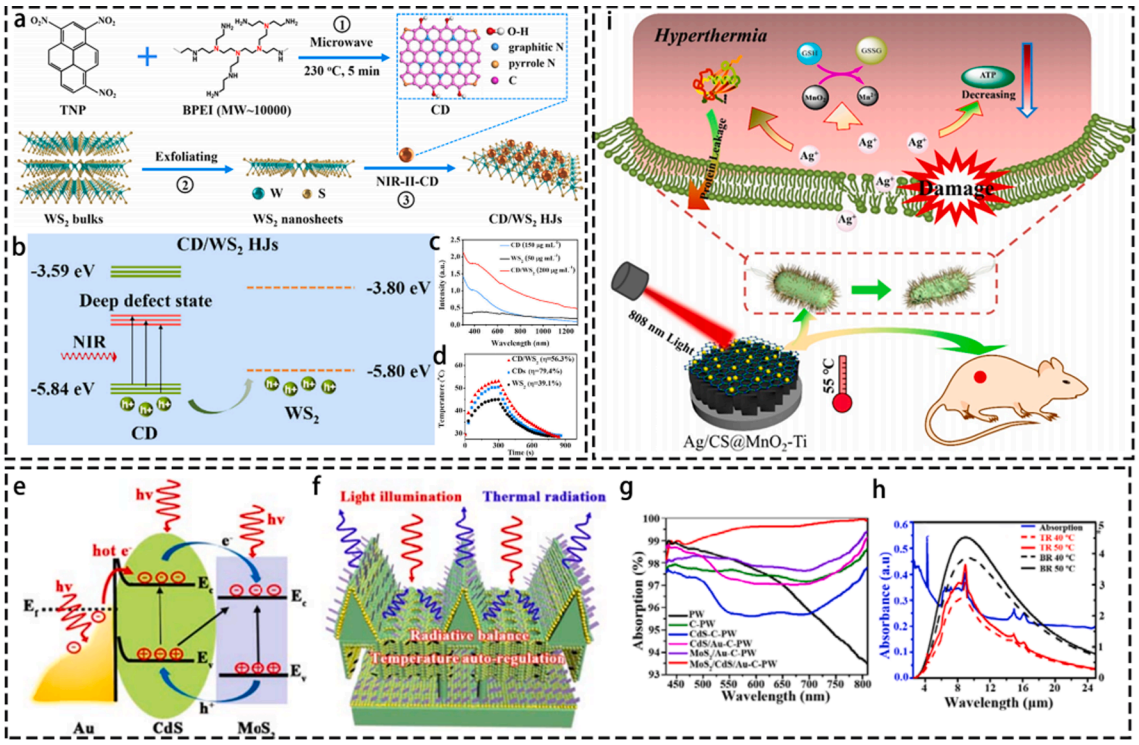

Fig. 33. (a) Preparation procedure of CD/WS_2 HJs including three steps. (b) Schematic illustration of the energy position and the deep defect state formation under NIR laser irradiation. UV–vis-NIR absorption spectra (c) and the photothermal effect (d) of CDs, WS_2, and CD/WS_2 HJs under 1064 nm laser irradiation (0.6 W cm^{-2}) [259]. Adapted with permission. Copyright 2019, Elsevier B.V. (e) Schenatic illustration of the photoelectric response mechanism and (f) the omnidirectional absorption and radiative balance characteristic of the MoS_2/CdS/Au_C_PW photodetector. (g) The absorption spectra of the different samples over the wavelength range of 400–810 nm. (h) Absorption and thermal radiation spectra of MoS_2/CdS/Au_C_PW [264]. Adapted with permission. Copyright 2020, Royal Society of Chemistry. (i) Schematic Drawing Exhibiting the Synergistic Behaviors in the Bacteria-Killing Processes of Ag/CS@MnO_2-Ti through Prereleased Low-Concerntration Ag^+ and Photothermal Effects of MnO_2 in the Coating under NIR Irradiation [271]. Adapted with permission. Copyright 2019, American Chemical Society.

negatively charged WS_2 nanosheets by electrostatic force, so the CDs/WS_2 mixture had higher light absorption efficiency under NIR-II light irradiation (Fig. 33**a, b**) [259]. Under irradiation, the excited electrons in the VB of CDs were trapped by the N-doping induced defects, and the holes were rapidly transferred to the WS_2. As a result, a large number of free carriers accumulated in WS_2, which caused the LSPR effect to enhance absorption in the NIRII region (Fig. 33**c, d**). Therefore, under irradiation by a laser with a power density of 0.6 W cm^{-2} and a wavelength of 1,064 nm for 5 min, the temperature of CD/WS_2 rapidly increased from 28.5 °C to 53.0 °C, and the photothermal conversion efficiency reached 56.3%. The CuS NPs also showed excellent photothermal effects through the LSPR effect under light irradiation. The CuS NPs and g-C_3N_4 were combined through a simple hydrothermal strategy, which showed uniform dispersion without agglomeration. The composite was subsequently encapsulated by PEG [263]. The hybrid had a strong NIR absorption capacity, 59.64% light-to-heat conversion efficiency, and an elimination efficiency of up to 99% against *S. aureus* and *E. coli* under NIR irradiation for 20 min. Tian et al. designed a MoS_2/CdS/Au composite material with excellent photothermal properties under full-spectrum light irradiation (Fig. 33**e-h**) [264]. The LSPR effect of Au NPs and layered MoS_2 promoted light absorption and enhanced the exciton transition capability of CdS NPs. Furthermore, due to the LSPR, the excition of Au NPs decayed nonradiatively into hot carriers. The hot electrons were transferred to the CB of the CdS NPs. However, because of the low CB edge in MoS_2, the photoexcited electrons of CdS NPs were transferred to the MoS_2. The tight interfacial contact between CdS, Au, and MoS_2 led to the narrowing of the energy band, enabling a wider range of light absorption. Finally, the remaining photoelectrons were relaxed through collisions between electrons or phonons. This process generated heat energy. In addition to Au NPs, another common noble metal, Ag, is also used to improve the photothermal performance of 2DNMs. Wang et al. prepared an Ag/CS@MnO_2 composite using a simple hydrothermal method [271]. Because of the LSPR effect of Ag, the photothermal performance of the system exhibited a significant enhancement compared with that of MnO_2 alone (Fig. 33**i**). After irradiation with 808 nm NIR light for 20 min, in response to the high-temperature treatment, the antibacterial effects of AgNPs/MnO_2 nanosheets were modified by chitosan (CS) against *S. aureus* and *E. coli,* reaching 99.00% and 99.25%, respectively. Local hyperthermia produced after irradiation increased the permeability of the membranes of these bacteria, increasing their sensitivity to small amounts of the released Ag^+, which eventually damaged the bacterial membranes, caused protein leakage, and decreased ATP levels. In an acidic environment, MnO_2 nanosheets reacted with GSH at membrane rupture sites, MnO_2 was degraded to Mn^{2+}, and GSH was oxidized to glutathione disulfide (GSSG). The rate of this process was accelerated by hyperthermia. The oxidation of GSH in bacteria caused disturbances in the internal balance of bacteria, thus accelerating bacterial death.

3.6. Synergy of photothermal and photodynamic therapy

Although PDT has exhibited unique advantages for eliminating bacteria [273,274] (i.e., inhibition of bacteria resistance formation, high controllability, and low invasiveness), ROS has a short life span (less than40 ns) and a small action radius (about 10 nm) [275]. Only a small amount of ROS interacts with bacteria, and bacterial membranes effectively block foreign substances, resulting in poor antibacterial effects [276]. PTT increases local temperature, thereby damaging bacteria. However, the use of PTT alone has the following limitations: 1) long-term exposure to a high-power density laser may damage healthy tissues; and 2) the temperature of photothermal treatment is generally from 45 to 50 °C [277]. Some heat-resistant bacteria are difficult to eliminate because they remain active at temperatures as high as 60 °C [278,279]. Recent studies have revealed that a combination of PDT and PTT achieves better antibacterial therapeutic effects than PDT or PTT alone (Table 7) [280–287].

For instance, Li et al. combined Zn^{2+}-doped flake g-C_3N_4 with GO through electrostatic bonding and π-π stacking interaction to prepare g-C_3N_4-Zn^{2+}@oxide graphene (SCN-Zn^{2+}@GO) hybrid nanosheets) (Fig. 34**a**) [281]. Under short-term (10 min) dual light of 660 nm and 808 nm irradiation, because of the synergy between the PDT and PTT, the membranes of *E. coli* and *S. aureus* were distorted or ruptured, and the cytoplasm overflowed. The generation of localized high temperatures altered the permeability of bacterial

Table 7
Summary of the combination of PDT and PTT in 2DMs.

2DM	composite	Light source	synthetic method	time	PTT	PDT	Antibacterial efficiency	Ref
GO	AIEgen	daylight, 795 nm	stirring	1 h, 5 min	50 °C	ROS	Over 99 % for *S. aureus* and *E. coli*	280
g-C_3N_4 GO	Zn^{2+}	660, 808 nm	electrostatic bonding and π π stacking interactions	10 min	58 °C	•O_2^-, H_2O_2	Over 99.1% for *S. aureus* and *E. coli*	281
g-C_3N_4	ZnO, C Dots	visible light	thermal-polymerization	15 min	51.3 °C	•O_2^-, •OH	99.97 % and 99.99 % for *S. aureus* and *E. coli*	282
MoO_{3-x}	Ag	808 nm	sonication, hydrothermal	10 min	55 °C	h^+, •O_2^-, •OH	99.2% of *E. coli* and 97.0% of *S. aureus*	283
MoS_2	PDA, RGD	808 nm	hydrothermal	6 min	56.4 °C	$^1O_2$	Over 92.6% for *S. aureus* and *E. coli*	284
MoS_2	CS	660, 808 nm	electrophoretic deposition	10 min	50 °C	$^1O_2$	99.84% and 99.65% against *E. coli* and *S. aureus*	285
WS_2	Ag_2S	808 nm	exfoliated	20 min	55 °C	ROS	99.93% and 99.84% for *S. aureus* and *E. coli*	286
Bi_2WO_6	AuNRs	808 nm	hydrothermal	15 min	55.2 °C	ROS	99.96% and 99.62% against *E. coli* and *S. aureus*	287

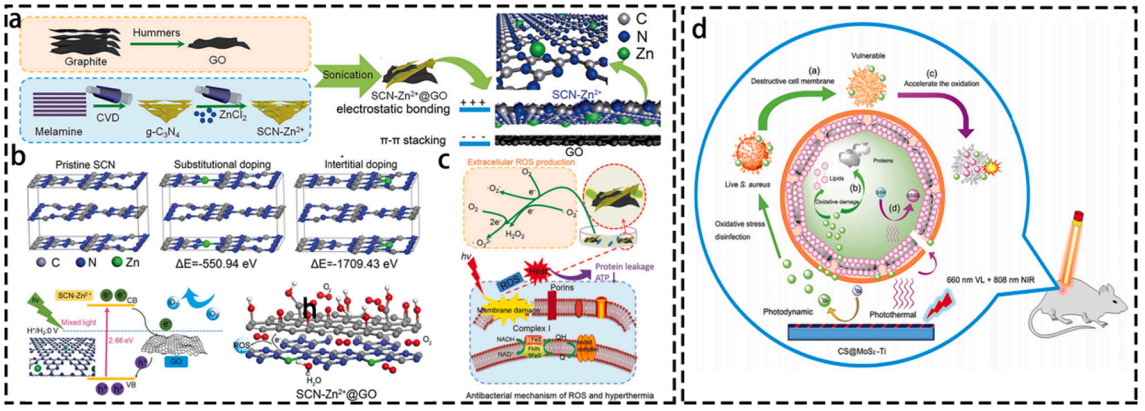

Fig. 34. (a) Preparation procedures of SCN-Zn^{2+}@GO with the atomic structure shown on the right. (b) Pristine SCN structure and possible binding modes of Zn and N atoms in SCN-Zn^{2+}@GO. From left to right are undoping and two kinds of Zn^{2+} doping (intertitial and substitutional doping) structure, respectively. The ΔE means the energy difference between undoped and doping structures. (c) Antibacterial mechanism of SCN-Zn^{2+}@GO20% under mixed light irradiation of ROS and hyperthermia [281]. Adapted with permission. Copyright 2018, Wiley-VCH. (d) Disinfection schematic *in vivo*, disruptive behavior on bacterial cell membrane, and inactivating bacteria through photodynamic and photothermal actions of CS@MoS_2 hybrid coating on Ti implant under the dual lights (660 nm VL + 808 nm NIR) [285]. Adapted with permission. Copyright 2018, Wiley-VCH.

membranes, reduced bacterial protein activity, and inhibited ATP synthesis. Photocatalytically generated ROS oxidized intracellular proteins through the bacterial cell wall and disrupted bacterial homeostasis. Furthermore, the electron transport of complex I, which binds NADH, FMN, and a tetranuclear FeS cluster, on the membrane respiratory chain was disrupted. The doping of Zn^{2+} increased defects in the SCN. Because both GO and Zn^{2+} easily captured electrons, they facilitated the separation of the photogenerated electron-

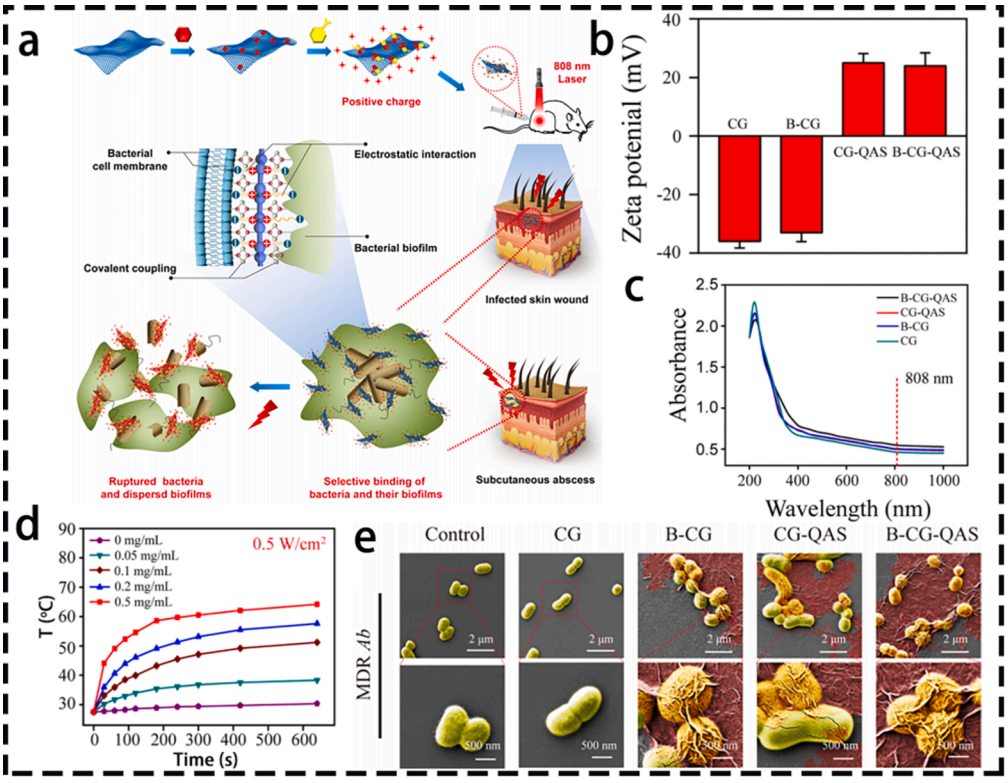

Fig. 35. (a) Schematic illustration of the antimicrobial mechanism of B-CG-QAS. (b) Zeta potentials of CG, B-CG, CG-QAS and B-CG-QAS. (c) UV–Vis-NIR spectra of CG, B-CG, CG-QAS and B-CG-QAS. (d)Temperature evolution curves of B-CG-QAS with different concentrations (0.05–0.5 $mg{\cdot}mL^{-1}$) under 808 nm NIR irradiation at 0.5 $W{\cdot}cm^{-2}$ (e) Representative SEM images of MDR *Ab* after incubation with PBS, CG, B-CG, CG-QAS and B-CG-QAS [294]. Adapted with permission. Copyright 2020, Elsevier B.V.

hole pairs (Fig. 34**b**). Zn^{2+} also increased light absorption and produced more carriers, which was conducive to the production of ROS that destroyed the cell membranes of bacteria, denatured proteins, and inhibited the metabolic pathways of bacteria (Fig. 34**c**). Yin et al. used MoO_{3-x} nanosheets to load Ag nanotubes and designed an efficient NIR light-driven hybrid antimicrobial agent [283]. Excited by NIR light, carriers that were effectively separated at the MoO_{3-x}-Ag interface reacted with O_2 and H_2O to generate active substances ($\bullet O_2^-$, and $\bullet OH$), which oxidized and destroyed the outer membranes of bacteria. In addition, MoO_{3-x}-Ag showed obvious NIR light absorption and efficient photothermal conversion ability. Hence, temperatures could reach 51.5 °C, and the generated hyperthermia could effectively inhibit bacterial activity. Finally, compared with bare MoO_{3-x} and Ag, under the synergistic effect of PDT and PTT, the system showed good bactericidal effects at a lower Ag content. Moreover, heat promoted the release of Ag^+, and metal ions had an inhibitory effect on bacterial activity. The antibacterial results showed that the antibacterial efficiency of the system against *E. coli* and *S. aureus* was as high as 99.2% and 97.0%, respectively, after 10 min of light stimulation. Feng et al. modified MoS_2 with CS to obtain a CS@MoS_2 hybrid coating, which had both photodynamic and photothermal properties for antibacterial applications (Fig. 34**d**) [285]. The results showed that, compared with a single light source, after irradiating with 660 nm and 808 nm light for 10 min, the antibacterial effects of the coating on *E. coli* and *S. aureus* reached 99.84% and 99.65%, respectively. In the underlying mechanism involving the 660 and 808 nm light sources, the former induced the system to produce singlet oxygen $^1O_2$ under 660 nm, while the latter caused the temperature to rise from 27.8 °C to 51.5 °C under 808 nm light irradiation. The cooperation of PDT and PTT led the system to have good antibacterial applications.

4. Synergistic antimicrobial activity

4.1. Functionalized targeting synergy

Targeted therapy has continued to be a research hotspot in the field of antibacterials because of its accurate bacterial-killing, high selectivity, and low toxicity effects on normal tissue [288,289]. Therefore, the establishment of a multi-modal targeting and treatment platform is a promising strategy for the treatment of bacterial infections [290,291].

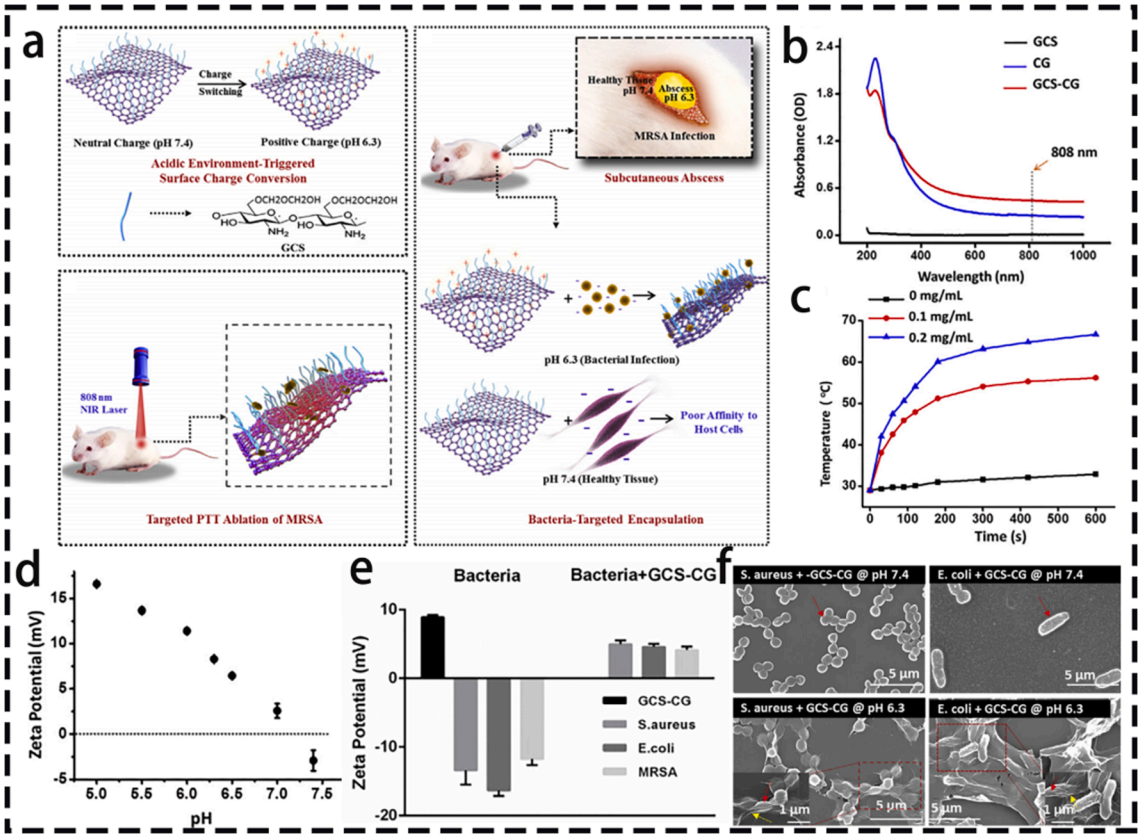

Fig. 36. (a) Schematic illustration of the antibacterial mechanism of GCS-CG. (b) Optical absorbance spectra of GCS, CG and GCS-CG at pH 6.3. (c) Photothermal conversion characterizations of GCS-CG aqueous solution with various concentrations under 0.75 W cm^2 808 nm laser irradiation for a certain time. (d) The GCS-CG surface-charge changes under different environmental pH. (e) Zeta potentials of bacteria before and after incubation with GCS-CG at pH 6.3. (f) Representative SEM micrographs of bacteria (pH 6.3 & 7.4) before and after incubation with GCS-CG [295]. Adapted with permission. Copyright 2018, Elsevier B.V.

For example, the heptadecylic end group of 1,2-distearoyl-*sn*-glycerol-3-phosphoethanolamino-[amino(polyethylene glycol-NH_2)] was utilized to hydrophobically interact with GO to obtain GO-PEG-NH_2 [292]. GO-PEG-NH_2 is a multifunctional antibacterial system with selective recognition, bacterial capture, and photothermal properties. Because the cell wall of bacteria was composed of peptidoglycan and acidic polysaccharides, the surface of the cell membrane was negatively charged. However, the cell membranes of normal tissue were almost neutral. Therefore, the amino functional group of GO-PEG-NH_2 was bound by electrostatic adsorption with negatively charged bacterial membranes. The presence of PEG chains also reduced the nonspecific adsorption of cell-surface proteins. Moreover, by utilizing the photothermal properties of GO, the system rapidly generated high local temperatures under NIR light irradiation to inactivate bacteria [293]. In another study, boric acid (BA), carboxylated graphene (CG), and quaternary ammonium salt (QAS) were combined to develop a dual-targeted antibacterial platform (B-CG-QAS) (Fig. 35**a**) [294]. On one hand, both bacteria and their biofilms had negative surface charges due to high levels of anionic phospholipids on their cell walls and negatively charged groups on polysaccharides and proteins in bacterial biofilm extracellular polymers (EPS). On the other hand, the cell walls and biofilm matrices of gram-negative bacteria were rich in polysaccharides, which covalently bound to BA to form cyclic boronated esters. Therefore, the positively charged B-CG-QAS reacted with the bacterial cell surface through electrostatic and hydrophobic interactions, thereby changing the molecular structure of the cell membrane surface and increasing the permeability of the cell membrane, which ultimately led to cytoplasmic diffusion and cell lysis (Fig. 35**b**). Furthermore, QAS damaged bacterial cell membranes, leading to the leakage of intracellular components and increasing the permeability and sensitivity of bacterial cells to heat. Finally, the platform exhibited a good photothermal effect under NIR light irradiation, and the system temperature rose to 51.2 °C after 10 min of irradiation (Fig. 35**c, d**). The induced high-temperature irreversibly inhibited bacterial intracellular responses and disrupted bacterial structures (Fig. 35**e**).

Inspired by the phenomenon that the pH values of bacterial microenvironments and normal tissue differed slightly, Qian et al. designed a pH-triggered system of ethylene glycol chitosan (GCS)-conjugated carboxygraphene (CG) (GCS-CG) (Fig. 36**a-c**) [295]. The system had the obvious ability to distinguish and target subtle changes in the pH value of the microenvironment, thus achieving bacteria targeting (pH = 6.3), and concentrated aggregation without damaging the surrounding healthy tissues (pH = 7.4) (Fig. 36**d, e**). After modification of the GCS, the absorption intensity of the system in the NIR range increased. Under the influence of the pH of the lesion, the surface charge in the system gradually changed from negative to positive. GCS-CG interacted strongly with the negatively charged bacterial surfaces, whereas healthy tissue was not targeted. In addition, after irradiation by NIR light, the local temperature of GCS-CG increased from 29 °C to 55 °C, and the antibacterial efficiency of the infected site was as high as 100% after photothermal treatment (Fig. 36**f**). In addition, specific secreted proteins on the surface of bacteria are used in targeted research field. For example, Liu et al. proposed an enzyme-responsive nanosystem using hyaluronic acid (HA) to encapsulate MoS_2 and ruthenium (Ru) loaded with ascorbic acid (AA). Bacterial infections were treated by using the synergistic chemical and photothermal effects of AA@Ru@HA-MoS_2 [296]. Ciprofloxacin-coated MoS_2 NPs with peroxide-like activity targeted bacteria and accumulated effectively in the infected area. Hyaluronidase secreted by the bacteria decomposed the encapsulant HA. When the NPs moved to the infected site, HA was broken down and AA was released. MoS_2 adsorbed on bacterial cells directly catalyzed AA to produce •OH, while mesoporous Ru NPs provided an NIR-responsive photothermal effect. As a result, it was able to target and eliminate the infection of *S. aureus* and *P. aeruginosa* under the synergistic effects of PTT and PDT, and the antibacterial rates were 89.2% and 81.9%, respectively.

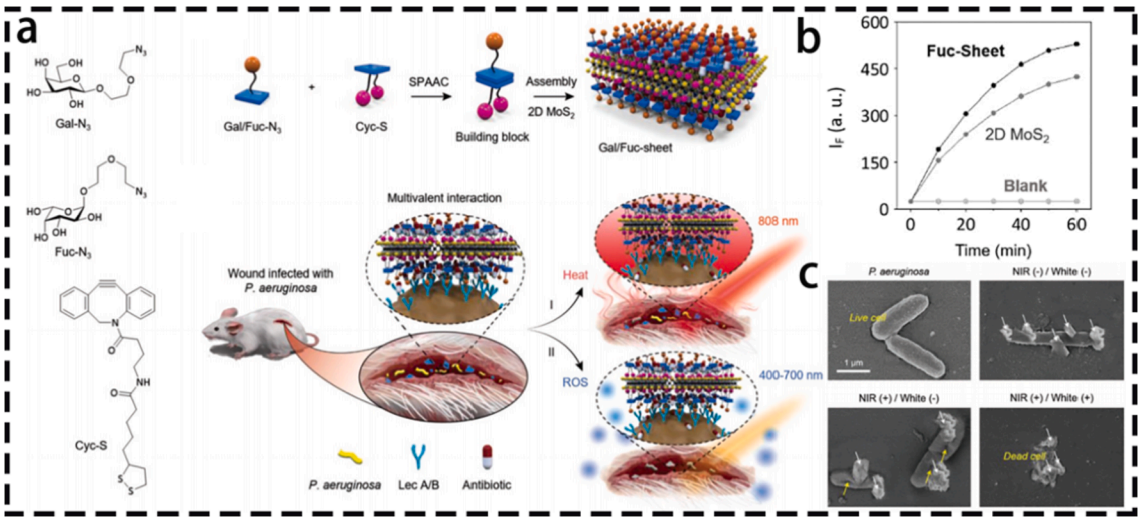

Fig. 37. (a) Construction of the antimicrobial glycosheets for double light-driven therapy of *Pseudomonas aeruginosa* (*P. aeruginosa*) on wounds. (b) The reactive oxygen species productivity of 2D MoS_2 and Fuc-sheet upon white light (400–700 nm; 1 W cm^{-2}) irradiation measured by a fluorogenic probe. (c) Morphological analysis of *P. aeruginosa* in the absence and presence of Fuc-sheet@CAZ without and with single NIR irradiation (2 h) or double-light irradiation (2 h) of NIR followed by 1 h of white light). The wavelength of NIR and white light is 808 nm (1 W cm^{-2}) and 400–700 nm (1 W cm^{-2}), respectively [298]. Adapted with permission. Copyright 2019, Wiley-VCH.

In addition, antigen–antibody proteins were targeted on the surface of bacterial cell membranes [297]. Hu et al. designed thin layers of MoS_2-based multivalent glycosheets, which targeted and treated multiple drug-resistant (MDR) *P. aeruginosa* wounds under light irradiation (Fig. 37**a**) [298]. A dense sugar alcohol layer formed on the MoS_2 surface using galactose- and fucose-based ligands, which facilitated the selective capture of carbohydrate-binding proteins on the surface of *P. aeruginosa*. After excitation by 808 nm NIR radiation at a power density of 1 W cm^{-2}, the glycoside tablets effectively generated hyperthermia *in situ*. Hyperthermia is important for increasing the permeability of bacterial membranes and reducing bacterial tolerance. Furthermore, under the synergistic action of ROS generated under visible light irradiation, the bacteria were thoroughly inactivated (Fig. 37**b, c**).

4.2. Magnetic field synergy

Magnetic materials effectively captured bacteria under the action of a magnetic field [299]. In addition, the negative magnetoresistance effect under an external magnetic field increased the mobility of carriers, thereby reducing the probability of carrier recombination at the interface and increasing the photocatalytic efficiency of the entire system [300]. Jia et al. synthesized CS-functionalized magnetic graphene oxide as a multifunctional therapeutic agent using the hydrothermal method (Fig. 38**a**) [301]. CS effectively contacted and trapped bacteria through the positively charged functional groups on its surface. GO is a common PTA used in the field of antibacterials because of its photothermal properties. The superparamagnetism of iron oxide makes bacteria easy to separate and aggregate under an external magnetic field, thereby improving the efficiency of photothermal sterilization (Fig. 38**b-d**). As a result, the bacteria were effectively eliminated, and the bacterial biofilm was destroyed after 10 min of NIR light irradiation. In addition, the antibacterial agent was regenerated by external magnets and reused in subsequent antibacterial applications [302]. Zhang et al. also constructed a multifunctional CS-functionalized magnetic MoS_2 to effectively eliminate pathogenic bacteria and treat diseased infections [303]. Wu et al. proposed rGO functionalized by glutaraldehyde and superparamagnetic Fe_2O_3, which showed excellent NIR photothermal conversion efficiency [304]. Under the action of an external magnetic field, bacteria gathered in a small area so that hyperthermia could better eliminate concentrated bacteria and improve killing efficiency [305].

4.3. Nitric oxide synergy

Nitric Oxide (NO) is a typical lipophilic biosignal molecule and a broad-spectrum antibacterial drug candidate, regardless of bacteria type [306,307]. It is a kind of diatomic free radical with strong reducing properties. The byproducts, such as peroxynitrite, produced after the reaction caused a stress reaction in bacteria and destroyed their immune system, leading to lipid peroxidation, cell membrane rupture, and DNA deamination [308]. Therefore, the synergistic effects of NO gas therapy effectively enhanced the antibacterial effects of 2DNMs [309].

Gao et al. developed a hybrid system of MoS_2 and a heat-sensitive agent of N,N'-di-*sec*-butyl-N,N'-dinitroso-1,4-phenylenediamine (BNN6) (Fig. 39**a-c**) [310]. MoS_2 had a large surface area and good NIR photothermal conversion performance. BNN6 showed good photosensitivity and released NO in response to heat. Excited by 808 nm laser radiation, MoS_2-BNN6 generated local hyperthermia at the infected site and simultaneously transmitted NO, inducing the destruction of bacteria through PTT/NO synergy (Fig. 39**d-f**). In addition, MoS_2 accelerated the oxidation of GSH and destroyed the balance of redox reactions in bacteria, thereby enhancing the inactivation effects of the system. Therefore, after 10 min of radiation, MoS_2-BNN6 achieved an efficient antibacterial effect of 97.2% (Fig. 39**g**). Huang et al. reported a hydrogel system based on NIR photothermal activity, which was prepared by methacrylate-modified gelatin with HA-grafted dopamine as a carrier and loaded with β-cyclodextrin functionalized GO and NO donor BNN6 [311]. The

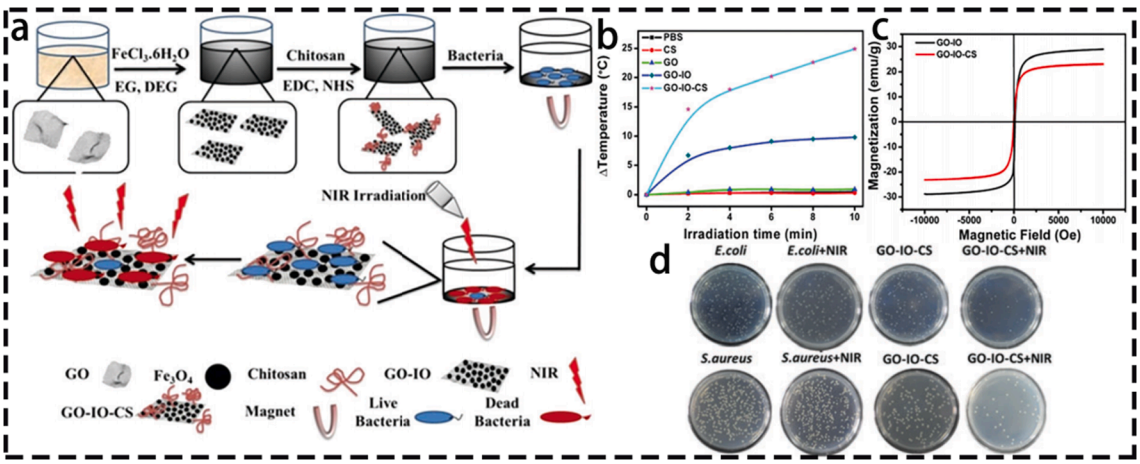

Fig. 38. (a) A schematic diagram showing the preparation of GO-IO-CS nanocomposites and their antibacterial application. (b) Temperature changes after NIR irradiation for 10 min with various materials. (c) Room-temperature magnetization curves of GO-IO and GO-IO-CS nanocomposites. (d) The corresponding bacterial colonies treated with GO-IO-CS, with and without NIR [301]. Adapted with permission. Copyright 2017, Royal Society of Chemistry.

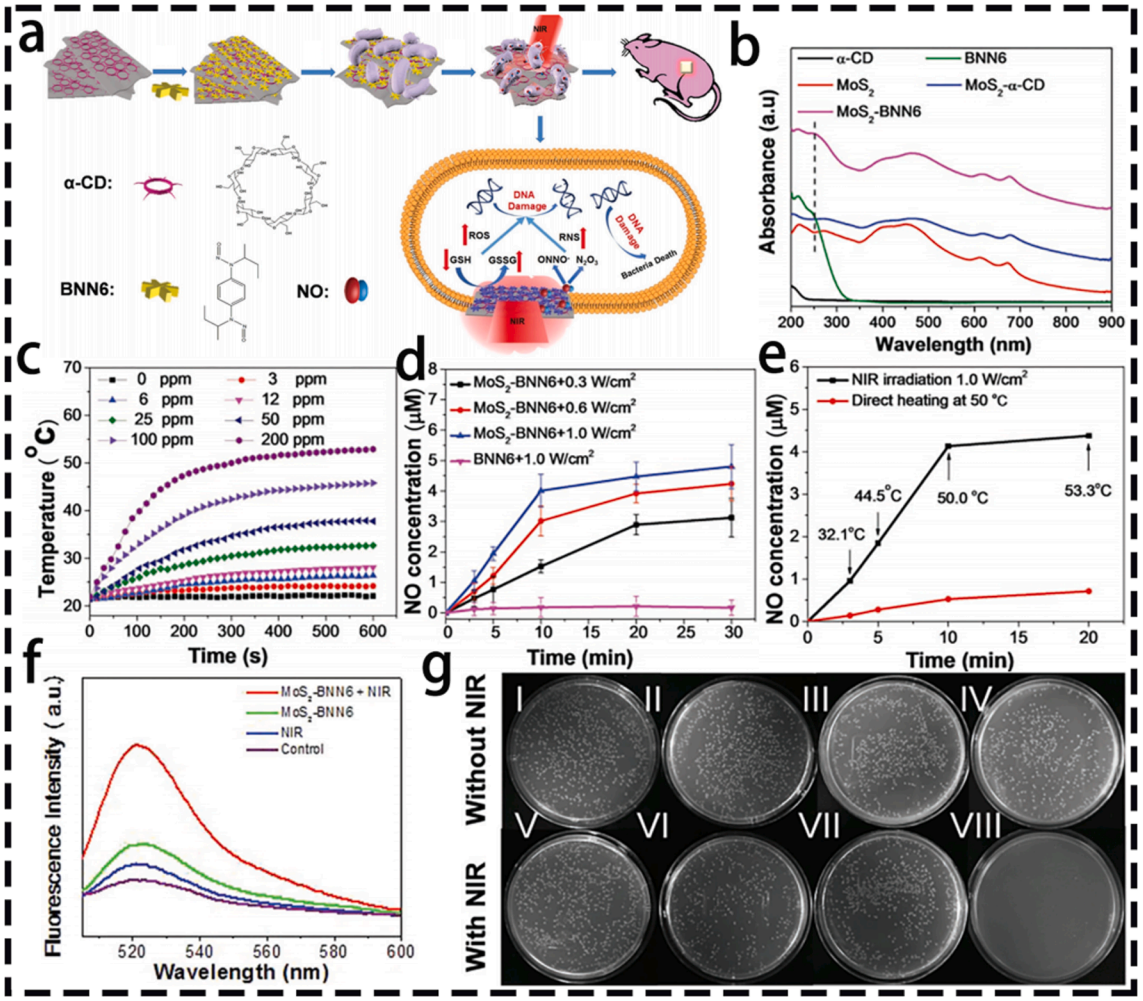

Fig. 39. (a) Schematic illustration of MoS_2-BNN6 as NIR laser-mediated NO release nanovehicle for synergistic eliminating bacteria. (b) UV–vis-NIR spectra of MoS_2, MoS_2-α-CD before and after loading with BNN6. (c) Photothermal effect of MoS_2-α-CD with different concentrations irradiated by 808 nm laser. (d) NO release curves of MoS_2-BNN6 under varying power densities irradiation of 808 nm laser. (e) Effects of direct heating and 808 nm laser irradiation on NO release from MoS_2-BNN6. (f) Measurement of ROS production in *Ampr E. coli* using DCFH-DA assay when MoS_2-BNN6 exposed to 808 nm laser. (g) Photographs of bacterial colonies formed by *Ampr E. coli* treated with (I) PBS, (II) MoS_2-α-CD, (III) BNN6, (IV) MoS_2-BNN6, (V) PBS + NIR, (VI) MoS_2-α-CD + NIR, (VII) BNN6 + NIR and (VIII) MoS_2-BNN6 + NIR [310]. Adapted with permission. Copyright 2018, Wiley-VCH.

synergy between PTT and gas therapy was expected to achieve excellent antibacterial efficiency while avoiding drug resistance. The results showed that the hydrogel had high antibacterial activity and mechanical properties as well as good adhesion and biocompatibility with tissues.

4.4. Drug delivery synergy

The delicate balance between therapeutic efficacy and side effects determines the suitability of antibiotics. Controlled release technology was expected to reduce side effects and improve treatment efficiency [312]. With the development of nanoscience and nanotechnology, new drug-delivery systems continue to emerge. Among them, 2DNMs have attracted much attention in the field of drug delivery because of their unique properties of meeting the requirements of nano-drug carriers [313–315]. The diversity of 2DNMs provides a wealth of options for various nanobiological applications. Their excellent physical and chemical properties guarantee high drug loading and application of nanodrugs. In addition, their preparation process is simple, which facilitates mass production. The release rates of drugs are affected by various factors, such as loading material, temperature, pH, and intermolecular forces [316–318].

For example, Huang et al. combined ofloxacin antibiotics with mild PTT to achieve high antibacterial efficiency [319]. MoS_2 nanosheets were used as effective NIR photothermal agents, and positively charged quaternary ammonium chitosan (QCS) was used to improve their dispersion stability and enhance their interactions with bacterial membranes (Fig. 40**a, b**). Ofloxacin antibiotics were

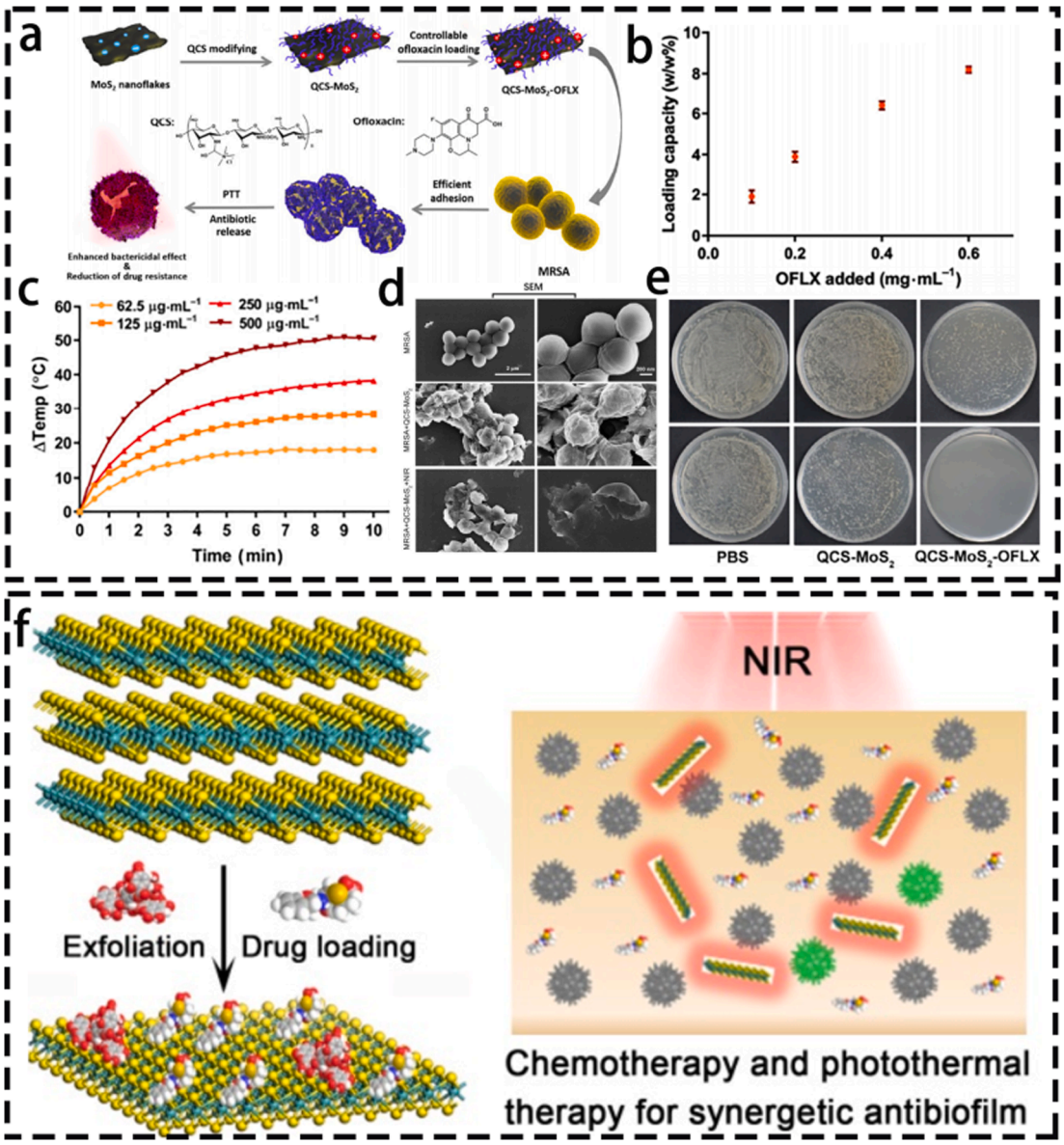

Fig. 40. (a) Schematic illustration of the preparation of QCS-MoS_2-OFLX and antibiotic-photothermal synergistic therapy against *MRSA* bacteria. (b) Loading capacity of ofloxacin on QCS-MoS_2 as the function of originally added drug concentrations. (c) Temperature evolution curve of QCS-MoS_2 with different concentrations. (d) Morphology change of *MRSA* after incubated with QCS-MoS_2 in the presence or absence of NIR irradiation. (e) *MRSA* suspension added to TSA medium after incubated with different samples with or without NIR irradiation [319]. Adapted with permission. Copyright 2020, Springer Nature. (f) Schematic illustration for the biofilm resistance mechanism of MOS_2-Pen [323]. Adapted with permission. Copyright 2018, American Chemical Society.

loaded onto QCS-MoS_2 through π-π stacking and hydrophobic interactions, thereby controlling the release of antibiotics. Their results showed that the nanosheets effectively adhered to the bacterial surface, and the temperature of the system rose to 45 °C within 5 min under NIR light irradiation. In addition to an antibacterial effect, mild photothermal was beneficial for changing the permeability of bacterial membranes, so the system showed an excellent bactericidal effect (82%) under the loading of a lower concentration of antibiotics (8 μg·mL^{-1}) (Fig. 40**c-e**). In addition, the formation of hydrogen bonds plays an important role in the slow release of the drug [320]. Liang et al. used an H_2O_2/horseradish peroxidase system to prepare a series of antibacterial hydrogels based on HA-grafted dopamine and rGO [321]. Their results showed that, due to the hydrogen bonds between the amino groups on the drug surface and the hydrogel network, the sustained release time of the drug was greatly prolonged, and the drug was released from the hydrogel by diffusion. In addition, under the synergistic effects of the photothermal effect, the hydrogel exhibited significantly enhanced antibacterial behavior *in vitro* and *in vivo*. Because of the different pH values of the microenvironment inside and outside the cell, the solubility of the drug-encapsulating agent in different pH environments is also different, resulting in different release rates. For

instance, Ma et al. prepared polyethylene glycol (PEG)-modified MoS_2 by a hydrothermal method, which was loaded with gentamicin (Gent) by electrostatic adsorption and finally encapsulated with CS to obtain a CS/Gent/PEG/MoS_2 composite system [322]. After continuous irradiation by 808 nm NIR light (0.5 W cm^2) for 25 min, the release rate of CS/Gent/PEG/MoS_2 at pH 5.5 was 2.5 times that at pH 7.4 due to the accelerated solution of CS at pH 5.5, so controllable drug release was achieved. In addition, the hyperthermia generated by the coating not only promoted the release of the system drug Gent, but also enhanced the membrane permeability of bacteria. Locally released Gent entered the interior of bacteria and bound to ribosomes to inhibit protein synthesis, thereby disrupting membrane integrity. The rupture of the cell membrane reduced the metabolism of the bacteria, leading to cytoplasmic efflux and bacterial death. This system achieved antibacterial rates of 99.93% and 99.19% against *E. coli* and *S. aureus*, respectively. Finally, temperature was a factor that determined the rate of drug release. Zhang et al. reported a polyphenol-assisted water exfoliation method for exfoliating bulk TMD into a monolayer or a few layers of nanosheets to load the antibiotic penicillin (Pen) [323]. They found that the light absorption of the exfoliated material was significantly enhanced, exhibiting a higher photothermal conversion performance (Fig. 40**f**). Because bacterial cells adhere to form biofilms, they are irreversibly attached to material or tissue surfaces and are further sealed by self-produced EPS. On one hand, EPS biofilm acted as a tight barrier to prevent the penetration of antibiotics by inhibiting diffusion, resulting in strong bacterial resistance to antibiotics. On the other hand, bacteria in the middle or bottom of the biofilm grew slowly or remained dormant due to the encapsulation of EPS, resulting in a sharp decline in bacterial susceptibility to antibiotics. Therefore, bacterial cells in biofilms were shown to be 1,000 times more resistant to antibiotics than planktonic bacterial cells. However, the elevated temperature of the photothermal system not only regulated the release of the drug but also affected the tissue structure of the formed biofilm, further promoting the diffusion of the drug through the biofilm and reducing tolerance to Pen when bacteria grew slowly or remained dormant on biofilms.

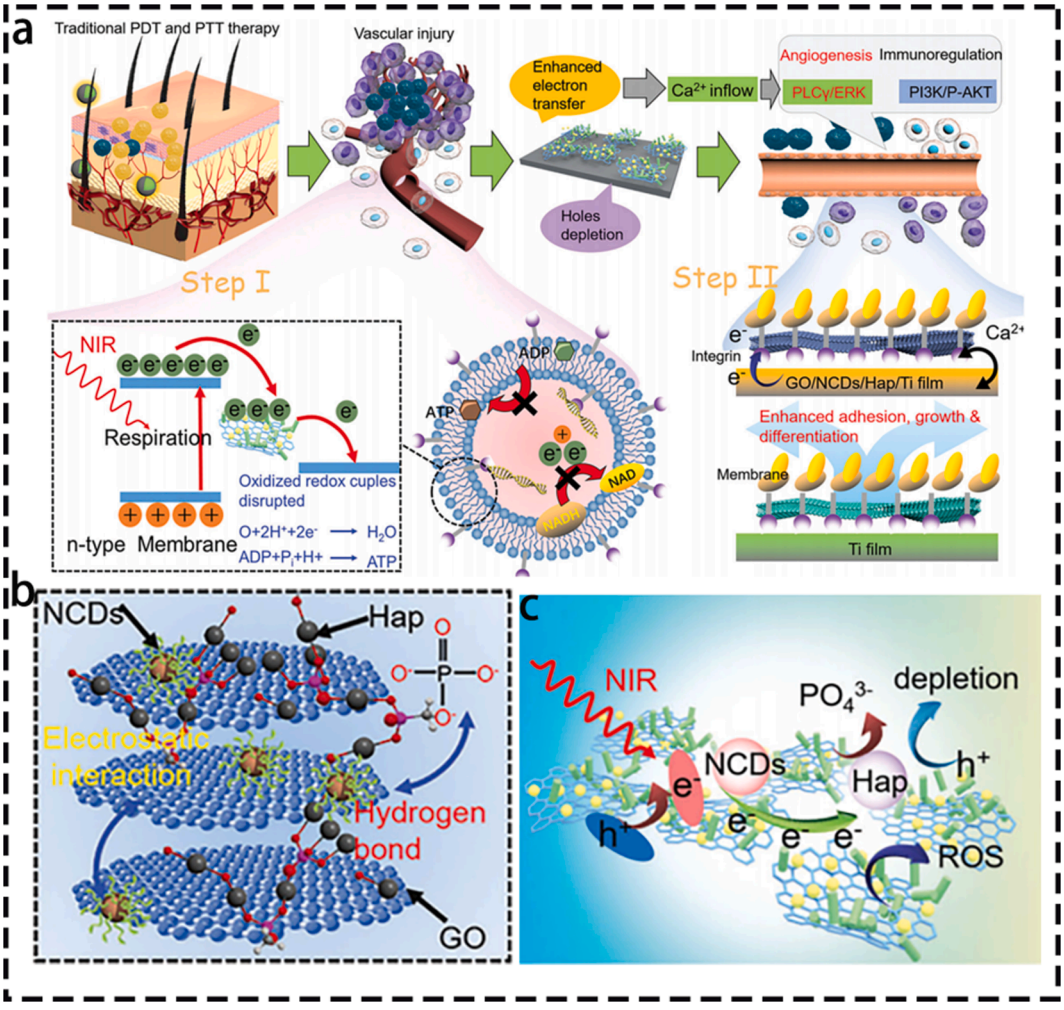

Fig. 41. (a) The mechanism of mild phototherapy using a GO/NCD/Hap film, which can repair injured vessels and simultaneously relieve inflammation reaction, thus promising a safe and noninvasive phototherapy in the near future. (b) The structure sketch map and binding forces of GO/NCDs/Hap/Ti. (c) The promoted separation of interfacial electrons and holes and inhibited recombination efficiency by and dissociated PO_4^{3-} [325]. Adapted with permission. Copyright 2020, Wiley-VCH.

4.5. Immunotherapy synergy

Immunotherapy is the treatment of diseases through artificial interventions that enhance or inhibit human immune function [324]. It can also be combined with 2DNMs to achieve better antibacterial therapeutic efficiency. Li et al. developed a light-excited hydroxyapatite (Hap)/N-doped CDs (NCDs)-modified GO heterojunction film (Fig. 41**a, b**) [325]. Under illumination, the metabolism of bacteria was significantly inhibited by enhanced photocatalytic and photothermal effects. After 15 min of NIR light irradiation, the composite membrane achieved 98.9% antimicrobial activity against *S. aureus*. One reason for this result was that the biological redox potential of the bacterial transmembrane protein complex in the respiratory chain was between −4.1 and −4.8 eV, which was higher than the CB of the complex system. As a result, the electrons on the film were spontaneously transferred to the surface of the material. The transferred electrons further inhibited the process of bacterial ATP synthesis, and the membrane potential increased, resulting in the interruption of the respiratory chain and the destruction of the membrane structure. The ROS generated by light excitation also greatly reduced the bacterial biochemical reaction and inhibited the ATP synthesis process of *S. aureus* (Fig. 41**c**). In addition, the electrons transferred between the system and the cell membrane after irradiation induced the flow of calcium ions (Ca^{2+}), which was beneficial for tissue cell migration and proliferation and enhanced alkaline phosphatase, thereby promoting tissue reconstruction. Ca^{2+} activated the PLCγ1/ERK pathway and promoted the repair of vascular injury by enhancing the expression of CD31. In addition, activation of the PI3K/P-AKT pathway improved the increase in CD^{4+}/CD^{8+} lymphocytes and effectively reduced inflammation.

5. Other antimicrobial strategies

In addition to the above strategies, some 2DNMs have presented good therapeutic effects under other exogenous stimuli due to their piezoelectric and dielectric properties. Microwave hyperthermia and ultrasound therapy, as well as a combination of other techniques, have been reported to be effective in enhancing the antibacterial efficacy of 2DNMs [326].

5.1. Microwave-assisted antimicrobial therapy

Microwaves (MW) are promising for the treatment of deep tissue infections because of their deep tissue penetration [327]. In addition, Microwave irradiation can generate microwave heat to eliminate bacteria. In recent studies, some 2DNMs have been found to be thermally responsive to microwaves and to locally generate perfect thermal properties at lower power densities, leading to significant therapeutic effects while reducing side effects on tissue damage [328]. Microwave hyperthermia has attracted much attention for use in medical treatment. Wang et al. prepared layered MoS_2 nanolayers using a simple bottom-up hydrothermal method (Fig. 42**a, b**) [329]. Coating MoS_2 nanomaterials with bovine serum albumin (BSA-MoS_2) induced low biological toxicity and sharp microwave responsiveness *in vitro*. The sample concentration was 30 mg/mL, after 1 min of irradiation, the temperature reached 42 °C, and then rose to 53 °C within 5 min (Fig. 42**c-e**). The microwave heating effect was due to ions and dipoles. Therefore, BSA-MoS_2 dispersed in saline showed a better MW heating effect than in aqueous solvent because of the large amount of sodium ions in normal saline. The

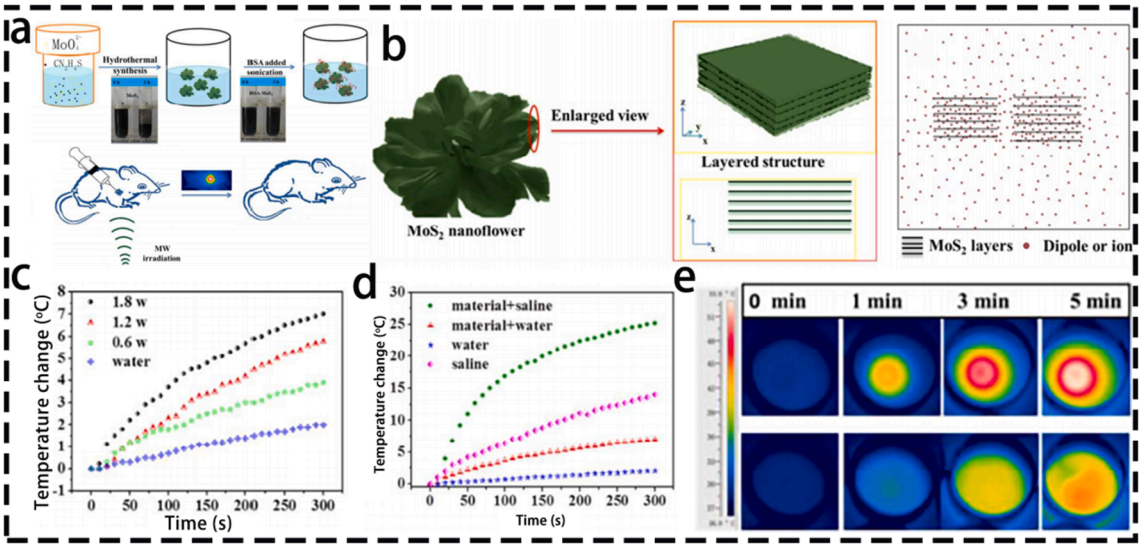

Fig. 42. (a) Schematical illustration of the synthesis process of BSA-MoS_2 nanoflowers as a nanoagent for MW thermal therapy. (b)The structure diagram of MoS_2 nanoflower, and the schematic drawing of dipoles or ions distribution in solution. (c) Infrared thermal images of normal saline and BSA-MoS_2 nanoflowers dispersed in saline solution (30 mg mL^{-1}, 1.8 W, 450 MHz) *in vitro*. (d) MW heating of BSA-MoS_2 dispersed in deionized water at different power (0.6 W, 1.2 W and 1.8 W). (e) MW heating of BSA-MoS_2 dispersed in deionized water and saline solution (30 mg mL^{-1}, 1 mL, 1.8 W, 450 MHz) [329]. Adapted with permission. Copyright 2020, Royal Society of Chemistry.

main mechanism of heat generation was that the structure and size of MoS_2 nanosheets easily led to the recruitment and enrichment of Na^+, resulting in a higher ion concentration on the surface. Under the irradiation of MW, the ions gathered between the layers were aligned in the oscillating electric field, and the resulting intermolecular friction and dielectric loss generated heat, thereby enhancing the effect of hyperthermia.

5.2. *Ultrasound antimicrobial therapy*

Piezoelectric materials have promising applications for converting mechanical energy into chemical energy (i.e., piezoelectric catalysis) by combining the piezoelectric effect with electrochemical processes [330–332]. 2DNMs, such as BP and transition metal dihalide compounds (i.e., MoS_2, WS_2, and WSe_2) exhibit this property [333,334]. Ultrasonic mechanical energy stimulates 2DNMs to generate ROS, and the time and sites of ROS generation are controllable. Ultrasound is transmitted to deep tissue, so this technology has positive effects on deep tissue infection.

For example, BP nanosheets have the property of ultrasound-induced ROS generation [335]. When ultrasonic waves induced mechanical strain in the BP nanosheets, piezoelectric polarization occurred, and the surface electrons and holes were separated, which in turn led to the formation of a piezoelectric field. Under ultrasonic irradiation, a piezoelectric potential difference of about 0.1 V was generated from the BP nanosheets, resulting in tilting of their energy bands. At this point, the CB of BP was negative, and the VB was

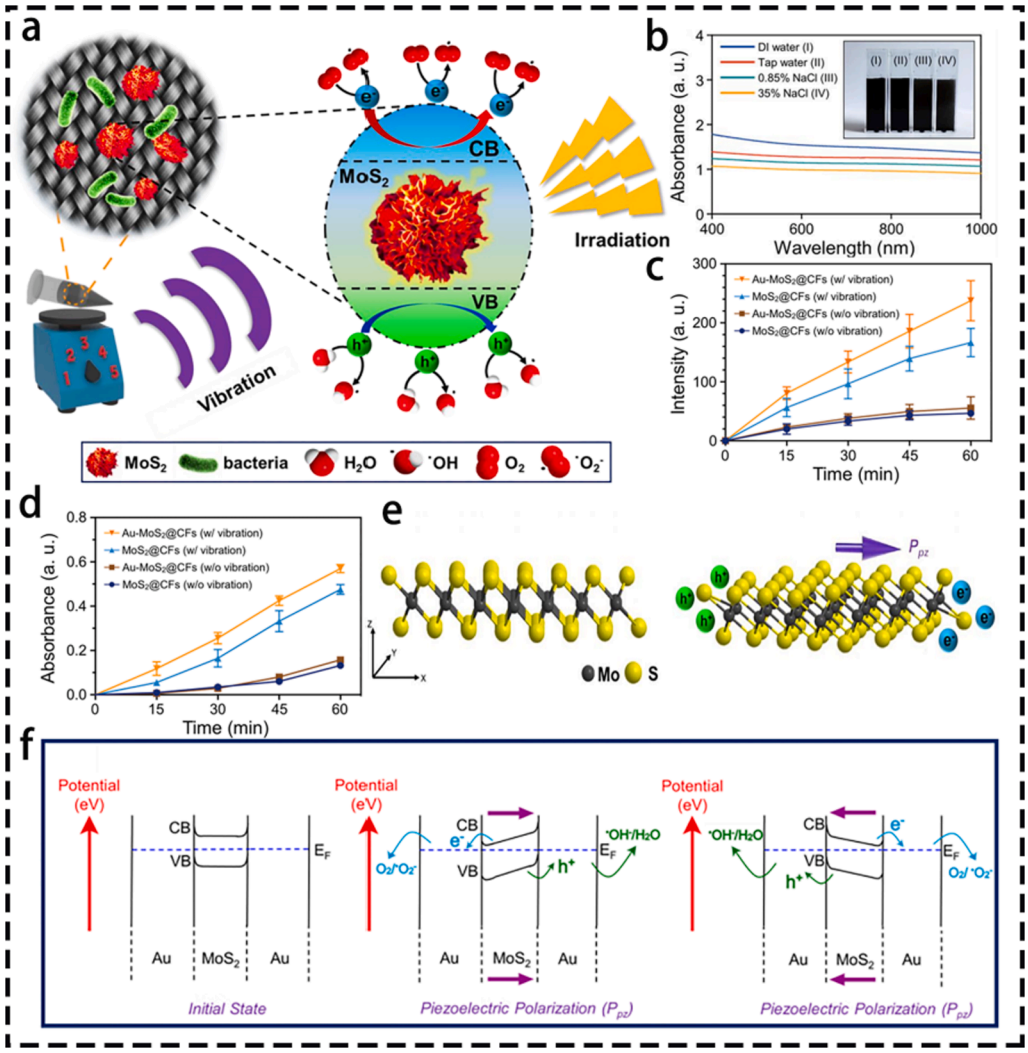

Fig. 43. (a) Schematic of the Au-MoS_2 nanocatalyst for water disinfection application. (b) Absorbance spectra of suspensions of synthesized MoS_2 NSs in different aqueous solutions. Characterization of ROS generation under different sample conditions by fluorescence for (c) •OH radicals and absorbance for (d) superoxide anions. (e) Schematic diagram of MoS_2 without an external force, and charge transfer to compensate for the electric field generated by piezoelectric polarization at active edge sites under an external force. (f) Illustration of the piezocatalytic reaction in Au-MoS_2@CFs to enhance ROS generation and EHP separation [336]. Adapted with permission. Copyright 2020, Elsevier B.V.

positive, both of which met the energy band requirements for ROS generation. In another study, monolayer, and multilayer MoS_2 nanosheets were shown to generate piezoelectric polarization under the ultrasonic piezoelectric effect (mechanical vibration), taking advantage of their noncentrosymmetric structure, which then induced a catalytic reaction to generate ROS to deactivate bacteria (Fig. 43**a, b**) [336]. Loading Au NPs on MoS_2 nanosheets increased the production of ROS and the subsequent disinfection of bacteria. When exposed to ultrasound or visible light for 45 min, this composite eliminated 99.999% of *E. coli* (Fig. 43**c, d**). The underlying mechanism was that under the action of ultrasound, the internal electric field generated by the piezoelectric polarization of MoS_2 nanosheets caused the band gap to bend (Fig. 43**e, f**). Moreover, MoS_2 and Au were in close contact to form a typical Schottky interface, which led to the facile movement of electrons to Au. Therefore, the separated electrons and holes reacted with water and O_2 to generate ROS, showing that the 2DNM had efficient antibacterial activity.

6. Conclusions and prospects

As shown in this review, the application of 2DNMs in the antibacterial field has been a booming trend in the past decade. Their potential applications have attracted extensive attention because of their unique 2D structure and tunable energy bands. Biological research on 2DNMs, such as antibacterial and wound healing, is a current hot topic. This review study has traced recent research on 2DNMs in the field of antibacterials, including their inherent antibacterial properties, their photodynamic and photothermal antibacterial properties, and their antibacterial mechanisms, as well as the methods used to improve their properties. The application of 2DNMs under microwave and ultrasound stimulation was expanded. We expect that the findings of the present review of the relevant literature will drive the development of 2D antimicrobial materials toward a greater number of practical applications. To better develop advanced 2D antibacterial agents, the following pressing issues must be considered:

1. Factors such as thickness, lateral dimensions, and surface functional groups of 2DNMs have decisive impacts on inherent antibacterial properties, including physical contact and oxidative stress. However, the mechanisms by which these parameters affect the antimicrobial efficacy of 2DNMs remain controversial.
2. The effects of inner physical interactions on the properties of materials, such as material defects, lattice orientation, and size, remain unexplored. Moreover, the deep mechanisms of electronic transitions and thermal radiation of 2DNMs after photoexcitation have not been fully explored.
3. The 2DNMs-bacteria interface and the internal reaction to bacteria are still unclear and need to be further explored. Therefore, it is necessary to explore interactions between nanomaterials and microorganisms at the molecular level to understand their specific antibacterial mechanisms. To develop antibacterial drugs required for comprehensive treatment, it is necessary to understand the physical properties of 2DNMs, the production of ROS and heat, and their effects on tissues. Only in this way could we gain a clear understanding of the relationships among the composition, structure, and properties of 2DNMs, which have important implications for future drug development.
4. The application of 2DNMs cannot be ignored. There are different requirements and needs for 2DNMs in different fields. In different exogenous stimuli, 2DNMs have different degrees of response. Therefore, to fully utilize the performance of 2DNMs, it is crucial to design and develop nanosystems for different application scenarios. For example, light can be applied to superficial wound healing and dental implants due to poor light penetration. For *in vivo* applications, more penetrating exogenous means, such as microwaves and ultrasounds, are required. These areas require more attention in the research.
5. Biosafety is a prerequisite for 2DNMs in clinical antibacterial applications. Many studies on the biological modification of 2DNMs have been published, and many biological experiments have been performed. Despite the excellent biocompatibility and low toxicity of 2DNMs after proper functionalization, biological information about them is still lacking. Therefore, its safety performance should be checked. Regarding the metabolism of 2DNMs, although some previous studies have focused on enhancing their biodegradability through surface functionalization or by designing ultra-small 2DNMs for easier removal from the body, the biotoxicity mechanism remains unexplored. Therefore, it is crucial to address these unresolved biosafety issues and conduct in-depth studies that will benefit future preclinical or clinical antimicrobial applications of 2DNMs.

In summary, based on in-depth research and the realization of more functional requirements, 2DNMs have received increasing attention in the literature. However, we are only one step closer to a greater number of practical clinical applications, and there are still many challenges that need to be solved. We hope that this review of the literature on 2DNMs in the field of biomaterials will contribute to the design and development of novel nanosystems for clinical applications in the future.

Declaration of Competing Interest

The authors declare that they have no known competing financial interests or personal relationships that could have appeared to influence the work reported in this paper.

Acknowledgements

This work is jointly supported by the China National Funds for Distinguished Young Scientists (No.51925104), and the National Natural Science Foundation of China (Nos. 51871162, and 52173251), NSFC-Guangdong Province Joint Program (Key program no. U21A2084).

References

[1] Fleming A. On the antibacterial action of cultures of a penicillium, with special reference to their use in the isolation of B. influenzae. Br J Exp Pathol 1929;10:226–36.
[2] Smith PA, Koehler MFT, Girgis HS, Yan D, Chen Y, Chen Y, et al. Optimized arylomycins are a new class of gram-negative antibiotics. Nature 2018;561:189–94.
[3] Liu Y, Bai P, Woischnig AK, Charpin-El Hamri G, Ye H, Folcher M, et al. Immunomimetic designer cells protect mice from. *MRSA* Infection. Cell 2018;174:259–70.
[4] Baker S, Thomson N, Weill FX, Holt KE. Genomic insights into the emergence and spread of antimicrobial-resistant bacterial pathogens. Science 2017;360:733–8.
[5] Novoselov KS, Geim AK, Morozov SV, Jiang DE, Zhang Y, Dubonos SV, et al. Electric field effect in atomically thin carbon films. Science 2004;306:666–9.
[6] Xia F, Wang H, Xiao D, Dubey M, Ramasubramaniam A. Two-dimensional material nanophotonics. Nat Photonics 2014;8:899–907.
[7] Zou X, Zhang L, Wang Z, Luo Y. Mechanisms of the antimicrobial activities of graphene materials. J Am Chem Soc 2016;138:2064–77.
[8] Robinson JT, Tabakman SM, Liang Y, Wang H, Sanchez Casalongue H, Vinh D, et al. Ultrasmall reduced graphene oxide with high near-infrared absorbance for photothermal therapy. J Am Chem Soc 2011;133:6825–31.
[9] Liu X, Duan G, Li W, Zhou Z, Zhou R. Membrane destruction-mediated antibacterial activity of tungsten disulfide (WS_2). RSC Adv 2017;7:37873–80.
[10] Li Y, Yang M, Xing Y, Liu X, Yang Y, Wang X, et al. Preparation of carbon-rich *g*-C_3N_4 nanosheets with enhanced visible light utilization for efficient photocatalytic hydrogen production. Small 2017;13:1701552.
[11] Zhang T, Jiang X, Li G, Yao Q, Lee JY. A red-phosphorous-assisted ball-milling synthesis of fewlayered $Ti_3C_2T_x$ (MXene) nanodot composite. ChemNanoMat 2018;4:56–60.
[12] Aksoy L, Küçükkeçeci H, Sevgi F, Metin Ö, Hatay PI. Photothermal antibacterial and antibiofilm activity of black phosphorus/gold nanocomposites against pathogenic bacteria. ACS Appl Mater Interfaces 2020;12:26822–31.
[13] Merlo A, Mokkapati VRSS, Pandit S, Mijakovic I. Boron nitride nanomaterials: biocompatibility and bio-applications. Biomater Sci 2018;6:2298–311.
[14] Zhang H. Ultrathin two-dimensional nanomaterials. ACS Nano 2015;9:9451–69.
[15] Mei L, Zhu S, Yin W, Chen C, Nie G, Gu Z, et al. Two-dimensional nanomaterials beyond graphene for antibacterial applications: current progress and future perspectives. Theranostics 2020;10:757–81.
[16] Yin T, Liu J, Zhao Z, Zhao Y, Dong L, Yang M, et al. Redox sensitive hyaluronic acid-decorated graphene oxide for photothermally controlled tumor-cytoplasmselective rapid drug delivery. Adv Funct Mater 2017;27:1604620.
[17] Rai MK, Deshmukh SD, Ingle AP, Gade AK. Silver nanoparticles: the powerful nanoweapon against multidrug-resistant bacteria. J Appl Microbiol 2012;112:841–52.
[18] Paladini F, Pollini M, Sannino A, Ambrosio L. Metal-based antibacterial substrates for biomedical applications. Biomacromolecules 2015;16:1873–85.
[19] Zhu P, Weng Z, Li X, Liu X, Wu S, Yeung KWK, et al. Biomedical applications of functionalized ZnO nanomaterials:from biosensors to bioimaging. Adv Mater Interfaces 2016;3:1500494.
[20] Choudhary A, Naughton LM, Montánchez I, Dobson ADW, Rai DK. Current status and future prospects of marine natural products (MNPs) as antimicrobials. Mar Drugs 2017;15:272.
[21] Saidin S, Jumat MA, Amin NAAM, Al-Hammadi ASS. Organic and inorganic antibacterial approaches in combating bacterial infection for biomedical application. Mater Sci Eng C 2021;118:111382.
[22] Palza H. Antimicrobial polymers with metal nanoparticles. Int J Mol Sci 2015;16:2099–116.
[23] Usman MS, El Zowalaty ME, Shameli K, Zainuddin N, Salama M, Ibrahim NA. Synthesis, characterization, and antimicrobial properties of copper nanoparticles. Int J Nanomed 2013;8:4467–79.
[24] Rai M, Yadav A, Gade A. Silver nanoparticles as a new generation of antimicrobials. Biotechnol Adv 2009;27:76–83.
[25] Guyomard A, Dé E, Jouenne T, Malandain JJ, Muller G, Glinel K. Incorporation of a hydrophobic antibacterial peptide into amphiphilic polyelectrolyte multilayers: a bioinspired approach to prepare biocidal thin coatings. Adv Funct Mater 2008;18:758–65.
[26] Cao F, Ju E, Zhang Y, Wang Z, Liu C, Li W, et al. An efficient and benign antimicrobial depot based on silver-infused MoS_2. ACS Nano 2017;11:4651–9.
[27] Mangadlao JD, Santos CM, Felipe MJL, De Leon ACC, Rodrigues DF. Advincula RC, On the Antibacterial Mechanism of Graphene Oxide (GO) Langmuir-Blodgett Films. Chem Commun 2015;51:2886–9.
[28] Mao C, Xiang Y, Liu X, Cui Z, Yang X, Yeung KWK, et al. Photo-inspired antibacterial activity and wound healing acceleration by hydrogel embedded with Ag/Ag@AgCl/ZnO nanostructures. ACS Nano 2017;11:9010–21.
[29] Siriwardena TN, Stach M, He R, Gan BH, Javor S, Heitz M, et al. Lipidated peptide dendrimers killing multidrug resistant bacteria. J Am Chem Soc 2017;140:423–32.
[30] Kiristi M, Singh VV, Esteban-Fernández de Ávila B, Uygun M, Soto F, Aktaş Uygun D, et al. Lysozyme-Based Antibacterial Nanomotors. ACS Nano 2015;9:9252-9.
[31] Chen Q, Xu L, Liang C, Wang C, Peng R, Liu Z. Photothermal therapy with immune-adjuvant nanoparticles together with checkpoint blockade for effective cancer immunotherapy. Nat Commun 2016;7:13193.
[32] Panda S, Rout TK, Prusty AD, Ajayan PM, Nayak S. Electron transfer directed antibacterial properties of graphene oxide on metals. Adv Mater 2018;30:1702149.
[33] Fan Z, Liu B, Wang J, Zhang S, Lin Q, Gong P, et al. A novel wound dressing based on ag/graphene polymer hydrogel: effectively kill bacteria and accelerate wound healing. Adv Funct Mater 2014;24:3933–43.
[34] Liu C, Xie X, Zhao W, Liu N, Maraccini PA, Sassoubre LM, et al. Conducting nanosponge electroporation for affordable and high efficiency disinfection of bacteria and viruses in water. Nano Lett 2013;13:4288–93.
[35] Chiu CM, Ke YY, Chou TM, Lin YJ, Yang PK, Wu CC, et al. Self-powered active antibacterial clothing through hybrid effects of nanowire-enhanced electric field electroporation and controllable hydrogen peroxide generation. Nano Energy 2018;53:1–10.
[36] Qiao Y, Liu X, Li B, Han Y, Zheng Y, Yeung KWK, et al. Treatment of MRSA-infected osteomyelitis using bacterial capturing, magnetically targeted composites with microwave-assisted bacterial killing. Nat Commun 2020;11:4446.
[37] Ren Y, Han Y, Li Z, Liu X, Zhu S, Liang Y, et al. Ce and Er Co-doped TiO_2 for rapid bacteria- killing using visible light. Bioact Mater 2020;5:201–9.
[38] Huang B, Tan L, Liu X, Li J, Wu S. A facile fabrication of novel stuff with antibacterial property and osteogenic promotion utilizing red phosphorus and near-infrared light. Bioact Mater 2019;4:17–21.
[39] Pang X, Liu X, Cheng Y, Zhang C, Ren E, Liu C, et al. Sono-immunotherapeutic nanocapturer to combat multidrug-resistant bacterial infections. Adv Mater 2019;31:1902530.
[40] Wu Q, Yu J, Li M, Tan L, Ren X, Fu C, et al. Nanoengineering of nanorattles for tumor treatment by CT imaging-guided simultaneous enhanced mcrowave thermal therapy and managing inflammation. Biomaterials 2018;179:122–33.
[41] Sun W, Wu FG. Two-dimensional materials for antimicrobial applications: graphene materials and beyond. Chem Asian J 2018;13:3378–410.
[42] Miao H, Teng Z, Wang C, Chong H, Wang G. Recent progress in two-dimensional antimicrobial nanomaterials. Chem Eur J 2019;25:929–44.
[43] Hashimoto A, Suenaga K, Gloter A, Urita K, Iijima S. Direct evidence for atomic defects in graphene layers. Nature 2004;430:870–3.
[44] Yu H, Shi R, Zhao Y, Bian T, Zhao Y, Zhou C, et al. Alkali-assisted synthesis of nitrogen deficient graphitic carbon nitride with tunable band structures for efficient visible-light-driven hydrogen evolution. Adv Mater 2017;29:1605148.
[45] Seyler KL, Rivera P, Yu H, Wilson NP, Ray EL, Mandrus DG, et al. Signatures of moiré-trapped valley excitons in $MoSe_2/WSe_2$ heterobilayers. Nature 2018;567:66–70.

[46] Wei ZX, Huang WQ, Xu L, Hu W, Peng P, Huang GF. Dual functions of 2D WS_2 and MoS_2-WS_2 monolayers coupled with a Ag_3PO_4 photocatalyst. Semicond Sci Technol 2016;31:095013.
[47] Huang K, Li Z, Lin J, Han G, Huang P. Two-dimensional transition metal carbides and nitrides (MXenes) for biomedical applications. Chem Soc Rev 2018;47:5109–24.
[48] Tian J, Sang Y, Yu G, Jiang H, Mu X, Liu H. A Bi_2WO_6-based hybrid photocatalyst with broad spectrum photocatalytic properties under UV, visible, and near-infrared irradiation. Adv Mater 2013;25:5075–80.
[49] Khan MH, Liu HK, Sun X, Yamauchi Y, Bando Y, Golberg D, et al. Few-atomic-layered hexagonal boron nitride:CVD growth, characterization, and applications. Mater Today 2017;20:611–28.
[50] Horiuchi S, Gotou T, Fujiwara M, Asaka T, Yokosawa T, Matsui Y. Single graphene sheet detected in a carbon nanofilm. Appl Phys Lett 2004;84:2403–5.
[51] Huang X, Qi X, Boey F, Zhang H. Graphene-based composites. Chem Soc Rev 2012;41:666–86.
[52] Hummers Jr WS, Offeman RE. Preparation of graphitic oxide. J Am Chem Soc 1958;80:1339.
[53] Yuan Z, Xiao X, Li J, Zhao Z, Yu D, Li Q. Self-assembled graphene-based architectures and their applications. Adv Sci 2018;5:1700626.
[54] Di J, Xia J, Li H, Liu Z. Freestanding atomically-thin two-dimensional materials beyond graphene meeting photocatalysis: opportunities and challenges. Nano Energy 2017;35:79–91.
[55] Li R, Mansukhani ND, Guiney LM, Ji Z, Zhao Y, Chang CH, et al. Identification and optimization of carbon radicals on hydrated graphene oxide for ubiquitous antibacterial coatings. ACS Nano 2016;10:10966–80.
[56] Karahan HE, Wiraja C, Xu C, Wei J, Wang Y, Wang L, et al. Graphene materials in antimicrobial nanomedicine: current status and future perspectives. Adv Healthc Mater 2018;7:1701406.
[57] Zeng X, McCarthy DT, Deletic A, Zhang X. Silver/reduced graphene oxide hydrogel as novel bactericidal filter for point-of-use water disinfection. Adv Funct Mater 2015;25:4344–51.
[58] Krishnamoorthy K, Veerapandian M, Zhang LH, Yun K, Kim SJ. Antibacterial efficiency of graphene nanosheets against pathogenic bacteria *via* lipid peroxidation. J Phys Chem C 2012;116:17280–7.
[59] Zheng K, Li K, Chang TH, Xie J, Chen PY. Synergistic antimicrobial capability of magnetically oriented graphene oxide conjugated with gold nanoclusters. Adv Funct Mater 2019;29:1904603.
[60] Zheng Y, Lin L, Wang B, Wang X. Graphitic carbon nitride polymers toward sustainable photoredox catalysis. Angew Chem Int Ed 2015;54:12868–84.
[61] Zhang J, Guo F, Wang X. An optimized and general synthetic strategy for fabrication of polymeric carbon nitride nanoarchitectures. Adv Funct Mater 2013;23:3008–14.
[62] Wang F, Feng Y, Chen P, Wang Y, Su Y, Zhang Q, et al. Photocatalytic degradation of fluoroquinolone antibiotics using ordered mesoporous g-C_3N_4 under simulated sunlight irradiation:kinetics, mechanism, and antibacterial activity elimination. Appl Catal B 2018;227:114–22.
[63] Liu H, Ma S, Shao L, Liu H, Gao Q, Li B, et al. Defective engineering in graphitic carbon nitride nanosheet for efficient photocatalytic pathogenic bacteria disinfection. Appl Catal B 2020;261:118201.
[64] Liao G, He F, Li Q, Zhong L, Zhao R, Che H, et al. Emerging graphitic carbon nitride-based materials for biomedical applications. Prog Mater Sci 2020;112:100666.
[65] Song J, Wu X, Zhang M, Liu C, Yu J, Sun G, et al. Highly Flexible, Core-Shell Heterostructured, and Visible-Light-Driven Titaniabased Nanofibrous Membranes for Antibiotic Removal and *E. coil* Inactivation. Chem Eng J 2020;379:122269.
[66] Lu Z, Wei Y, Deng J, Ding L, Li ZK, Wang H. Self-crosslinked MXene (Ti_3C_2Tx) membranes with good anti-swelling property for monovalent metal ions exclusion. ACS Nano 2019;13:10535–44.
[67] Rafieerad A, Amiri A, Yan W, Eshghi H, Dhingra S. Conversion of 2D MXene to multi-low-dimensional GerMXene superlattice heterostructure. Adv Funct Mater 2022;32:2108495.
[68] Wang W, Feng H, Liu J, Zhang M, Liu S, Feng C, et al. A photo catalyst of cuprous oxide anchored MXene nanosheet for dramatic enhancement of synergistic antibacterial ability. Chem Eng J 2020;386:124116.
[69] Mayorga-Martinez CC, Sofer Z, Sedmidubský D, Luxa J, Kherzia B, Pumera M. Metallic impurities in black phosphorus nanoflakes prepared by different synthetic routes. Nanoscale 2018;10:1540–6.
[70] Sofer Z, Sedmidubský D, Huber Š, Luxa J, Bouša D, Boothroyd C, et al. Layered black phosphorus: strongly anisotropic magnetic, electronic, and electron-transfer properties. Angew Chem Int Ed 2016;55:3382–6.
[71] Zhang D, Liu HM, Shu X, Feng J, Yang P, Dong P, et al. Nanocopper-loaded black phosphorus nanocomposites for efficient synergistic antibacterial application. J Hazard Mater 2020;393:122317.
[72] Tan L, Li J, Liu X, Cui Z, Yang X, Yeung KWK, et al. *In situ* disinfection through photoinspired radical oxygen species storage and thermal-triggered release from black phosphorous with strengthened chemical stability. Small 2018;14:1703197.
[73] Qu G, Xia T, Zhou W, Zhang X, Zhang H, Hu L, et al. Property-activity relationship of black phosphorus at the nano-bio interface: from molecules to organisms. Chem Rev 2020;120:2288–346.
[74] Sofer Z, Sedmidubský D, Luxa J, Bouša D, Huber Š, Lazar P, et al. Universal method for large scale synthesis of layered transition metal dichalcogenides. Chem-Eur J 2017;23:10177–86.
[75] Han GH, Duong DL, Keum DH, Yun SJ, Lee YH. Van der waals metallic transition metal dichalcogenides. Chem Rev 2018;118:6297–336.
[76] Wei F, Cui X, Wang Z, Dong C, Li J, Han X. Recoverable peroxidase-like Fe_3O_4@MoS_2-Ag nanozyme with enhanced antibacterial ability. Chem Eng J 2021;408:127240.
[77] Tian X, Sun Y, Fan S, Boudreau MD, Chen C, Ge C, et al. Photogenerated charge carriers in molybdenum disulfide quantum dots with enhanced antibacterial activity. ACS Appl Mater Interfaces 2019;11:4858–66.
[78] Di J, Xia J, Ji M, Li H, Xu H, Li H, et al. The synergistic role of carbon quantum dots for the improved photocatalytic performances of Bi_2MoO_6. Nanoscale 2015;7:11433–43.
[79] Xiong J, Song P, Di J, Li H, Liu Z. Freestanding ultrathin bismuth-based materials for diversified photocatalytic applications. J Mater Chem A 2019;7:25203–26.
[80] Huo WC, Dong X, Li JY, Liu M, Liu XY, Zhang YX, et al. Synthesis of Bi_2WO_6 with gradient oxygen vacancies for highly photocatalytic NO oxidation and mechanism study. Chem Eng J 2018;361:129–38.
[81] Han X, Zhang Y, Wang S, Huang H. Controllable synthesis, characterization and photocatalytic performance of four kinds of bismuth-based materials. Colloids Surf A 2019;568:419–28.
[82] Jia Y, Zhan S, Ma S, Zhou Q. Fabrication of TiO_2-Bi_2WO_6 binanosheet for enhanced solar photocatalytic disinfection of *E. coli*: insights on the mechanism. ACS Appl Mater Interfaces 2016;8:6841-51.
[83] Lee KH, Shin HJ, Lee J, Lee IY, Kim GH, Choi JY, et al. Large-scale synthesis of high-quality hexagonal boron nitride nanosheets for large-area graphene electronics. Nano Lett 2012;12:714–8.
[84] Gao G, Mathkar A, Martins EP, Galvão DS, Gao D, Da Silva Autreto PA, et al. Designing nanoscaled hybrids from atomic layered boron nitride with silver nanoparticle deposition. J Mater Chem A 2014;2:3148–54.
[85] Merenkov IS, Myshenkov MS, Zhukov YM, Sato Y, Frolova TS, Danilov DV, et al. Orientation-controlled, low-temperature plasma growth and applications of h-BN nanosheets. Nano Res 2019;12:91–9.
[86] Kirby AE, Garner K, Levin BR. The relative contributions of physical structure and cell density to the antibiotic susceptibility of bacteria in biofilms. Antimicrob Agents Chemother 2012;56:2967–75.
[87] Cucarella C, Solano C, Valle J, Amorena B, Lasa Í, Penadés JR. Bap, a *Staphylococcus aureus* surface protein involved in biofilm formation. J Bacteriol 2001;183:2888–96.

[88] Karahan HE, Wang Y, Li W, Liu F, Wang L, Sui X, et al. Antimicrobial graphene materials:the interplay of complex material characteristics and competing mechanisms. Biomater Sci 2018;6:766–73.
[89] Lin N, Berton P, Moraes C, Rogers RD, Tufenkji N. Nanodarts, nanoblades, and nanospikes: mechano-bactericidal nanostructures and where to find them. Adv Colloid Interface Sci 2018;252:55–68.
[90] Liu S, Zeng TH, Hofmann M, Burcombe E, Wei J, Jiang R, et al. Antibacterial activity of graphite, graphite oxide, graphene oxide, and reduced graphene oxide: membrane and oxidative stress. ACS Nano 2011;5:6971–80.
[91] Lu X, Feng X, Werber JR, Chu C, Zucker I, Kim JH, et al. Enhanced antibacterial activity through the controlled alignment of graphene oxide nanosheets. Proc Natl Acad Sci U S A 2017;114:E9793–801.
[92] Akhavan O, Ghaderi E. Toxicity of graphene and graphene oxide nanowalls against bacteria. ACS Nano 2010;4:5731–6.
[93] Wei W, Li J, Liu Z, Deng Y, Chen D, Gu P, et al. Distinct antibacterial activity of vertically aligned grapheme coating against gram-positive and gram-negative bacteria. J Mater Chem B 2020;8:6069–79.
[94] Cui H, Gu Z, Chen X, Lin L, Wang Z, Dai X, et al. Stimulating antibacterial activities of graphitic carbon nitride nanosheets with plasma treatment. Nanoscale 2019;11:18416–25.
[95] Tu Y, Lv M, Xiu P, Huynh T, Zhang M, Castelli M, et al. Destructive extraction of phospholipids from *Escherichia coli* membranes by grapheme nanosheets. Nat Nanotechnol 2013;8:594–601.
[96] Ji DK, Zhang Y, Zang Y, Li J, Chen GR, He XP, et al. Targeted intracellular production of reactive oxygen species by a 2D molybdenum disulfide glycosheet. Adv Mater 2016;28:9356–63.
[97] Yang X, Li J, Liang T, Ma C, Zhang Y, Chen H, et al. Antibacterial activity of two-dimensional MoS_2 sheets. Nanoscale 2014;6:10126–33.
[98] Karunakaran S, Pandit S, Basu B, De M. Simultaneous exfoliation and functionalization of 2H-MoS_2 by thiolated surfactants: applications in enhanced antibacterial activity. J Am Chem Soc 2018;140:12634–44.
[99] Shi L, Chen J, Teng L, Wang L, Zhu G, Liu S, et al. The antibacterial applications of graphene and its derivatives. Small 2016;12:4165–84.
[100] Navale GR, Rout CS, Gohil KN, Dharne MS, Late DJ, Shinde SS. Oxidative and membrane stress-mediated antibacterial activity of WS_2 and rGO-WS_2 nanosheets. RSC Adv 2015;5:74726–33.
[101] Gurunathan S, Han JW, Dayem AA, Eppakayala V, Kim JH. Oxidative stress-mediated antibacterial activity of graphene oxide and reduced graphene oxide in *Pseudomonas aeruginosa*. Int J Nanomed 2012;7:5901–14.
[102] Xiong Z, Zhang X, Zhang S, Lei L, Ma W, Li D, et al. Bacterial toxicity of exfoliated black phosphorus nanosheets. Ecotoxicol Environ Saf 2018;161:507–14.
[103] Pandit S, Karunakaran BSK, Basu B, De M. High antibacterial activity of functionalized chemically exfoliated MoS_2. ACS Appl Mater Interfaces 2016;8:31567–73.
[104] Cui F, Li T, Wang D, Yi S, Li J, Li X. Recent advances in carbon-based nanomaterials for combating bacterial biofilm-associated infections. J Hazard Mater 2022;431:128597.
[105] Kim TI, Kwon B, Yoon J, Park I, Bang GS, Park Y, et al. Antibacterial activities of graphene oxide molybdenum disulfide nanocomposite films. ACS Appl Mater Interfaces 2017;9:7908–17.
[106] Rasool K, Helal M, Ali A, Ren CE, Gogotsi Y, Mahmoud KA. Antibacterial activity of $Ti_3C_2T_x$ MXene. ACS Nano 2016;10:3674–84.
[107] Hu J, Tang YA, Elmenoufy AH, Xu H, Cheng Z, Yang X. Nanocomposite-based photodynamic therapy strategies for deep tumor treatment. Small 2015;11:5860–87.
[108] Ristic BZ, Milenkovic MM, Dakic IR, Todorovic-Markovic BM, Milosavljevic MS, Budimir MD, et al. Photodynamic antibacterial effect of graphene quantum dots. Biomaterials 2014;35:4428–35.
[109] Shanmugam V, Selvakumar S, Yeh CS. Near-infrared light-responsive nanomaterials in cancer therapeutics. Chem Soc Rev 2014;43:6254–87.
[110] Tavares A, Carvalho C, Faustino MA, Neves MG, Tomé JPC, Tomé AC, et al. Antimicrobial photodynamic therapy: study of bacterial recovery viability and potential development of resistance after treatment. Mar Drugs 2010;8:91–105.
[111] Hu X, Zhou M, Zhou Q. Ambient water and visible-light irradiation drive changes in graphene morphology, structure, surface chemistry, aggregation, and toxicity. Environ Sci Technol 2015;49:3410–8.
[112] Li X, Shan J, Zhang W, Su S, Yuwen L, Wang L. Recent advances in synthesis and biomedical applications of two-dimensional transition metal dichalcogenide nanosheets. Small 2017;13:1602660.
[113] Chong Y, Ge C, Fang G, Wu R, Zhang H, Chai Z, et al. Light-enhanced antibacterial activity of graphene oxide mainly *via* accelerated electron transfer. Environ Sci Technol 2017;51:10154–61.
[114] Li J, Wang G, Zhu H, Zhang M, Zheng X, Di Z, et al. Antibacterial activity of large-area monolayer graphene film manipulated by charge transfer. Sci Rep 2014;4:4359.
[115] Huang J, Ho W, Wang X. Metal-free disinfection effects induced by graphitic carbon nitride polymers under visible light illumination. Chem Commun 2014;50:4338–40.
[116] Niu P, Zhang L, Liu G, Cheng HM. Graphene-like carbon nitride nanosheets for improved photocatalytic activities. Adv Funct Mater 2012;22:4763–70.
[117] Li J, Yu Y, Zhang L. Bismuth oxyhalide nanomaterials: layered structures meet photocatalysis. Nanoscale 2014;6:8473–88.
[118] Zhou Y, Zhang Y, Lin M, Long J, Zhang Z, Lin H, et al. Monolayered Bi_2WO_6 nanosheets mimicking heterojunction interface with open surfaces for photocatalysis. Nat Commun 2015;6:8340.
[119] Kang S, Huang W, Zhang L, He M, Xu S, Sun D, et al. Moderate bacterial etching allows scalable and clean delamination of g-C_3N_4 with enriched unpaired electrons for highly improved photocatalytic water disinfection. ACS Appl Mater Interfaces 2018;10:13796–804.
[120] Wang Y, Jiang W, Luo W, Chen X, Zhu Y. Ultrathin nanosheets g-C_3N_4@Bi_2WO_6 core-shell structure *via* low temperature reassembled strategy to promote photocatalytic activity. Appl Catal B 2018;237:633–40.
[121] Zhao H, Yu H, Quan X, Chen S, Zhang Y, Zhao H, et al. Fabrication of atomic single layer graphitic-C_3N_4 and its high performance of photocatalytic disinfection under visible light irradiation. Appl Catal B 2014;152–153:46–50.
[122] Liu H, Li Y, Xiang M, Zeng H, Shao X. Single layered MoS_2 directly grown on rutile TiO_2 (110) for enhanced interfacial charge transfer. ACS Nano 2019;13:6083–9.
[123] Liu C, Kong D, Hsu PC, Yuan H, Lee HW, Liu Y, et al. Rapid water disinfection using vertically aligned MoS_2 nanofilms and visible light. Nat Nanotechnol 2016;11:1098–104.
[124] Niu J, Sun Y, Wang F, Zhao C, Ren J, Qu X. Photo-modulated nanozyme used for gram-selective antimicrobial. Chem Mater 2018;30:7027–33.
[125] Bellis SL. Advantages of RGD peptides for directing cell association with biomaterials. Biomaterials 2011;32:4205–10.
[126] Wang L, Zhang X, Yu X, Gao F, Shen Z, Zhang X, et al. An all-organic semiconductor g-C_3N_4/PDINH heterostructure with advanced antibacterial photocatalytic therapy activity. Adv Mater 2019;31:1901965.
[127] Zeng X, Liu Y, Xia Y, Uddin MH, Xia D, McCarthy DT, et al. Cooperatively modulating reactive oxygen species generation and bacteriaphotocatalyst contact over graphitic carbon nitride by polyethylenimine for rapid water disinfection. Appl Catal B 2020;274:119095.
[128] Samak NA, Selim MS, Hao Z, Xing J. Immobilized arginine/tryptophan-rich cyclic dodecapeptide on reduced graphene oxide anchored with manganese dioxide for microbial biofilm eradication. J Hazard Mater 2022;426:128035.
[129] Breloy L, Brezová V, Blacha-Grzechnik A, Presset M, Yildirim MS, Yilmaz I, et al. Visible light anthraquinone functional phthalocyanine photoinitiator for free-radical and cationic polymerizations. Macromol 2019;53:112–24.
[130] Nguyen VN, Zhao Z, Tang BZ, Yoon J. Organic photosensitizers for antimicrobial phototherapy. Chem Soc Rev 2022:D1CS00647A.
[131] Hu K, Chen C, Zhu Y, Zeng G, Huang B, Chen W, et al. Ternary Z-scheme Heterojunction of Bi_2WO_6 with Reduced Grapheme Oxide (rGO) and Meso-Tetra (4-Carboxyphenyl) Porphyrin (TCPP) for Enhanced Visible-Light Photocatalysis. J Colloid Interface Sci 2019;540:115–25.
[132] Chen D, Wang K, Hong W, Zong R, Yao W, Zhu Y. Visible light photoactivity enhancement *via* CuTCPP hybridized g-C_3N_4 nanocomposite. Appl Catal B 2015;166:366–73.

[133] Da Silva ES, Moura NM, Neves MGP, Coutinho A, Prieto M, Silva CG, et al. Novel hybrids of graphitic carbon nitride sensitized with free-base meso-tetrakis (carboxyphenyl) porphyrins for efficient visible light photocatalytic hydrogen production. Appl Catal B 2018;221:56–69.
[134] Zhang J, Wang A, Zhao W, Li C, Chen X, Wang Y, et al. Influence of metal-porphyrins on the photocatalysis of graphitic carbon nitride. Dyes Pigm 2018;153:241–7.
[135] Lu W, Xu T, Wang Y, Hu H, Li N, Jiang X, et al. Synergistic photocatalytic properties and mechanism of g-C_3N_4 coupled with zinc phthalocyanine catalyst under visible light irradiation. Appl Catal B 2016;180:20–8.
[136] Ge R, Li X, Kang SZ, Qin L, Li G. Highly efficient graphene oxide/porphyrin photocatalysts for hydrogen evolution and the interfacial electron transfer. Appl Catal B 2016;187:67–74.
[137] Hu Q, Rezaee E, Shan H, Liu P, Xu ZX. Graphene oxide/N-CuMe$_2$Pc nanorod hybrid nanocomposite as efficient visible light photocatalyst for aqueous Cr(VI) reduction. Catal Today 2018;335:180–6.
[138] Shi T, Wen Z, Ding L, Liu Q, Guo Y, Ding C, et al. Visible/near-infrared light response VOPc/carbon nitride nanocomposites: VOPc sensitizing carbon nitride to improve photo-to-current conversion efficiency for fabricating photoelectrochemical diclofenac aptasensor. Sensor Actuators B 2019;299:126834.
[139] Liang Q, Zhang M, Liu C, Xu S, Li Z. Sulfur-doped graphitic carbon nitride decorated with zinc phthalocyanines towards highly stable and efficient photocatalysis. Appl Catal A 2016;519:107–15.
[140] Zhang X, Yu L, Zhuang C, Peng T, Li R, Li X. Highly asymmetric phthalocyanine as sensitizer of graphitic carbon nitride for extremely efficient photocatalytic H_2 production under near-IR light. ACS Catal 2014;4:162–70.
[141] Sun J, Bian J, Li J, Zhang Z, Li Z, Qu Y, et al. Efficiently photocatalytic conversion of CO_2 on ultrathin metal phthalocyanine/g-C_3N_4 heterojunctions by promoting charge transfer and CO_2 activation. Appl Catal B 2020;277:119199.
[142] Liu B, Li C, Chen G, Liu B, Deng X, Wei Y, et al. Synthesis and optimization of MoS_2@Fe_3O_4-ICG/Pt(IV) nanoflowers for MR/IR/PA bioimaging and combined PTT/PDT/chemotherapy triggered by 808 nm laser. Adv Sci 2017;4:1600540.
[143] Sharker SM, Lee JE, Kim SH, Jeong JH, In I, Lee H, et al. pH triggered *in vivo* photothermal therapy and fluorescence nanoplatform of cancer based on responsive polymer-indocyanine green integrated reduced graphene oxide. Biomaterials 2015;61:229–38.
[144] Li M, Li L, Su K, Liu X, Zhang T, Liang Y, et al. Highly effective and noninvasive near-infrared eradication of a *staphylococcus aureus* biofilm on implants by a photoresponsive coating within 20 min. Adv Sci 2019;6:1900599.
[145] Zhang L, Chen P, Xu Y, Nie W, Zhou Y. Enhanced photo-induced antibacterial application of graphene oxide modified by sodium anthraquinone-2-sulfonate under visible light. Appl Catal B 2020;265:118572.
[146] Shiraishi Y, Kofuji Y, Sakamoto H, Tanaka S, Ichikawa S, Hirai T. Effects of surface defects on photocatalytic H_2O_2 production by mesoporous graphitic carbon nitride under visible light irradiation. ACS Catal 2015;5:3058–66.
[147] Guirguis A, Polaki SR, Sahoo G, Ghosh S, Kamruddin M, Merenda A, et al. Engineering high-defect densities across vertically-aligned graphene nanosheets to induce photocatalytic reactivity. Carbon 2020;168:32–41.
[148] Zhang G, Hu Z, Sun M, Liu Y, Liu L, Liu H, et al. Formation of Bi_2WO_6 bipyramids with vacancy pairs for enhanced solar-driven photoactivity. Adv Funct Mater 2015;25:3726–34.
[149] Wang J, Liang H, Zhang C, Jin B, Men Y. Bi_2WO_{6-x} nanosheets with tunable bi quantum dots and oxygen vacancies for photocatalytic selective oxidation of alcohols. Appl Catal B 2019;256:117874.
[150] Di J, Chen C, Zhu C, Ji M, Xia J, Yan C, et al. Bismuth vacancy mediated single unit cell Bi_2WO_6 nanosheets for boosting photocatalytic oxygen evolution. Appl Catal B 2018;238:119–25.
[151] Guan M, Xiao C, Zhang J, Fan S, An R, Cheng Q, et al. Vacancy associates promoting solar-driven photocatalytic activity of ultrathin bismuth oxychloride nanosheets. J Am Chem Soc 2013;135:10411–7.
[152] Dai Z, Qin F, Zhao H, Ding J, Liu Y, Chen R. Crystal defects engineering of aurivillius Bi_2MoO_6 by Ce doping for increased reactive species production in photocatalysis. ACS Catal 2016;6:3180–92.
[153] Di J, Xia J, Chisholm MF, Zhong J, Chen C, Cao X, et al. Defect-tailoring mediated electron-hole separatsion in single-unit-cell Bi_3O_4Br nanosheets for boosting photocatalytic hydrogen evolution and nitrogen fixationre under electron irradiation. Adv Mater 2019;31:1807576.
[154] Li H, Shang J, Ai Z, Zhang L. Efficient visible light nitrogen fixation with BiOBr nanosheets of oxygen vacancies on the exposed 001 facets. J Am Chem Soc 2015;137:6393–9.
[155] Ding J, Dai Z, Tian F, Zhou B, Zhao B, Zhao H, et al. Generation of $V_{Bi}V_OV_{Bi}$ defect cluster for $^1O_2$ production in molecular oxygen activation of photocatalysis. J Mater Chem A 2017;5:23453–9.
[156] Yu W, Shan X, Zhao Z. Unique nitrogen-deficient carbon nitride homojunction prepared by a facile inserting-removing strategy as an efficient photocatalyst for visible lightdriven hydrogen evolution. Appl Catal B 2020;269:118778.
[157] Kong L, Mu X, Fan X, Li R, Zhang Y, Song P, et al. Site-selected N Vacancy of g-C_3N_4 for photocatalysis and physical mechanism. Appl Mater Today 2018;13:329–38.
[158] Qi R, Yu P, Zhang J, Guo W, He Y, Hojo H, et al. Efficient visible light photocatalysis enabled by the interaction between dual cooperative defect sites. Appl Catal B 2020;274:119099.
[159] Di J, Xia J, Li X, Ji M, Xu H, Chen Z, et al. Constructing confined surface carbon defects in ultrathin graphitic carbon nitride for photocatalytic free radical manipulation. Carbon 2016;107:1–10.
[160] Lan H, Li L, An X, Liu F, Chen C, Liu H, et al. Microstructure of carbon nitride affecting synergetic photocatalytic activity: hydrogen bonds vs structural defects. Appl Catal B 2017;204:49–57.
[161] Xie Y, Li Y, Huang Z, Zhang J, Jia X, Wang X, et al. Two types of cooperative nitrogen vacancies in polymeric carbon nitride for efficient solar-driven H_2O_2 evolution. Appl Catal B 2020;265:118581.
[162] Zhang Z, Lu L, Lv Z, Chen Y, Jin H, Hou S, et al. Porous carbon nitride with defect mediated interfacial oxidation for improving visible light photocatalytic hydrogen evolution. Appl Catal B 2018;232:384–90.
[163] Komsa HP, Kurasch S, Lehtinen O, Kaiser U, Krasheninnikov AV. From point to extended defects in two-dimensional MoS_2: Evolution of atomic structure under electron irradiation. Phys Rev B 2013;88:035301.
[164] Ma Y, Hai G, Atinafu DG, Dong W, Li R, Hou C, et al. Carbon inserted defect-rich MoS_{2-x} nanosheets@CdS nanospheres for efficient photocatalytic hydrogen evolution under visible light irradiation. J Colloid Interface Sci 2020;569:89–100.
[165] Zhang Y, Kuwahara Y, Mori K, Yamashita H. Defect engineering of MoS_2 and its impacts on electrocatalytic and photocatalytic behavior in hydrogen evolution reactions. Chem-Asian J 2019;14:278–85.
[166] Sarkar D, Mondal B, Som A, Ravindran SJ, Jana SK, Manju CK, et al. Holey MoS_2 nanosheets with photocatalytic metal rich edges by ambient electrospray deposition for solar water disinfection. Global Challenges 2018;2:1800052.
[167] Xiong J, Di J, Xia J, Zhu W, Li H. Surface defect engineering in 2D nanomaterials for photocatalysis. Adv Funct Mater 2018;28:1801983.
[168] Azizi A, Wang Y, Stone G, Elias AL, Lin Z, Terrones M, et al. Mauricio terrones defect coupling and sub-angstrom structural distortions in $W_{1-x}Mo_xS_2$ monolayers. Nano Lett 2017;17:2802–8.
[169] Wu XL, Mei YF, Siu GG, Wong KL, Moulding K, Stokes MJ, et al. Spherical growth and surface-quasifree vibrations of Si nanocrystallites in Er-doped Si nanostructures. Phys Rev Lett 2001;86:3000.
[170] Mohamed MA, Zain MFM, Minggu LJ, Kassim MB, Amin NAS, Salleh WNW, et al. Constructing bio-templated 3D porous microtubular C-doped g-C_3N_4 with tunable band structure and enhanced charge carrier separation. Appl Catal B 2018;236:265–79.
[171] Wang T, Zhang X, Mei L, Ma D, Liao Y, Zu Y, et al. Two-step gas/liquid strategy for production of N-doped defect-rich transition metal dichalcogenides nanosheets and their antibacterial applications. Nanoscale 2020;12:8415–24.
[172] Xiong T, Huang H, Sun Y, Dong F. *In situ* synthesis of a C-doped $(BiO)_2CO_3$ hierarchical self-assembly effectively promoting visible lght photocatalysis. J Mater Chem A 2015;3:6118–27.

[173] Tang B, Jiang G, Wei Z, Li X, Wang X, Jiang T, et al. Preparation of N-doped Bi_2WO_6 microspheres for efficient visible light-induced photocatalysis. Acta Metall Sin 2014;27:124–30.
[174] Mateo D, García-Mulero A, Albero J, García H. N-doped defective graphene decorated by strontium titanate as efficient photocatalyst for overall water splitting. Appl Catal B 2019;252:111–9.
[175] Ke T, Shen S, Rajavel K, Yang K, Lin D. *In situ* growth of TiO_2 nanoparticles on nitrogen doped Ti_3C_2 with isopropyl amine toward enhanced photocatalytic activity. J Hazard Mater 2021;402:124066.
[176] Maimaitizi H, Abulizi A, Zhang T, Okitsu K, Zhu JJ. Facile photo-ultrasonic assisted synthesis of flower-like Pt/N-MoS_2 microsphere as an efficient sonophotocatalyst for nitrogen fixation. Ultrason Sonochem 2020;63:104956.
[177] Zhang JW, Gong S, Mahmood N, Pan L, Zhang X, Zou JJ. Oxygen-doped nanoporous carbon nitride *via* water-based homogeneous supramolecular assembly for photocatalytic hydrogen evolution. Appl Catal B 2018;221:9–16.
[178] Wang Y, Wang H, Chen F, Cao F, Zhao X, Meng S, et al. Facile synthesis of oxygen doped carbon nitride hollow microsphere for photocatalysis. Appl Catal B 2017;206:417–25.
[179] Bellardita M, García-López EI, Marcì G, Krivtsov I, García JR, Palmisano L. Selective photocatalytic oxidation of aromatic alcohols in water by using P-doped g-C_3N_4. Appl Catal B 2018;220:222–33.
[180] Zhang Y, Shi J, Huang Z, Guan X, Zong S, Cheng C, et al. Synchronous construction of CoS_2 *in-situ* loading and S doping for g-C_3N_4: enhanced photocatalytic H_2-evolution activity and mechanism insight. Chem Eng J 2020;401:126135.
[181] Feng C, Tang L, Deng Y, Zeng G, Wang J, Liu Y, et al. Enhancing optical absorption and charge transfer: synthesis of S-doped h-BN with tunable band structures for metal-free visible-light-driven photocatalysis. Appl Catal B 2019;256:117827.
[182] Alafif ZO, Anjum M, Ansari MO, Kumar R, Rashid J, Madkour M, et al. Synthesis and characterization of S-Doped-rGO/ZnS nanocomposite for the photocatalytic degradation of 2-chlorophenol and disinfection of real dairy wastewater. J Photochem Photobiol A 2019;377:190–7.
[183] Huang H, Liu K, Chen K, Zhang Y, Zhang Y, Wang S. Ce and F comodification on the crystal structure and enhanced photocatalytic activity of Bi_2WO_6 photocatalyst under visible light irradiation. J Phys Chem C 2014;118:14379–87.
[184] Khazaee Z, Khavar AHC, Mahjoub AR, Motaee A, Srivastava V, Sillanpää M. Template-confined growth of X-Bi_2MoO_6 (X:F, Cl, Br, I) nanoplates with open surfaces for photocatalytic oxidation;experimental and DFT insights of the halogen doping. Sol Energy 2020;196:567–81.
[185] Chu YC, Lin TJ, Lin YR, Chiu WL, Nguyen BS, Hu C. Influence of P, S, O-doping on g.C_3N4 for hydrogel formation and photocatalysis: an experimental and theoretical study. Carbon 2020;169:338–48.
[186] Ma S, Zhan S, Jia Y, Shi Q, Zhou Q. Enhanced disinfection application of Ag-Modified g-C_3N_4 composite under visible light. Appl Catal B 2016;186:77–87.
[187] Chernousova S, Epple M. Silver as antibacterial agent: ion, nanoparticle, and metal. Angew Chem Int Ed 2013;52:1636–53.
[188] Zhu M, Liu X, Tan L, Cui Z, Liang Y, Li Z, et al. Photo-responsive chitosan/Ag/MoS_2 for rapid bacteria-killing. J Hazard Mater 2019;383:121122.
[189] Zheng X, Liu Q, Jing C, Li Y, Li D, Luo W, et al. Catalytic gold nanoparticles for nanoplasmonic detection of DNA hybridization. Angew Chem Int Ed 2011;123:12200–4.
[190] Cai T, Wang L, Liu Y, Zhang S, Dong W, Chen H, et al. Ag_3PO_4/Ti_3C_2 MXene interface materials as a schottky catalyst with enhanced photocatalytic activities and anti-photocorrosion performance. Appl Catal B 2018;239:545–54.
[191] Zhang M, Li X, Fan S, Zeng L, Yin Z, Lian T, et al. Highly oriented SnS_2/RGO/Ag heterostructures for boosting photoeletrochemical and photocatalytic performances *via* schottky and RGO-n dual-heterojunctions interfacial effects. Appl Catal A 2018;563:118–26.
[192] Han N, Wang W, Lv X, Zhang W, Yang C, Wang M, et al. Highly efficient purification of multicomponent wastewater by electrospinning kidney-bean-skin-like porous H-PPAN/rGO–g–PAO@Ag^+/Ag composite nanofibrous membranes. ACS Appl Mater Interfaces 2019;11:46920–9.
[193] Zhao M, Chen P. Exploring plasmonic photocatalysis *via* single-molecule reaction imaging. Nano Lett 2020;20:2939–40.
[194] Linic S, Christopher P, Ingram DB. Plasmonic-metal nanostructures for efficient conversion of solar to chemical energy. Nat Mater 2011;10:911–21.
[195] Vidyasagar D, Ghugal SG, Kulkarni A, Mishra P, Shende AG, Jagannath, et al. Silver/Silver(II) Oxide (Ag/AgO) Loaded Graphitic Carbon Nitride Microspheres: An Effective Visible Light Active Photocatalyst for Degradation of Acidic Dyes and Bacterial Inactivation. Appl Catal B 2017;221:339-48.
[196] Xie X, Mao C, Liu X, Zhang Y, Cui Z, Yang X, et al. Synergistic bacteria killing through photodynamic and physical actions of graphene oxide/Ag/collagen coating. ACS Appl Mater Interfaces 2017;9:26417–28.
[197] Zhang Z, Huang J, Fang Y, Zhang M, Liu K, Dong B. A nonmetal plasmonic Z-scheme photocatalyst with UV- to NIR-driven photocatalytic protons reduction. Adv Mater 2017;29:1606688.
[198] He Z, Kim C, Lin L, Jeon TH, Lin S, Wang X, et al. Formation of heterostructures *via* direct growth CN on *h*-BN porous nanosheets for metal-free photocatalysis. Nano Energy 2017;42:58–68.
[199] Xu H, Liu L, Song Y, Huang L, Li Y, Chen Z, et al. BN nanosheets modified WO_3 photocatalysts for enhancing photocatalytic properties under visible light irradiation. J Alloys Compd 2016;660:48–54.
[200] Cai H, Wang B, Xiong L, Bi J, Yuan L, Yang G, et al. Orienting the charge transfer path of type-ii heterojunction for photocatalytic hydrogen evolution. Appl Catal B 2019;256:117853.
[201] Ong WJ, Putri LK, Tan LL, Chai SP, Yong ST. Heterostructured AgX/g-C_3N_4 (X=Cl and Br) nanocomposites *via* a sonication-assisted deposition-precipitation approach: emerging role of halide ions in the synergistic photocatalytic reduction of carbon dioxide. Appl Catal B 2016;180:530–43.
[202] Wang Q, Xu P, Zhang G, Hu L, Wang P. Visible-light responsive g-C_3N_4 coupled with ZnS nanoparticles *via* a rapid microwave route: characterization and enhanced photocatalytic activity. Appl Surf Sci 2019;488:360–9.
[203] Li J, Yin Y, Liu E, Ma Y, Wan J, Fan J, et al. *In situ* growing Bi_2MoO_6 on g-C_3N_4 nanosheets with enhanced photocatalytic hydrogen evolution and disinfection of bacteria under visible light irradiation. J Hazard Mater 2017;321:183–92.
[204] Guo L, Zhang K, Han X, Zhao Q, Zhang Y, Qi M, et al. 2D/2D type-II Cu_2ZnSnS_4/Bi_2WO_6 heterojunctions to promote visible-light-driven photo-fenton catalytic activity. Chin J Catal 2020;41:503–13.
[205] Lu B, Zeng S, Li C, Wang Y, Pan X, Zhang L, et al. Nanoscale P-N heterojunctions of BiOI/nitrogen-doped reduced graphene oxide as a high performance photocatalyst. Carbon 2018;132:191–8.
[206] Guo F, Shi W, Wang H, Huang H, Liu Y, Kang Z. Fabrication of $CuBi_2O_4$/g-C_3N_4 P-N heterojunction with enhanced visible light photocatalytic efficiency toward tetracycline degradation. Inorg Chem Front 2017;4:1714–20.
[207] Xie T, Liu Y, Wang H, Wu Z. Layered $MoSe_2/Bi_2WO_6$ composite with P-N heterojunctions as a promising visible-light induced photocatalyst. Appl Surf Sci 2018;444:320–9.
[208] Lu H, Xu L, Wei B, Zhang M, Gao H, Sun W. Enhanced photosensitization process induced by the P-N junction of $Bi_2O_2CO_3$/BiOCl heterojunctions on the degradation of rhodamine B. Appl Surf Sci 2014;303:360–6.
[209] Shi H, Fan J, Zhao Y, Hu X, Zhang X, Tang Z. Visible Light Driven $CuBi_2O_4/Bi_2MoO_6$ P-N Heterojunction with Enhanced Photocatalytic Inactivation of *E. coli* and Mechanism Insight. J Hazard Mater 2020;381:121006.
[210] Yang X, Xiang Y, Qu Y, Ding X, Chen H. Novel *in situ* fabrication of conjugated microporous poly(benzothiadiazole)-Bi_2MoO_6 Z-scheme heterojunction with enhanced visible light photocatalytic activity. J Catal 2017;345:319–28.
[211] Yan J, Wu H, Chen H, Zhang Y, Zhang F, Liu SF. Fabrication of TiO_2/C_3N_4 heterostructure for enhanced photocatalytic Z-scheme overall water splitting. Appl Catal B 2016;191:130–7.
[212] Zeng X, Wang Z, Wang G, Gengenbach TR, McCarthy DT, Deletic A, et al. Highly dispersed TiO_2 nanocrystals and WO_3 nanorods on reduced graphene oxide: Z-scheme photocatalysis system for accelerated photocatalytic water disinfection. Appl Catal B 2017;218:163–73.
[213] Guo M, Xing Z, Zhao T, Li Z, Yang S, Zhou W. WS_2 quantum Dots/MoS_2@WO_{3-x} Core-Shell hierarchical dual Z-scheme tandem heterojunctions with wide-spectrum response and enhanced photocatalytic performance. Appl Catal B 2019;257:117913.
[214] Hu J, Chen D, Mo Z, Li N, Xu Q, Li H, et al. Z-scheme 2D/2D heterojunction of black phosphorus/monolayer Bi_2WO_6 nanosheets with enhanced photocatalytic activities. Angew Chem Int Ed 2018;58:2073–7.

[215] Li H, Hu T, Zhang R, Liu J, Hou W. Preparation of solid-state Z-scheme Bi_2MoO_6/MO (M=Cu, C_{o3}/4, orNi) heterojunctions with internal electric field-improved performance in photocatalysis. Appl Catal B 2016;188:313–23.
[216] Jia X, Han Q, Liu H, Li S, Bi H. A dual strategy to construct flowerlike s-scheme BiOBr/BiOAc1−xBrx heterojunction with enhanced visible-light photocatalytic activity. Chem Eng J 2020;399:125701.
[217] Qin D, Xia Y, Li Q, Yang C, Qin Y, Lv K. One-pot calcination synthesis of $Cd_{0.5}Zn_{0.5}S$/g-C_3N_4 photocatalyst with a step-scheme heterojunction structure. J Mater Sci Technol 2020;56:206–15.
[218] Sayama K, Mukasa K, Abe R, Abe Y, Arakawa H. Stoichiometric water splitting into H_2 and O_2 using a mixture of two different photocatalysts and an IO_3^-/I^- shuttle redox mediator under visible light irradiation. Chem Commun 2001;23:2416–7.
[219] Zhou P, Yu J, Jaroniec M. All-solid-state Z-scheme photocatalytic systems. Adv Mater 2014;26:4920–35.
[220] Xu Q, Zhang L, Yu J, Wageh S, Al-Ghamdi AA, Jaroniec M. Direct Z-scheme photocatalysts: principles, synthesis, and applications. Mater Today 2018;21:1042–63.
[221] Sasaki Y, Iwase A, Kato H, Kudo A. The effect of co-catalyst for Z-scheme photocatalysis systems with an Fe^{3+}/Fe^{2+} electron mediator on overall water splitting under visible light irradiation. J Catal 2008;259:133–7.
[222] Lan Y, Li Z, Li D, Xie W, Yan G, Guo S. Visible-light responsive Z-scheme Bi@β-Bi_2O_3/g-C_3N_4 heterojunction for efficient photocatalytic degradation of 2,3-dihydroxynaphthalene. Chem Eng J 2020;392:123686.
[223] Feng S, Chen T, Liu Z, Shi J, Yue X, Li Y. Z-scheme CdS/CQDs/g-C_3N_4 composites with visible-near-infrared light response for efficient photocatalytic organic pollutant degradation. Sci Total Environ 2020;704:135404.
[224] Liu X, Zhang Q, Ma D. Advances in 2D/2D Z-scheme heterojunctions for photocatalytic applications. Solar RRL 2021;5:2000397.
[225] Wu Y, Wang H, Sun Y, Xiao T, Tu W, Yuan X, et al. Photogenerated charge transfer *via* interfacial internal electric field for significantly improved photocatalysis in direct Z-scheme oxygen-doped carbon nitrogen/CoAl-layered double hydroxide heterojunction. Appl Catal B 2018;227:530–40.
[226] Wu B, Li Y, Su K, Tan L, Liu X, Cui Z, et al. The enhanced photocatalytic properties of MnO_2/g-C_3N_4 heterostructure for rapid sterilization under visible light. J Hazard Mater 2019;377:227–36.
[227] Xia P, Cao S, Zhu B, Liu M, Shi M, Yu J, et al. Designing 0D/2D S-scheme heterojunction over polymeric carbon nitride for visible-light photocatalytic inactivation of bacteria. Angew Chem Int Ed 2020;59:5218–25.
[228] Xu JW, Yao K, Xu ZK. Nanomaterials with photothermal effect for antibacterial activities: an overview. Nanoscale 2019;11:8680–91.
[229] Li J, Liu X, Tan L, Cui Z, Yang X, Liang Y, et al. Zinc-doped prussian blue enhances photothermal clearance of *staphylococcus aureus* and promotes tissue repair in infected wounds. Nat Commun 2019;10:4490.
[230] Li J, Liu X, Zhou Z, Tan L, Wang X, Zheng Y, et al. Lysozyme-assisted photothermal eradication of methicillin-resistant *Staphylococcus aureus* infection and accelerated tissue repair with natural melanosome nanostructures. ACS Nano 2019;13:11153–67.
[231] Zhang Q, Liu X, Tan L, Cui Z, Li Z, Liang Y, et al. An UV to NIR-driven platform based on red phosphorus/graphene oxide film for rapid microbial inactivation. Chem Eng J 2020;383:123088.
[232] Liu S, Pan X, Liu H. Two-dimensional nanomaterials for photothermal therapy. Angew Chem Int Ed 2020;132:5943–53.
[233] Liu G, Zou J, Tang Q, Yang X, Zhang Y, Zhang Q, et al. Surface modified Ti_3C_2 MXene nanosheets for tumor targeting photothermal/photodynamic/chemo synergistic therapy. ACS Appl Mater Interfaces 2017;9:40077–86.
[234] Zhang W, Guo Z, Huang D, Liu Z, Guo X, Zhong H. Synergistic effect of chemo-photothermal therapy using PEGylated grapheme oxide. Biomaterials 2011;32:8555–61.
[235] Chou SS, Kaehr B, Kim J, Foley BM, De M, Hopkins PE, et al. Chemically exfoliated MoS_2 as near-infrared photothermal agents. Angew Chem Int Ed 2013;52:4160–4.
[236] Shi J, Li J, Wang Y, Cheng J, Zhang CY. Recent advances in MoS_2-based photothermal therapy for cancer and infectious diseases treatment. J Mater Chem B 2020;8:5793–807.
[237] Li D, Zhao Q, Zhang S, Wu F, Yu X, Xiong Z, et al. Filtration-based water treatment system embedded with black phosphorus for NIR-triggered disinfection. Environ Sci: Nano 2019;6:2977–85.
[238] Feng L, Yang D, Gai S, He F, Yang G, Yang P, et al. Single bismuth tungstate nanosheets for simultaneous chemo-, photothermal, and photodynamic therapies mediated by near-infrared light. Chem Eng J 2018;351:1147–58.
[239] Shahzad F, Alhabeb M, Hatter CB, Anasori B, Hong SM, Koo CM, et al. Electromagnetic interference shielding with 2D transition metal carbides (MXenes). Science 2016;353:1137–40.
[240] Cheng Y, Chang Y, Feng Y, Jian H, Tang Z, Zhang H. Deep-level defect enhanced photothermal performance of bismuth sulfide-gold heterojunction nanorods for photothermal therapy of cancer guided by computed tomography imaging. Angew Chem Int Ed 2018;57:246–51.
[241] Wang M, Deng K, Lü W, Deng X, Li K, Shi Y, et al. Rational design of multifunctional Fe@γ-Fe_2O_3@$HTiO_2$ nanocomposites with enhanced magnetic and photoconversion effects for wide applications: from photocatalysis to imaging-guided photothermal cancer therapy. Adv Mater 2018;30:1706747.
[242] Zhang P, Liao Q, Zhang T, Cheng H, Huang Y, Yang C, et al. High throughput of clean water excluding ions, organic media, and bacteria from defect abundant graphene aerogel under sunlight. Nano Energy 2018;46:415–22.
[243] Deng X, Li K, Cai X, Liu B, Wei Y, Deng K, et al. A hollow-structured CuS@Cu_2S@Au nanohybrid: synergistically enhanced photothermal efficiency and photoswitchable targeting effect for cancer theranostics. Adv Mater 2017;29:1701266.
[244] Wang J, Li Y, Deng L, Wei N, Weng Y, Dong S, et al. High-performance photothermal conversion of narrow-bandgap Ti_2O_3 nanoparticles. Adv Mater 2017;29:1603730.
[245] Fan X, Liu L, Jin X, Wang W, Zhang S, Tang B. MXene $Ti_3C_2T_x$ for phase change composite with superior photothermal storage capability. J Mater Chem A 2019;7:14319–27.
[246] Perreault F, De Faria AF, Nejati S, Elimelech M. Antimicrobial properties of graphene oxide nanosheets: why size matters. ACS Nano 2015;9:7226–36.
[247] Chen Y, Wu X, Chen T, Yang G. Hot carriers and photothermal effects of monolayer MoO_x for promoting sulfite oxidase mimetic activity. ACS Appl Mater Interfaces 2020;12:19357–68.
[248] Yang MQ, Shen L, Lu Y, Chee SW, Lu X, Chi X, et al. Disorder engineering in monolayer nanosheets enabling photothermic catalysis for full solar spectrum (250–2500 nm) harvesting. Angew Chem Int Ed 2019;58:3077–81.
[249] Wang YW, Fu YY, Wu LJ, Li J, Yang HH, Chen GN. Targeted photothermal ablation of pathogenic bacterium, *Staphylococcus aureus*, with nanoscale reduced graphene oxide. J Mater Chem B 2013;1:2496–501.
[250] Xuan J, Wang Z, Chen Y, Liang D, Cheng L, Yang X, et al. Organic-base-driven intercalation and delamination for the production of functionalized titanium carbide nanosheets with superior photothermal therapeutic performance. Angew Chem Int Ed 2016;128:14789–94.
[251] Jin Z, Chen D, Zhao P, Wen Y, Fan M, Zhou G, et al. Coordination-induced exfoliation to monolayer Bi-anchored MnB_2 nanosheets for multimodal imaging-guided photothermal therapy of cancer. Theranostics 2020;10:1861–72.
[252] Yin W, Yu J, Lv F, Yan L, Zheng LR, Gu Z, et al. Functionalized nano-MoS_2 with peroxidase catalytic and near-infrared photothermal activities for safe and synergetic wound antibacterial applications. ACS Nano 2016;10:11000–11.
[253] Ghim D, Jiang Q, Cao S, Singamaneni S, Jun YS. Mechanically interlocked 1T/2H phases of MoS_2 nanosheets for solar thermal water purification. Nano Energy 2018;53:949–57.
[254] Ito Y, Tanabe Y, Han J, Fujita T, Tanigaki K, Chen M. Multifunctional porous graphene for high-efficiency steam generation by heat localization. Adv Mater 2015;27:4302–7.
[255] Li H, Gong M, Xiao J, Hai L, Luo Y, He L, et al. Photothermally activated multifunctional MoS_2 bactericidal nanoplatform for combined chemo/photothermal/photodynamic triple-mode therapy of bacterial and biofilm infections. Chem Eng J 2022;429:132600.
[256] Ahn W, Vurgaftman I, Pietron JJ, Pehrsson PE, Simpkins BS. Energy-tunable photocatalysis by hot carriers generated by surface plasmon polaritons. J Mater Chem A 2019;7:7015–24.

[257] Yang H, He LQ, Hu YW, Lu X, Li GR, Liu B, et al. Quantitative detection of photothermal and photoelectrocatalytic effects induced by SPR from Au@Pt nanoparticles. Angew Chem Int Ed 2015;54:11462–6.
[258] Ji M, Xu M, Zhang W, Yang Z, Huang L, Liu J, et al. Structurally well-defined Au@$Cu_{2-x}S$ Core-Shell nanocrystals for improved cancer treatment based on enhanced photothermal efficiency. Adv Mater 2016;28:3094–101.
[259] Geng B, Qin H, Shen W, Li P, Fang F, Li X, et al. Carbon dot/WS_2 heterojunctions for NIR-II enhanced photothermal therapy of osteosarcoma and bone regeneration. Chem Eng J 2020;383:123102.
[260] Geng B, Qin H, Zheng F, Shen W, Li P, Wu K, et al. Carbon dot-sensitized MoS_2 nanosheet heterojunctions as highly efficient NIR photothermal agents for complete tumor ablation at ultralow laser exposure. Nanoscale 2019;11:7209–20.
[261] Geng B, Shen W, Li P, Fang F, Qin H, Li XK, et al. Carbon dot-passivated black phosphorus nanosheet hybrids for synergistic cancer therapy in the NIR-II window. ACS Appl Mater Interfaces 2019;11:44949–60.
[262] Hu K, Xie L, Zhang Y, Hanyu M, Yang Z, Nagatsu K, et al. Marriage of black phosphorus and Cu^{2+} as effective photothermal agents for PET-guided combination cancer therapy. Nat Commun 2020;11:2778.
[263] Liu X, Li X, Shan Y, Yin Y, Liu C, Lin Z, et al. CuS nanoparticles anchored to g-C_3N_4 nanosheets for photothermal ablation of bacteria. RSC Adv 2020;10:12183–91.
[264] Tian J, Chen L, Qiao R, Xiong K, Zhang W, Mao Y, et al. Photothermal-assist enhanced high-performance self-powered photodetector with bioinspired temperature-autoregulation by passive radiative balance. Nano Energy 2021;79:105435.
[265] Hu SH, Chen YW, Hung WT, Chen IW, Chen SY. Quantum-dot-tagged reduced graphene oxide nanocomposites for bright fluorescence bioimaging and photothermal therapy monitored *in situ*. Adv Mater 2012;24:1748–54.
[266] Feng Y, Chen Q, Yin Q, Pan G, Tu Z, Liu L. Reduced graphene oxide functionalized with gold nanostar nanocomposites for synergistically killing bacteria through intrinsic antimicrobial activity and photothermal ablation. ACS Appl Bio Mater 2019;2:747–56.
[267] Luo J, Deng W, Yang F, Wu Z, Huang M, Gu M. Gold nanoparticles decorated graphene oxide/nanocellulose paper for NIR laser-induced photothermal ablation of pathogenic bacteria. Carbohydr Polym 2018;198:206–14.
[268] Li S, Zhang Y, Wen W, Sheng W, Wang J, Wang S, et al. A high-sensitivity thermal analysis immunochromatographic sensor based on au nanoparticle-enhanced two-dimensional black phosphorus photothermal-sensing materials. Biosens Bioelectron 2019;133:223–9.
[269] Chen Y, Wu W, Xu Z, Jiang C, Han S, Ruan J, et al. Photothermal-assisted antibacterial application of graphene oxide-Ag nanocomposites against clinically isolated multi-drug resistant *Escherichia coli*. R Soc Open Sci 2020;7:192019.
[270] Ouyang J, Liu RY, Chen W, Liu Z, Xu Q, Zeng K, et al. Black phosphorus based synergistic antibacterial platform against drug resistant bacteria. J Mater Chem B 2018;6:6302–10.
[271] Wang X, Su K, Tan L, Liu X, Cui Z, Jing D, et al. Rapid and highly effective noninvasive disinfection by hybrid Ag/CS@MnO_2 nanosheets using near-infrared light. ACS Appl Mater Interfaces 2019;11:15014–27.
[272] Liang W, Wang D, Ren X, Ge C, Wang H, Li Z, et al. Facile sonochemical-assisted synthesis of orthorhombic phase black phosphorus/rGO hybrids for effective photothermal therapy. Nanophotonics 2020;9:3023–34.
[273] Chen Y, Wu Y, Sun B, Liu S, Liu H. Two-dimensional nanomaterials for cancer nanotheranostics. Small 2017;13:1603446.
[274] Gao G, Jiang YW, Guo Y, Jia HR, Cheng X, Deng Y, et al. Enzyme-mediated tumor starvation and phototherapy enhance mild-temperature photothermal therapy. Adv Funct Mater 2020;30:1909391.
[275] Chen L, Bai H, Xu JF, Wang S, Zhang X. Supramolecular porphyrin photosensitizers: controllable disguise and photoinduced activation of antibacterial behavior. ACS Appl Mater Interfaces 2017;9:13950–7.
[276] Wang W, Li G, Xia D, An T, Zhao H, Wong PK. Photocatalytic nanomaterials for solar-driven bacterial inactivation: recent progress and challenges. Environ Sci Nano 2017;4:782–99.
[277] Yuan Z, Lin C, He Y, Tao B, Chen M, Zhang J, et al. Near infrared light triggered nitric oxide-enhanced photodynamic therapy and low-temperature photothermal therapy for biofilm elimination. ACS Nano 2020;14:3546–62.
[278] Yoo D, Jeong H, Noh SH, Lee JH, Cheon J. Magnetically triggered dual functional nanoparticles for resistance free apoptotic hyperthermia. Angew Chem Int Ed 2013;125:13285–9.
[279] Li M, Liu X, Tan L, Cui Z, Yang X, Li Z, et al. Noninvasive rapid bacteria-killing and acceleration of wound healing through photothermal/photodynamic/copper ions synergistic action of a hybrid hydrogel. Biomater Sci 2018;6:2110–21.
[280] Zhang Y, Fu H, Liu DE, An J, Gao H. Construction of biocompatible bovine serum albumin nanoparticles composed of nano graphene oxide and AIEgen for dual-mode phototherapy bacteriostatic and bacterial tracking. J Nanobiotechnol 2019;17:104.
[281] Li Y, Liu X, Tan L, Cui Z, Yang X, Zheng Y, et al. Rapid sterilization and accelerated wound healing using Zn^{2+} and graphene oxide modified g-C_3N_4 under dual light irradiation. Adv Funct Mater 2018;28:1800299.
[282] Xiang Y, Zhou Q, Li Z, Cui Z, Liu X, Liang Y, et al. A Z-scheme heterojunction of ZnO/CDots/C_3N_4 for strengthened photoresponsive bacteria-killing and acceleration of wound healing. J Mater Sci Technol 2020;57:1–11.
[283] Yin Q, Tan L, Lang Q, Ke X, Bai L, Guo K, et al. Plasmonic molybdenum oxide nanosheets supported silver nanocubes for enhanced near-infrared antibacterial activity: synergism of photothermal effect, silver release and photocatalytic reactions. Appl Catal B 2018;224:671–80.
[284] Yuan Z, Tao B, He Y, Liu J, Lin C, Shen X, et al. Biocompatible MoS_2/PDA-RGD coating on titanium implant with antibacterial property *via* intrinsic ROS-independent oxidative stress and NIR irradiation. Biomaterials 2019;217:119290.
[285] Feng Z, Liu X, Tan L, Cui Z, Yang X, Li Z, et al. Electrophoretic deposited stable chitosan@MoS_2 coating with rapid *in situ* bacteria-killing ability under dual-light irradiation. Small 2018;14:1704347.
[286] Lin Y, Han D, Li Y, Tan L, Liu X, Cui Z, et al. Ag_2S@WS_2 heterostructure for rapid bacteria-killing using near-infrared light. ACS Sustainable Chem Eng 2019;7:14982–90.
[287] Li B, Tan L, Liu X, Li Z, Cui Z, Liang Y, et al. Superimposed surface plasma resonance effect enhanced the near-infrared photocatalytic activity of Au@Bi_2WO_6 coating for rapid bacterial killing. J Hazard Mater 2019;380:120818.
[288] Gai S, Yang G, Yang P, He F, Lin J, Jin D, et al. Recent advances in functional nanomaterials for light-triggered cancer therapy. Nano Today 2018;19:146–87.
[289] Yang Y, He P, Wang Y, Bai H, Wang S, Xu JF, et al. Supramolecular radical anions triggered by bacteria *in situ* for selective photothermal therapy. Angew Chem Int Ed 2017;129:16457–60.
[290] Korupalli C, Huang CC, Lin WC, Pan WY, Lin PY, Wan WL, et al. Acidity-triggered charge-convertible nanoparticles that can cause bacterium-specific aggregation *in situ* to enhance photothermal ablation of focal infection. Biomaterials 2017;116:1–9.
[291] Zhang M, Wang W, Cui Y, Chu X, Sun B, Zhou N, et al. Magnetofluorescent Fe_3O_4/carbon quantum dots coated single-walled carbon nanotubes as dual-modal targeted imaging and chemo/photodynamic/photothermal triple-modal therapeutic agents. Chem Eng J 2018;338:526–38.
[292] Ma G, Qi J, Cui Q, Bao X, Gao D, Xing C. Graphene oxide composite for selective recognition, capturing, photothermal killing of bacteria over mammalian cells. Polymers 2020;12:1116.
[293] Mei L, Lin C, Cao F, Yang D, Jia X, Hu S, et al. Amino-functionalized graphene oxide for the capture and photothermal inhibition of bacteria. ACS Appl Nano Mater 2019;2:2902–8.
[294] Wang H, Zhao B, Dong W, Zhong Y, Zhang X, Gong Y, et al. A dual-targeted platform based on graphene for synergistic chemophotothermal therapy against multidrug-resistant gram-negative bacteria and their biofilms. Chem Eng J 2020;393:124595.
[295] Qian W, Yan C, He D, Yu X, Yuan L, Liu M, et al. pH-triggered charge-reversible of glycol chitosan conjugated carboxyl graphene for enhancing photothermal ablation of focal infection. Acta Biomater 2018;69:256–64.
[296] Liu Y, Lin A, Liu J, Chen X, Zhu X, Gong Y, et al. Enzyme-responsive mesoporous ruthenium for combined chemo-photothermal therapy of drug-resistant bacteria. ACS Appl Mater Interfaces 2019;11:26590–606.

[297] Mangadlao JD, Wang X, McCleese C, Escamilla M, Ramamurthy G, Wang Z, et al. Prostate-specific membrane antigen targeted gold nanoparticles for theranostics of prostate cancer. ACS Nano 2018;12:3714–25.
[298] Hu XL, Chu L, Dong X, Chen GR, Tang T, Chen D, et al. Multivalent glycosheets for double light-driven therapy of multidrug-resistant bacteria on wounds. Adv Funct Mater 2019;29:1806986.
[299] Li J, Pei Q, Wang R, Zhou Y, Zhang Z, Cao Q, et al. Enhanced photocatalytic performance through magnetic field boosting carrier transport. ACS Nano 2018;12:3351–9.
[300] Yu J, Yin W, Zheng X, Tian G, Zhang X, Bao T, et al. Smart MoS_2/Fe_3O_4 nanotheranostic for magnetically targeted photothermal therapy guided by magnetic resonance/photoacoustic imaging. Theranostics 2015;5:931–45.
[301] Jia X, Ahmad I, Yang R, Wang C. Versatile graphene-based photothermal nanocomposites for effectively capturing and killing bacteria, and for destroying bacterial biofilms. J Mater Chem B 2017;5:2459–67.
[302] Arshad A, Iqbal J, Mansoor Q. Graphene/Fe_3O_4 nanocomposite: solar light driven fenton like reaction for decontamination of water and inhibition of bacterial growth. Appl Surf Sci 2019;474:57–65.
[303] Zhang W, Shi S, Wang Y, Yu S, Zhu W, Zhang X, et al. Versatile molybdenum disulfide based antibacterial composites for *in vitro* enhanced sterilization and *in vivo* focal infection therapy. Nanoscale 2016;8:11642–8.
[304] Wu MC, Deokar AR, Liao JH, Shih PY, Ling YC. Graphene-based photothermal agent for rapid and effective killing of bacteria. ACS Nano 2013;7:1281–90.
[305] Wang N, Hu B, Chen ML, Wang JH. Polyethylenimine mediated silver nanoparticle-decorated magnetic grapheme as a promising photothermal antibacterial agent. Nanotechnol 2015;26:195703.
[306] Yu S, Li G, Liu R, Ma D, Xue W. Dendritic Fe_3O_4@Poly(dopamine)@PAMAM Nanocomposite as Controllable NO-Releasing Material: A Synergistic Photothermal and NO Antibacterial Study. Adv Funct Mater 2018;28:1707440.
[307] Zhao B, Wang H, Dong W, Cheng S, Li H, Tan J, et al. A multifunctional platform with single-NIR-laser-triggered photothermal and NO release for synergistic therapy against multidrug-resistant gram-negative bacteria and their biofilms. J Nanobiotechnol 2020;18:59.
[308] Yu YT, Shi SW, Wang Y, Zhang QL, Gao SH, Yang SP, et al. A ruthenium nitrosyl-functionalized magnetic nanoplatform with near-infrared light-controlled nitric oxide delivery and photothermal effect for enhanced antitumor and antibacterial therapy. ACS Appl Mater Interfaces 2020;12:312–21.
[309] Nablo BJ, Prichard HL, Butler RD, Klitzman B, Schoenfisch MH. Inhibition of implant-associated infections *via* nitric oxide release. Biomaterials 2005;26:6984–90.
[310] Gao Q, Zhang X, Yin W, Ma D, Xie C, Zheng L, et al. Functionalized MoS_2 nanovehicle with near-infrared laser mediated nitric oxide release and photothermal activities for advanced bacteria-infected wound therapy. Small 2018;14:1802290.
[311] Huang S, Liu H, Liao K, Hu Q, Guo R, Deng K. Functionalized GO nanovehicles with nitric oxide release and photothermal activity-based hydrogels for bacteria-infected wound healing. ACS Appl Mater Interfaces 2020;12:28952–64.
[312] Chen W, Ouyang J, Liu H, Chen M, Zeng K, Sheng J, et al. Black phosphorus nanosheet-based drug delivery system for synergistic photodynamic/photothermal/chemotherapy of cancer. Adv Mater 2017;29:1603864.
[313] Mainardes RM, Silva LP. Drug delivery systems: past, present, and future. Curr Drug Targets 2004;5:449–55.
[314] Shim G, Kim MG, Park JY, Oh YK. Graphene-based nanosheets for delivery of chemotherapeutics and biological drugs. Adv Drug Delivery Rev 2016;105:205–27.
[315] Liu J, Cui L, Losic D. Graphene and graphene oxide as new nanocarriers for drug delivery applications. Acta Biomater 2013;9:9243–57.
[316] Sattari S, Dadkhah Tehrani A, Adeli M. pH-responsive hybrid hydrogels as antibacterial and drug delivery systems. Polymers 2018;10:660.
[317] Wells C, Vollin-Bringel O, Fiegel V, Harlepp S, Van Der Schueren B, Bégin-Colin S, et al. Engineering of mesoporous silica coated carbon-based materials optimized for an ultrahigh doxorubicin payload and a drug release activated by pH, T, and NIR-light. Adv Funct Mater 2018;28:1706996.
[318] Liang J, Chen B, Hu J, Huang Q, Zhang D, Wan J, et al. pH and thermal dual-responsive graphene oxide nanocomplexes for targeted drug delivery and photothermal-chemo/photodynamic synergetic therapy. ACS Appl Bio Mater 2019;2:5859–71.
[319] Huang Y, Gao Q, Li X, Gao Y, Han H, Jin Q, et al. Ofloxacin loaded MoS_2 nanoflakes for synergistic mild-temperature photothermal/antibiotic therapy with reduced drug resistance of bacteria. Nano Res 2020;13:2340–50.
[320] Li X, Zhang Z, Fakhri A, Gupta VK, Agarwal S. Adsorption and photocatalysis assisted optimization for drug removal by chitosan-glyoxal/polyvinylpyrrolidone/Mo_S2 nanocomposites. Int J Biol Macromol 2019;136:469–75.
[321] Liang Y, Zhao X, Hu T, Chen B, Yin Z, Ma PX, et al. Adhesive hemostatic conducting injectable composite hydrogels with sustained drug release and photothermal antibacterial activity to promote full-thickness skin regeneration during wound healing. Small 2019;15:1900046.
[322] Ma M, Liu X, Tan L, Cui Z, Yang X, Liang Y, et al. Enhancing the antibacterial efficacy of low-dose gentamicin with 5 minute assistance of photothermy at 50 °C. Biomater Sci 2019;7:1437–47.
[323] Zhang C, Hu DF, Xu JW, Ma MQ, Xing H, Yao K, et al. Polyphenol-assisted exfoliation of transition metal dichalcogenides into nanosheets as photothermal nanocarriers for enhanced antibiofilm activity. ACS Nano 2018;12:12347–56.
[324] Li Y, Liu X, Li B, Zheng Y, Han Y, Chen DF, et al. Near-infrared light triggered phototherapy and immunotherapy for elimination of methicillin-resistant *staphylococcus aureus* biofilm infection on bone implant. ACS Nano 2020;14:8157–70.
[325] Li Y, Xu X, Liu X, Li B, Han Y, Zheng Y, et al. Photoelectrons mediating angiogenesis and immunotherapy through heterojunction film for noninvasive disinfection. Adv Sci 2020;7:2000023.
[326] Sun Y, Chen Z, Gong H, Li X, Gao Z, Xu S, et al. Continuous "snowing" thermotherapeutic graphene. Adv Mater 2020;32:2002024.
[327] Bu Y, Cui B, Chen P, Yang Z. Preparation of a microwave-responsive hollow-mesoporous Fe_3O_4/nGO composite for on-demand controllable drug release. New J Chem 2018;42:13406–13.
[328] Fu C, He F, Tan L, Ren X, Zhang W, Liu T, et al. MoS_2 nanosheets encapsulated in sodium alginate microcapsules as microwave embolization agents for large orthotopic transplantation tumor therapy. Nanoscale 2017;9:14846–53.
[329] Wang S, Tan L, Liang P, Liu T, Wang J, Fu C, et al. Layered MoS_2 nanoflowers for microwave thermal therapy. J Mater Chem B 2016;4:2133–41.
[330] Li S, Zhao Z, Yu D, Zhao JZ, Su Y, Liu Y, et al. Few-layer transition metal dichalcogenides (MoS_2, WS_2, and WSe_2) for water splitting and degradation of organic pollutants: understanding the piezocatalytic effect. Nano Energy 2019;66:104083.
[331] Liu J, Liu F, Bao R, Jiang K, Khan F, Li Z, et al. Scaled-up direct-current generation in MoS_2 multilayer-based moving heterojunctions. ACS Appl Mater Interfaces 2019;11:35404–9.
[332] Zhao X, Lei Y, Fang P, Li H, Han Q, Hu W, et al. Piezotronic effect of single/few-layers MoS_2 nanosheets composite with TiO_2 nanorod heterojunction. Nano Energy 2019;66:104168.
[333] Su K, Tan L, Liu X, Cui Z, Zheng Y, Li B, et al. Rapid photo-sonotherapy for clinical treatment of bacterial infected bone implants by creating oxygen deficiency using sulfur doping. ACS Nano 2020;14:2077–89.
[334] Pan M, Liu S, Chew JW. Unlocking the high redox activity of MoS_2 on dual-doped graphene as a superior piezocatalyst. Nano Energy 2020;68:104366.
[335] Li Z, Zhang T, Fan F, Gao F, Ji H, Yang L. Piezoelectric materials as sonodynamic sensitizers to safely ablate tumors: a case study using black phosphorus. J Phys Chem Lett 2020;11:1228–38.
[336] Chou TM, Chan SW, Lin YJ, Yang PK, Liu CC, Lin YJ, et al. A highly efficient Au-MoS_2 nanocatalyst for tunable piezocatalytic and photocatalytic water disinfection. Nano Energy 2019;54:14–21.

Bo Li received his Bachelor of Engineering in 2018 from Hubei University. He is a PhD candidate in Hubei University, under the co-supervision of Prof. Xiangmei Liu (Hubei University ; Hebei University of Technology) and Prof. Shuilin Wu (Peking University). His current scientific interest focuses on two-dimensional materials-based photo-responsive antibacterial materials.

Yue Luo is a postgraduate of the School of Materials Science and Engineering of Hubei University. She is studying for a Ph.D. under the guidance of Prof. Shui-Lin Wu. Her research interests are mainly in the study of osteogenesis and antibacterial materials. These materials mainly include photocatalytic materials, titanium implants, etc.

Yufeng Zheng received his Ph.D. from Harbin Institute of Technology. He is a professor of the School of Materials Science & Engineering, Peking University. His research interests and directions are mainly to develop new metal biomaterials (biodegradable metals including magnesium alloys, iron alloys and zinc alloys, bulk metallic glasses, bulk nanocrystalline materials, shape memory alloys, titanium alloys, etc.), surface modification of biomaterials and the development of interventional therapy and minimal invasive therapy devices (stent, occlude, etc).

Xiangmei Liu received her Ph.D. from City University Hong Kong. She is a professor of the School of Health Science & Biomedical Engineering, Hebei University of Technology. Her research interests and directions are mainly light response materials, antibacterial biomaterials, wound repair materials, etc.

Lei Tan received his Ph.D. from Wuhan University. He is an associate professor of the School of Materials Science & Engineering, Hubei University. His research interests and directions are mainly light response materials, antibacterial biomaterials, osseointegration materials, etc.

Shuilin Wu Academic qualifications: PhD in Physics & Materials Science (2007) from City University of Hong Kong Current position: Tenured Professor, School of Materials Science & Engineering, Peking University Relevant research area: Biomedical materials; Surface biofunctionalization of biomaterials; Tissue engineering; Photo-Responsive antibacterial materials; MOF-based photo-responsive antibacterial materials.